12-2007

Finite element modeling of soft tissue deformation.

Hongjian Shi
University of Louisville

FINITE ELEMENT MODELING OF SOFT TISSUE DEFORMATION

By

Hongjian Shi
B.Sc. 1984, Math, Henan Normal University, China
M.Sc. 1987, Math, Peking University, China
Ph.D. 1997, Math, Simon Fraser University, Canada
M.A.Sc. 2001, ECE, University of British Columbia, Canada

A Dissertation
Submitted to the Faculty of the
Graduate School of the University of Louisville
in Partial Fulfillment of the Requirements
for the Degree of

Doctor of Philosophy

Department of Electrical and Computer Engineering
University of Louisville
Louisville, Kentucky

December 2007

FINITE ELEMENT MODELING OF SOFT TISSUE DEFORMATION

By

Hongjian Shi
B.Sc. 1984, Math, Henan Normal University, China
M.Sc. 1987, Math, Peking University, China
Ph.D. 1997, Math, Simon Fraser University, Canada
M.A.Sc. 2001, ECE, University of British Columbia, Canada

A Dissertation Approved on

_____

by the Following Reading and Examination Committee:

_____

Aly A. Farag, Ph.D., Dissertation Director

_____

Amir A. Amini, Ph.D.

_____

Xiangqian Liu, Ph.D.

_____

Michael J. Voor, Ph.D.

_____

Roger D. Bradshaw, Ph.D.

DEDICATION

This dissertation is dedicated to

my wife Guixia, son Tianyu, daughters Jeanne and Annie

for their understanding my degree pursuing during family hardship.

ACKNOWLEDGMENT

ABSTRACT

FINITE ELEMENT MODELING OF SOFT TISSUE DEFORMATION

Hongjian Shi

September 11, 2007

Computer-aided minimally invasive surgery (MIS) has progressed significantly in the last decade and it has great potential in surgical planning and operations. To limit the damage to nearby healthy tissue, accurate modeling is required of the mechanical behavior of a target soft tissue subject to surgical manipulations. Therefore, the study of soft tissue deformations is important for computer-aided (MIS) in surgical planning and operation, or in developing surgical simulation tools or systems. The image acquisition facilities are also important for prediction accuracy.

This dissertation addresses partial differential and integral equations (PDIE) based biomechanical modeling of soft tissue deformations incorporating the specific material properties to characterize the soft tissue responses for certain human interface behaviors. To achieve accurate simulation of real tissue deformations, several biomechanical finite element (FE) models are proposed to characterize liver tissue. The contribution of this work is in theoretical and practical aspects of tissue modeling.

High resolution imaging techniques of Micro Computed Tomography (Micro-CT) and Cone Beam Computed Tomography (CBCT) imaging are first proposed to study soft tissue deformation in this dissertation. These high resolution imaging techniques can detect the tissue deformation details in the contact region between the tissue and the probe for small force loads which would be applied to a surgical probe used. Traditional imaging techniques in clinics can only achieve low image resolutions. Very small force loads

seen in these procedures can only yield tissue deformation on the few millimeters to sub-millimeter scale. Small variations are hardly to detect. Furthermore, if a model is validated using high resolution images, it implies that the model is true in using the same model for low resolution imaging facilities. The reverse cannot be true since the small variations at the sub-millimeter level cannot be detected. In this dissertation, liver tissue deformations, surface morphological changes, and volume variations are explored and compared from simulations and experiments. The contributions of the dissertation are as follows.

For liver tissue, for small force loads (5 grams to tens of grams), the linear elastic model and the neo-Hooke's hyperelastic model are applied and shown to yield some discrepancies among them in simulations and discrepancies between simulations and experiments. The proposed finite element models are verified for liver tissue.

A general FE modeling validation system is proposed to verify the applicability of FE models to the soft tissue deformation study. The validation of some FE models is performed visually and quantitatively in several ways in comparison with the actual experimental results. Comparisons among these models are also performed to show their advantages and disadvantages. The method or verification system can be applied for other soft tissues for the finite element analysis of the soft tissue deformation. For brain tissue, an elasticity based model was proposed previously employing local elasticity and Poisson's ratio. It is validated by intraoperative images to show more accurate prediction of brain deformation than the linear elastic model. FE analysis of brain ventricle shape changes was also performed to capture the dynamic variation of the ventricles in author's other works. There, for the safety reasons, the images for brain deformation modeling were from Magnetic Resonance Imaging (MRI) scanning which have been used for brain scanning.

The measurement process of material properties involves the tissue desiccation, machine limits, human operation errors, and time factors. The acquired material parameters from measurement devices may have some difference from the tissue used in real state of experiments. Therefore, an experimental and simulation based method to inversely evaluate the material parameters is proposed and compared with the material parameters measured by devices.

As known, the finite element method (FEM) is a comprehensive and accurate method used to solve the PDIE characterizing the soft tissue deformation in the three dimensional tissue domain, but the computational task is very large in implementation. To achieve near real time simulation and still a close solution of soft tissue deformation, region-of-interest (ROI) based sub-modeling is proposed and the accuracy of the simulated deformations are explored over concentric regions of interest. Such a ROI based FE modeling is compared to the FE modeling over the whole tissue and its efficiency is shown and as well as its influence in practical applications such as endoscopic surgical simulation.

TABLE OF CONTENTS

LIST OF TABLES

LIST OF FIGURES

CHAPTER I
INTRODUCTION

In medical image analysis, mathematical modeling of tissue deformation and visualization of the surface and volume changes are challenging tasks. The modeling may be employed in surgical planning and operations. For example, before one theory or technique is used on real human patients, it is interesting to use alternatives to replace human patients in a virtual environment to simulate real procedures such as a probe indenting the target tissue, or a scalpel cutting the tissue. Currently, many surgical procedures on human patients are not explored or not accurately modeled and simulated using some mathematical theory and numerical techniques. The potential verified techniques are important for minimally invasive surgeries to protect human health and to save human lives, particularly for surgeries with high accuracy requirements such as human brain surgery to ablate tumors with critical structures nearby.

There are good geometrical models and physical models in research but few are employed in real practice due to the complication of the real surgical procedures or the lack of knowledge of tissue material properties. Accurate modeling is essential in characterizing the tissue material responses. It is very important to verify the applicability of a model for the target tissue. Therefore, it is challenging to verify how good a model is in comparison with other models and what values of the tissue material parameters should be used in the modeling. Obtaining the optimal material parameters is also challenging to achieve accurate modeling of the tissue response if the material experiment is not accurate, or the device induces some errors due to human operations, machine limits, timing factor, or the tissue dehydration. Soft tissue modeling using the acquired images as a starting point, provides a safe and noninvasive way to study the tissue behavior and to simulate the procedures before real operations. The image resolution is also important to describe the

behavior or procedure accurately in capturing small details. So, it is proposed to use high resolution imaging facilities for image acquisition for this study.

In the study, some known models or their variants in applications to soils and fluids are employed to verify their applicabilities to the modeling of soft tissues. The behavior of the soft tissues are between those of solids and fluids. High resolution Micro Computed Tomography (Micro-CT) and medium resolution Cone Beam Computed Tomography (CBCT) images are first employed by in the study of liver tissue deformation to validate some known models potentially applied to the liver tissue. The higher resolution CT images provide a competitive benefit to show surface and volume changes. As known, Micro-CT images and CBCT images have been used traditionally for hard tissue imaging such as the bone, joints, or the boundary regions of bones connected to their neighboring soft tissues. The CBCT images are specially used for dental imaging, and are popular in imaging diagnosis for their high resolution and high quality in describing teeth and jaw related diagnosis and surgical treatment. Although the Micro-CT images and CBCT images can not be used to identify intensity changes inside soft tissues, for the liver tissue, the intensity and structure of the liver are quite evenly distributed and so the outer surface shape can be shown by reconstructing the three-dimensional liver volume. In this study, a model validation standard is established to verify the applicability of a model to some target tissue under small force loads. For small force loads, the surface change of the liver may not be detected by traditional CT imaging. The applicability of a model to the liver deformation verified by Micro-CT and CBCT imaging implies its applicability of the model applied to traditional CT images. Further, Micro-CT and CBCT images provide more accurate results. The estimation strategy of optimal values of material parameters and region-of-interest finite element modeling for fast computation for practical applications are also proposed. Although this study focuses on the surface and volume changes, the region of interest based finite element method can also be applied to study the object with different soft materials if the segmentation of the soft materials is successful and their material properties are known. For example, the brain tissue behaves mainly elastic under a very small force load, and the material parameters are known of the brain components

white matter, grey matter, and cerebrospinal fluid ([1]).

A. MODELING OF SOFT TISSUES: AN OVERVIEW

1. Significance of Soft Tissue Modeling

Surgical planning and operations are critical procedures to protect human health and life. The significant progress of computer-aided surgical simulation in the last decade has helped and will be helping surgeons in two main aspects: training of new surgeons, and surgical planning and operations.

The traditional training of a future surgeon is based on an apprenticeship model. The apprentice learns by watching expert surgeons perform surgical operations, and by participating and taking an active role in the operations to gain experience. After sufficient experience, the apprentice may perform operations under the guidance of an expert surgeon and gradually becomes an expert surgeon. Such an education is effective, but it has some disadvantages: The apprentice may need a long time to gain experience which increases the education cost; the apprentice inside an operation room may affect and delay the ongoing surgery due to the space limit; the number of surgical procedures increases for surgeries minimally invasive to neighboring healthy tissues; the accuracy is lower in perception than computer predicts. Computer-assisted training may offer good solutions [2, 3] to complement these disadvantages. If an apprentice is initially trained on computer simulated phantoms, the apprentice may make incorrect procedures without any consequence and learn quickly from them by correcting the errors from repeated practices. Animals and phantoms may provide alternatives to patients in computer simulation. Virtual environments can be made in experiments to gain operation skills of surgical procedures ([4–6]).

Before surgery, the surgeon always explains the operation and its possible complications. As a part of this, the surgeon needs to know the position of the tumor, the possible path for operation, and the possible tissue change in its neighboring region. The imaging scans can always be obtained. Three dimensional object reconstruction from the

scanned images can help the surgeon to know the accurate position of the tumor. The tissue deformation for certain operations due to a surgical tool (probe) can also be predicted before surgery ([7, 8]). This can help the surgical planning be more organized and help the surgery go more smoothly with no or less damage to the neighboring healthy tissue around the probe. One example is the planning of image guided cryosurgical treatment of liver cancer. The cryosurgery (also known as cryotherapy) destroys tumor cells using cold temperatures. This is done by inserting a stainless steel probe (cryoprobe) into contact with the tumor. A cryogenic agent (e.g., argon gas or nitrogen liquid) is circulated through the end of the cryoprobe freezing the nearby cells. The frozen tissue thaws and is either naturally absorbed by the body (internal tumor), or it dissolves and forms a scab (external tumor) ([9]). During a cryosurgery, the doctor uses MR images or ultrasound images to guide the cryoprobe and to monitor the freezing of the cells. Image-guided minimally invasive surgery (MIS) is promising in predicting the tissue changes before and during surgical operations and helps the surgeon to know the tissue changes and deformations due to surgical tools and human factors such as pushing force with different human interfaces. The technology involves both virtual and augmented reality tools to facilitate the surgeon's task in surgical planning and operations.

2.   Mechanics of Soft Tissues

Human tissues are among the most interesting and complex materials that an engineer may study. Though much is not known about the human body and its organs and tissues, some things are known: every component in tissue, every architectural nuance in its geometry, every quirk in its mechanical or electrical behavior, all integrated together to provide a systemic response that is perfectly suited for the development of life. As engineers, it is the treat to examine the body and its constituents, to learn about the system and its parts and why they respond as they do. Using this knowledge, the medical professionals can be assisted in diagnosis and optimization of surgical treatments for pathologies that affect the human body.

To mimic realistic tissue behavior, it is important to obtain mechanical properties of the soft tissue. Soft tissues may be classified into two categories: (1) solid, which includes brain, liver, spleen, and pancreas, and (2) hollow, which includes gall bladder, stomach, and bowel (e.g., [10]). The liver tissue is a soft tissue and its density is approximately even distributed. In these these studies, some of the works were focused on the spleen and liver, because they consist of a dense connective tissue capsule surrounding the parenchyma, and can be treated as approximately isotropic, homogeneous, and incompressible ([10], [11], [12], and [13]). The mechanical properties of a given tissue can be measured either *in vivo* [10, 14, 15] or *ex vivo* [11]. It is more ideal to measure the tissue properties using *in vivo* tests than using *ex vivo* tests. However, it is difficult to do so for several reasons such as uncontrolled boundary conditions, noise, accessibility, and ethics. In literature such as [15], the effects of different testing conditions were studied and an artificial environment was created to mimic the *in vivo* environment.

In reality, soft biological tissues are inhomogeneous, anisotropic and are often subjected to large deformations. One type of mathematical model usually cannot describe the complex mechanical response of a soft tissue even under small force loads. For larger force loads, the soft tissue deforms larger in a more nonlinear manner in geometry and material. So, many attempts have been made to describe the nonlinear behavior ([14–17]). Different biomechanical models have been developed for different types of soft tissues such as liver, brain, muscle, and kidney (e.g., [10, 14]). These attempts recorded the ways to approach the accurate prediction of the mechanical behavior of soft tissues.

3.   Finite Element Methods (FEM)

The FEM originated from the need for a method to solve complex elasticity, and structural analysis problems in both civil engineering and aeronautical engineering. However, it has since been used in many fields. One essential characteristic is the decomposition of a continuous domain into a set of discrete sub-domains. Such a characteristic provides a great advantage to employ local information comprehensively and to describe variation

details, while much computation is needed.

The development of the FEM in continuum mechanics is often based on an energy principle, e.g., the virtual work principle or the minimum total potential energy principle, which provides a general, intuitive and physical basis that has a great appeal to engineers. Mathematically, the finite element method is employed to find approximate solutions of partial differential equations as well as solutions of integral equations or their combinations. The solution approach is usually a numerically based simulation.

In the modeling of the mechanical response of a soft tissue, the finite element method has been employed to solve the established constitutive equation which describes the soft tissue behavior. The comprehensive employment of local information makes the FEM efficient in describing the shape changes of the soft tissue. On the other hand, with the increase of the computation power of computers, the finite element based modeling becomes an efficient and accurate technique in many applications.

4.   Existing Models and Their Applications

The FEM has been widely used in engineering for its discrete approximation to complicated shape continuum solids. The FEM was employed earlier in the analysis of human organ stresses [12, 18]. However, the applications were not image based modeling and they were focused on the study of mechanical properties. Modeling of soft tissue deformations began in the middle of 1990s in order to reduce incident inaccuracy induced by surgical tools during surgical processes [19]. Pure image-based models have been used for the prediction of displacements assuming some image similarity and small displacements between 2D images ([20–22]). However, without correct physical information of the soft tissues, these models usually could not predict the real shape changes since two objects with same shape but with different material characteristics may change their shapes quite differently under an equal force load. To cope with this, some physical deformation models utilizing the tissue characteristics have been proposed ([23–26]). These models used better physical regularization constraints on the image similarity but did not incorporate specific

material properties of the target tissues. The biomechanical models incorporating specific material properties were used early in the modeling of heart tissue motion (e.g., [27]). In that work, the linear elastic model was presented to estimate the force driven left ventricular deformation. Because of its simplicity, the linear elastic model was widely used in early surgical simulation and is still used frequently ([28–30]).

With the increasing speed of computer processing, the prediction accuracy attracts more attention. More complicated biomechanical models have been employed to predict the deformations or registrations of brain, liver, skin and muscle tissues ([13, 30–32]). These models were mainly used to study brain deformation ([33–36]). Some works on the liver tissue modeling using the FEM were reviewed and reported in [37] where the low resolution images were used in prediction. However, the validation of these models, or of newer finite element models for the liver tissue is still challenging. The modeling of tissue deformation and validation of the modeling are necessary steps in building a real surgical simulator for clinical use.

The inaccuracy of brain surgery is mainly due to the brain deformation induced by the surgical tool during surgery. A number of studies on finite element modeling of the brain deformation in minimally invasive surgery appeared in the past five years (e.g., [17, 30, 33, 38]). Edwards et al. ([38]) used the minimum energy method and simple grids in 2D for their modeling of surgical procedures. Škrinjar et al. ([30]) presented a homogeneous linear viscoelastic model. Miller and Chinzei [17] presented a nonlinear viscoelastic model based on the strain energy function. Miga et al. [33] presented a biphasic model composed of an isotropic linear elastic solid and a fluid component which is represented by the interstitial pressure distribution. To improve the accuracy in the prediction of brain deformation, recent studies have used intraoperative imaging to update the prediction during surgical procedures ([31, 32, 35, 36, 39–42]). The finite element models in [31, 32, 35, 39–43] assumed the brain tissue as a single isotropic material. Miller et al. ([17, 34, 44, 45]) presented several finite element models for the brain tissue deformation. Soza [46] and Kemper [47] proposed a method to search for optimal constant parameters for the isotropic and anisotropic linear elastic models. In all these studies (with the exception of Miga [33])

the entire brain was assumed to have the same parameters on elasticity or other properties. Hagemann et al. ([48, 49]) proposed and implemented a 2D finite element model by incorporating a set of landmarks into their model. The model considers the heterogeneity of the bone and the brain. The model uses iterative segmentation to classify material types and the cubic grid meshes for modeling. In the finite element model proposed by Miga [33], the heterogeneity of the brain tissue was dealt with by classifying the brain tissue into white matter and grey matter which were considered having different mechanical properties. Castellano-Smith et al. ([50]) proposed a mesh warping technique to construct patient-specific finite element models. These generated meshes are based on an atlas mesh in which the inside features are preserved within the meshes. Also, the brain was classified into three types of materials: cerebrospinal fluid, white matter, and grey matter. However, details of meshing and modeling were not presented in that paper.

In [51], Hansen presented a region of interest based finite element modeling of brain deformation. They applied a dynamic model in a region requiring high accuracy and a static model elsewhere. The homogeneity is also assumed for the whole brain. In [1], a mixed finite element model of the brain tissue was proposed and tested using the different material properties of the different tissue components.

This finite element modeling of the soft tissues attempted to describe the tissue responses provides attempts using biomechanical models from the simple linear elastic model to complicated models. Validation of these models is still challenging before it can be employed in clinical practice.

B. PROBLEM STATEMENTS

Several aspects of computer-aided simulation of surgical procedures have been interesting in medical image analysis. One of the most important aspects is the study of soft tissue modeling incorporating the mechanical properties of the soft tissue. In this study, the following problems are considered and addressed:

1. Modeling of Soft Tissues

    Consider a 3D soft tissue volume V and a surgical probe which contacts the tissue surface as shown in Fig. 1. If a pushing force is applied through the probe, how is the soft tissue deforming? Further, how is the tissue deformation described for different interfaces such as the different force loads and different size surgical tools?

2. Validation of Soft Tissue Modeling

    There are a number of geometrical models and mechanical models to characterize the soft tissues. However, determining if a model is suitable to the target soft tissue in comparison with other models is a challenging task. Therefore, the validation of the applicability of a model to a target tissue is an important step before the practical use of such a model in modeling the target tissue. Is there any criterion or standard for validation?

3. Determination of Optimal Material Parameters

    As known, different soft tissues deform quite differently since their material properties are different. The material parameters measurement may be limited to the accuracy of the machine, human operation factors, and the status of the tissue such as temperature and tissue dehydration. Therefore, how are the most accurate material parameters to be obtained for clinic simulation?

4. Region of Interest Modeling for Fast Computation

    For the accuracy of deformation prediction, mechanical models are usually employed in consideration of tissue material properties. The computational analysis for a model of soft tissue incorporating its material properties is considerably large if its mesh is dense and has more than 10000 nodes. For endoscopic surgical simulation, the affected area is well specified. The problem is how to reduce the computation time of finite element analysis. In this study, region of interest finite element modeling is investigated for fast
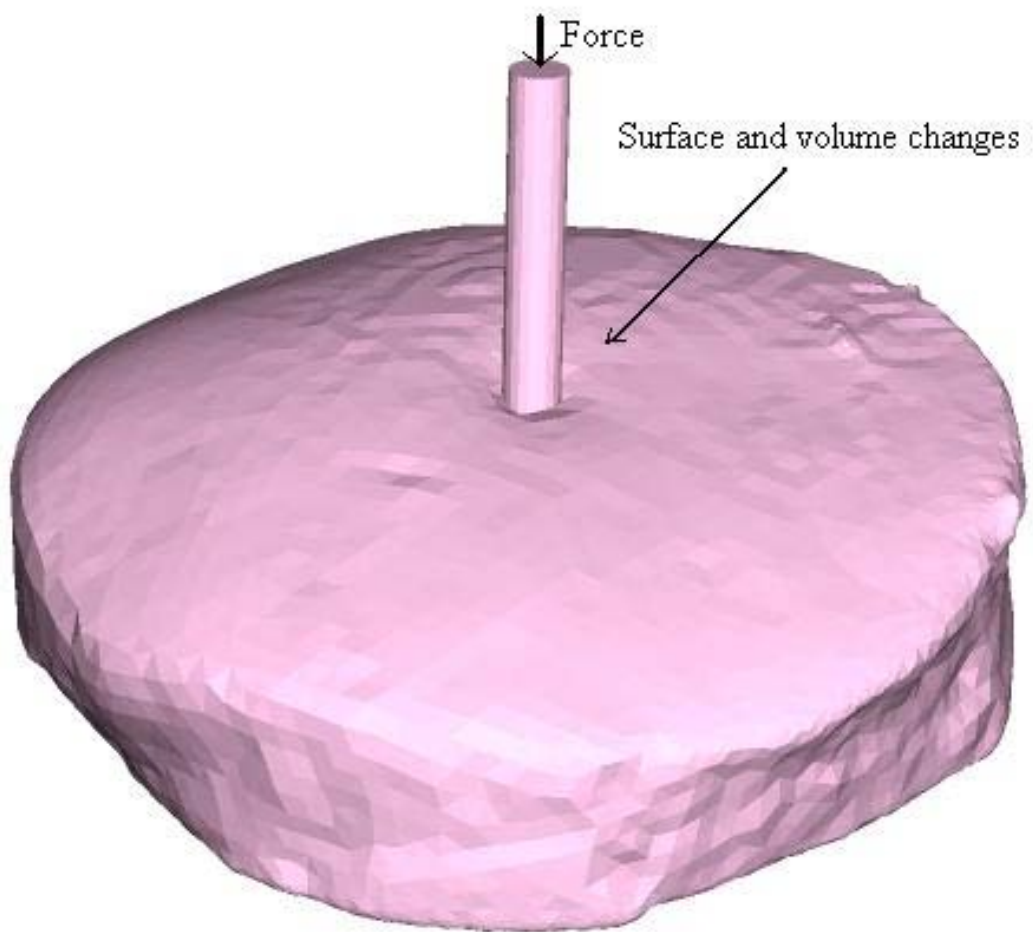
FIGURE 1 – A piece of lamb liver in contact with a probe - this 3D image is reconstructed from 2D Micro-CT slices, and input into the finite element software with the designed probe.

computation and its accuracy is evaluated.

C.   CONTRIBUTION OF THE DISSERTATION

The contribution of this dissertation are in four aspects:

- High resolution imaging facilities are first employed to predict the soft tissue deformation. Such employment has been proved successfully to describe the soft tissue surface and volume shape changes.

- A validation system is proposed to verify the applicability of soft tissue modeling using different types of mathematical models. The linear elastic model and the neo-Hooke's hyperelastic model for the lamb liver was verified in details. The applicability of a model validated using high resolution imaging implies the applicability of the model for the target soft tissue using low images.

- A method to search optimal material parameters in practical environment is proposed and the optimal material parameters for the lamb liver under small force loads are obtained.

- Region of interest based finite element modeling is proposed and its performance is tested over different concentric regions in comparison with the finite element analysis over the entire soft tissue. To speed up the computer simulation, a proper small restricted region can be found. This has potential applications in endoscopic surgical simulation.

D.   DISSERTATION ORGANIZATION

The organization of this dissertation is as follows:

In Chapter II, surgical simulation and the finite element method are introduced and explained for their great benefits in surgical education, planning, and operations. The

prospective and essential component of surgical simulation to describe soft tissue deformation is introduced.

In Chapter III, two basic high resolution imaging techniques are introduced to capture even spaced cross sections for the whole tissue volumes for this study.

In Chapter IV, basic models traditionally employed to described continuum solids are introduced for soft tissue modeling.

In Chapter V, preprocessing procedures including equipment setup, image acquisition, image segmentation are introduced of the soft tissues for finite element analysis.

In Chapter VI, finite element modeling of liver tissue using Micro-CT and CBCT is performed. A validation system is proposed for the prediction accuracy of liver tissue deformation using different models.

In Chapter VII, the volume expression, mesh generation, and the contact of the indentor with volume mesh are introduced in details.

In Chapter VIII, various simulations using different material parameters are performed and compared to those from real experiments to configure the material parameter values.

In Chapter IX, region-of-interest finite element analysis of liver tissue deformation using Neo-Hooke's hyperelastic model is reported over different concentric regions of interest.

In Chapter X, conclusions are made for soft tissue modeling and validation of the modeling and future works are proposed.

E.   SUMMARY

In this chapter, the recent developed geometric and physical models were reviewed in their applications to the prediction of soft tissue deformation. The importance of soft tissue modeling was stressed for the surgical planning and operations to prevent the potential damage to health tissues in surgical procedures. The usage of high resolution imaging facilities was first proposed and the advantages of employing high resolution imaging fa-

cilities were briefly analyzed. Research topics for this dissertation were stated and their challenging aspects were introduced. In the last, the contributions and the organization of the entire dissertation was stated as in the order to appear in content.

CHAPTER II
PROSPECTIVE OF SOFT TISSUE STUDY IN SURGICAL SIMULATION

In the introduction chapter, the recent development of geometric and physical models in research and applications were reported. These models have potential applications in assisting surgical planning and simulations. This chapter will address the prospective of surgical simulations and the surgical simulation project conducted at the Computer Vision and Image Processing (CVIP) Laboratory, University of Louisville.

A.   PROSPECTIVES OF SURGICAL SIMULATION

The advances in medical imaging have been made frequently from the discovery of X-rays for more than 100 years ago. Now the time comes to open new perspectives for the improvement of the computer assisted surgical planning and surgical simulation in operation rooms. Computer tomography and magnetic resonance imaging are widely-used for diagnostic and visualization purposes and the 3D human anatomy provides the information on the geometrical disposition. The main goal of computer surgical simulation is to simulate physical interactions with the virtual body. Currently hundreds of schools in the United States and around the world provide hands-on health care education to medical, nursing, and allied health students. Virtual reality medical simulators used in combination with traditional training methods can provide a comprehensive learning opportunity [52]. Currently, there are more than a dozen companies dedicating to make surgical simulators (Immersion Medical, MD, USA; Verefi Technologies, PA, USA; Simbionix Technologies, OH, USA; Rechin Technologies, Stockholm, Sweden). The main prospectives and benefits of surgical simulation are as follows:

- For educational purposes, medical simulators are changing the practice of medicine. Virtual reality medical simulators used in combination with traditional training meth-

ods can provide a comprehensive learning opportunity. The use of surgical simulators in training programs has been shown to improve performance and lead to shorter response time and less deviation from practice standards than non-simulator training. Using a surgical simulator can increase trainee confidence, competence, and improve patient safety. Medical simulators allow the clinician to safely learn, practice, and repeat the skill or procedure over and over until proficiency is achieved. Simulation training fosters critical thinking, active learning, and confidence building.

- For safety purposes, using virtual reality simulation, medical students, residents, and practicing physicians can learn treatment protocols and master basic and procedural skills before touching a real patient. Physicians can review, repeat, and reassess their performance and find areas for improvement without compromising patient safety.

- Accurate and robust simulations of surgical interventions on virtual patients, including the realistic prediction of their postoperative appearance. The computer assisted surgical planning has many advantages in comparison with conventional planning systems. Once the virtual model of a patient is generated, various case scenarios of the surgical impact and their outcomes can be extensively studied. Better preparation, shorter operation time, lower costs are the immediate benefits.

- Future potential for simulated surgical instruments to operate on real patients to achieve more accurate surgeries to release surgical doctors from possible human vision and physical limitation in performing operation procedures.

B. SURGICAL SIMULATION PROJECT AT CVIP LAB

This section addresses the surgical simulation project at the CVIP lab where this dissertation is written on finite element modeling of tissue deformation.

1.   Introduction

This section addresses the CVIP lab and the initialization of the surgical simulation project. The CVIP lab at the University of Louisville has been pushing research forward in the Biomedical Imaging field for over twelve years: Autonomous Robotics for the past three years, Remote Sensing for the past two years, and has entered the research field of Biometrics the past year and a half. The CVIP Lab is fully staffed, and employees eighteen graduate research students in the fields mentioned above. Virtual Endoscopic applications of hollow organs [53]; Lung Cancer Early Detection [54]; and 3D Modeling the human jaw, teeth, and gums [55].

The CVIP lab is very versatile and has successfully developed technology and new algorithms across disciplines and subject matter. For example, the same vision technology developed in the lab and applied to the virtual endoscope field for vision has been demonstrated as applicable for robotic navigation as well. The same change detection algorithms developed and enhanced at the CVIP lab for the early detection of Lung Cancer has been applied successfully to the Remote Sensing Satellite. It is hoped to study these algorithms' applications to the 3D modeling of the human brain project, as well as to use the finite element method to identify and model the areas of change throughout a brain surgery.

The CVIP Lab has a wide net of multidisciplinary collaborations with over 30 researchers in the mathematical, biomedical and computer sciences areas. The CVIP lab has strong computing equipments to conduct various projects for army or industries related to medical imaging and computer vision.

Researchers at the CVIP lab at the University of Louisville propose to conduct preliminary work in order to develop real-time surgical modeling tools for intra-operative use in delicate organs such as the brain and liver. The CVIP lab works with iMRI Department (Norton Hospital, Louisville, KY) to assist MRI brain data acquisition as required. In the following sections, the surgical simulation project will be introduced in steps.
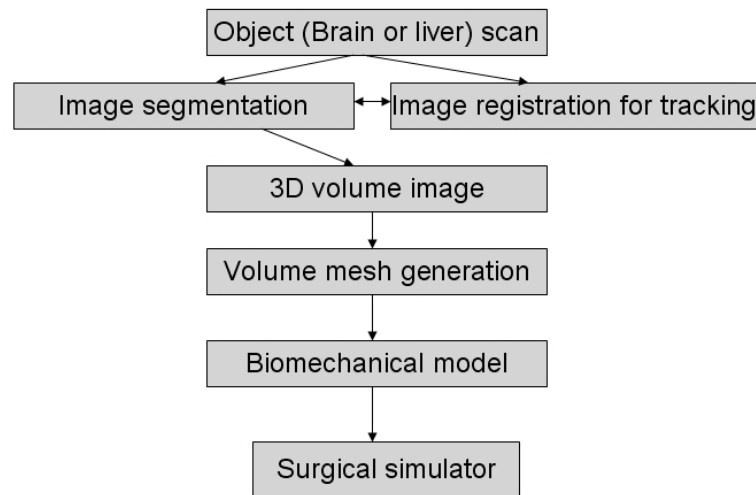
FIGURE 2 – Procedure for the surgical simulation.

2. Segmentation

The first step after image acquisition is the segmentation of the target object such as brain for surgical simulation. It is a very important step to accurately extract the target object from the stack of 2D images. It relates to the accuracy of simulated results, and finite element simulated results in the tissue deposition simulation projects.

a. Introduction The image segmentation is to extract an objects from an image with complicated features except the object inside the image. The process of identifying object boundaries in an image is a crucial step. It has been a persistent challenge from the draw of the digital image processing in the late 1960s. There are a lot of papers on image segmentation in yearly image processing, pattern recognition, and computer vision conferences. Most of these segmentation techniques appearing frequently are application oriented and geometrically based. Therefore, analytic segmentation approach is a desirable goal for surgical simulation. One advantage is that the segmentation is one way straight forwards and fast implementation. Another advantage is the post smoothing procedure is not necessary due to the smoothness of the related solutions. For segmentation, image noise, inhomogeneities, occlusion, lack of strong edges, and sharing image intensities between different objects are the main challenges. For the surgical simulation project, there were

several analytic segmentation algorithms developed at the CVIP lab ([56–58]).

   b. Basic level set method   Osher and Sethian in 1988 introduced the concept of level set representation [59] which provides an analytic approach for surface evolution. Objects in 2D images may be outlined by the intersection of a parametric 3D function and the x-y plane (zero level). Different objects can be identified by controlling the evolution of the 3D function. This level set method is flexible and provides a parametric object description in 2D by energy minimization of curve evolution guided by intrinsic features in an image ([60, 61]).

   The basic level set functions $\Phi_i(x, y, t)$ are represented based on the regions, i.e. it's positive inside the region, negative outside and zero on the interface boundary. The time variable t is used to track the changes of the front evolution curve. Change of the level set function with time results in different curves. The level set function is zero at the front:

$$\Phi(x, y, t) = 0 \tag{1}$$

Full differentiation of both sides of Equation 3 leads to the following equation.

$$\frac{\partial \Phi}{\partial t} dt + \frac{\partial \Phi}{\partial x} dx + \frac{\partial \Phi}{\partial y} dy = 0. \tag{2}$$

Then,

$$\frac{\partial \Phi}{\partial t} + \| \nabla \Phi \| F = 0 \tag{3}$$

where

$$\| \nabla \Phi \| = (\frac{\partial \Phi}{\partial x}, \frac{\partial \Phi}{\partial y}) \tag{4}$$

and $F = \frac{\nabla \Phi}{\|\nabla \Phi\|} \cdot (\frac{dx}{dt}, \frac{dy}{dt})$ is the speed function leading the front propagates.

   Osher and Sethian [59] handled the topology changes by embedding the contour into a higher dimensional function. Evolving contours are represented implicitly by level set functions. An object is outlined through an energy formulation involving the object's boundaries (external energy) and its evolution (internal energy). These energies aim to minimize the arc-length and the area enclosed.

$$E(\phi) = \lambda \int_\Omega g(I)\delta(\phi)\|\nabla \phi\|d\Omega + \nu \int_\Omega g(I)H(\phi)d\Omega \tag{5}$$

where H and δ are the univariate delta dirac function and the heaviside function. The indicator function g depends on the edge of the object as follows:

$$g(I) = \frac{1}{1 + \|\nabla(G_\sigma * I)\|} \tag{6}$$

This function approaches zero approximately at the object edges where the contour evolution stops. The arc-length term is used to smooth the contour with a positive weight λ. The area terms speed up the evolution with a weight ν which can be positive if the object is inside the contour or negative if the object is outside the contour. A contour is represented as the zero level of the function which contains a positive part inside the contour and negative part outside the contour. By the variational calculus [62], the level set function evolves according to the gradient descent optimization. The approach depends largely on the the edge quality.

c. Segmentation using multilevel set functions Surgical planning and navigation benefit from segmentation of anatomical structures from medical images. CT data segmentation can be performed simply using an intensity threshold. However, in general, segmentation requires sophisticated algorithms if the target tissue has complicated structures. The simple intensity based segmentation methods fail to identify the grey matter and white matter components inside brain. The level set segmentation approach provides a better way for accurate segmentation of the brain tissue. It is capable to preserve the topology naturally and recovering the shapes quickly. Level Sets evolution combining global smoothness with the flexibility of topology changes offers significant advantages over traditional statistical classification. As known, the brain tissue consists of grey matter, white matter, and cerebrospinal fluid. So, the number of classes including the background region is four and the class distributions for brain tissue components can be assumed to be Gaussian with known mean and variance. The classes have no common areas and are assumed to be phases separated by interface boundaries where each class has its corresponding level set function. The level set method will be demonstrated from [56], a work developed at the CVIP lab.

The selection of the speed function F in the Equation 3, is very important to keep the change of the front smooth so the format of the speed function is practically selected. The speed function F can be written ([59]): $F = \pm 1 - \epsilon k$. The positive sign means that the front is shrinking and the negative sign means that the front is expanding and ϵ is selected to be a small value for smoothness. κ is the mean curvature of the front computed as follows:

$$\kappa = \frac{\Phi_{xx}\Phi_y^2 - 2\Phi_x\Phi_y\Phi_{xy} + \Phi_{yy}\Phi_x^2}{(\Phi_x^2 + \Phi_y^2)^{3/2}}.$$

The first order and second order partial derivatives are computed same as their definitions in the symmetrical format as follows:

$$
\begin{aligned}
\Phi_x &= \frac{\Phi(x+\Delta x,y,t)-\Phi(x-\Delta x,y,t)}{2\Delta x}, \\
\Phi_y &= \frac{\Phi(x,y+\Delta y,t)-\Phi(x,y-\Delta y,t)}{2\Delta y}, \\
\Phi_{xx} &= \frac{\Phi(x+2\Delta x,y,t)-2\Phi(x,y,t)+\Phi(x-2\Delta x,y,t)}{(2\Delta x)^2}, \\
\Phi_{yy} &= \frac{\Phi(x,y+2\Delta y,t)-2\Phi(x,y,t)+\Phi(x,y-2\Delta y,t)}{(2\Delta y)^2}, \\
\Phi_{xy} &= \frac{\Phi(x+2\Delta x,y+2\Delta y,t)-\Phi(x-2\Delta x,y+2\Delta y,t)-\Phi(x+2\Delta x,y-2\Delta y,t)+\Phi(x-2\Delta x,y-2\Delta y,t)}{4\Delta x\Delta y}.
\end{aligned}
\tag{7}
$$

The solution of the level set function is sensitive to the iterative time step. So, the Courant-Friedrichs-Levy (CFL) restriction [56] is used in selected the time step.

$$\Delta t \leq \frac{\sqrt{\Phi_x^2 + \Phi_y^2}}{(\frac{|\Phi_x|}{\Delta x} + \frac{|\Phi_x|}{\Delta x})F}. \tag{8}$$

The aim is to find the surface iteratively at different time steps. Then at each time step the front is obtained by intersecting the surface with the zero plane. It is needed to track this front by getting the length of the front and its enclosed area. The enclosed area contains all the points where the level set function is greater than zero and the points of the front where the level set function is zero. The positive points are obtained by applying the ideal heaviside step function and the zero points are obtained by applying the delta function. The approximations of the ideal heaviside step and the delta functions are used to deal with the solution smoothness problem as follows:

- The enclosed area:

$$A = \int\int_D H(\Phi)dxdy, \tag{9}$$

- Interface length of the front:

$$L = \int \int_D \delta(\Phi) \| \bigtriangledown \Phi \| dx dy, \tag{10}$$

- Delta Dirac function:

$$\delta_\alpha(\Phi) = \frac{(1 + \cos(\pi\Phi/\alpha))}{2\alpha}, \quad |\Phi| \leq \alpha, \tag{11}$$

- Haviside step function:

$$H_\alpha = 0.5(1 + \Phi/\alpha + \tfrac{1}{\pi}\sin(\pi\Phi/\alpha), \text{ when } |\Phi| \leq \alpha,$$
$$H_\alpha(\Phi) = 1, \text{ when } |\Phi| > \alpha. \tag{12}$$

Figure 3 shows the delta and step function and an example with a level set function. The value of a is always taken $1.5\Delta x$ to make the band equal to $3\Delta x$ where Δx is the grid mesh size which is always 1. Solving the PDE of the level set function requires numerical processing at each point of the image domain, which is a time consuming process. A acceleration process was proposed at the CVIP by only calculating the change of the level set function for a narrow region of points around the front. Large positives or negative values are assigned to the points outside this region. The stability requirement insures valid results with this approach. The existence of the front means that the level set function has positive and negative valued regions, with zero-valued points between them. The level set function with this property is called a signed distance function. This property should be maintained through the iterations to maintain the front.

The proposed algorithm level set method at the CVIP lab achieved successfully. Figure 4 shows the original image (2D), its segmented correspondence, and the 3D image of the segmented white matter inside the brain. This segmentation method is one of the segmentation method developed.

3. Registration

Shape registration is the process of a transformation that maps a given shape to one target according to some similarity measure ([63], [58]). It can also be said a motion
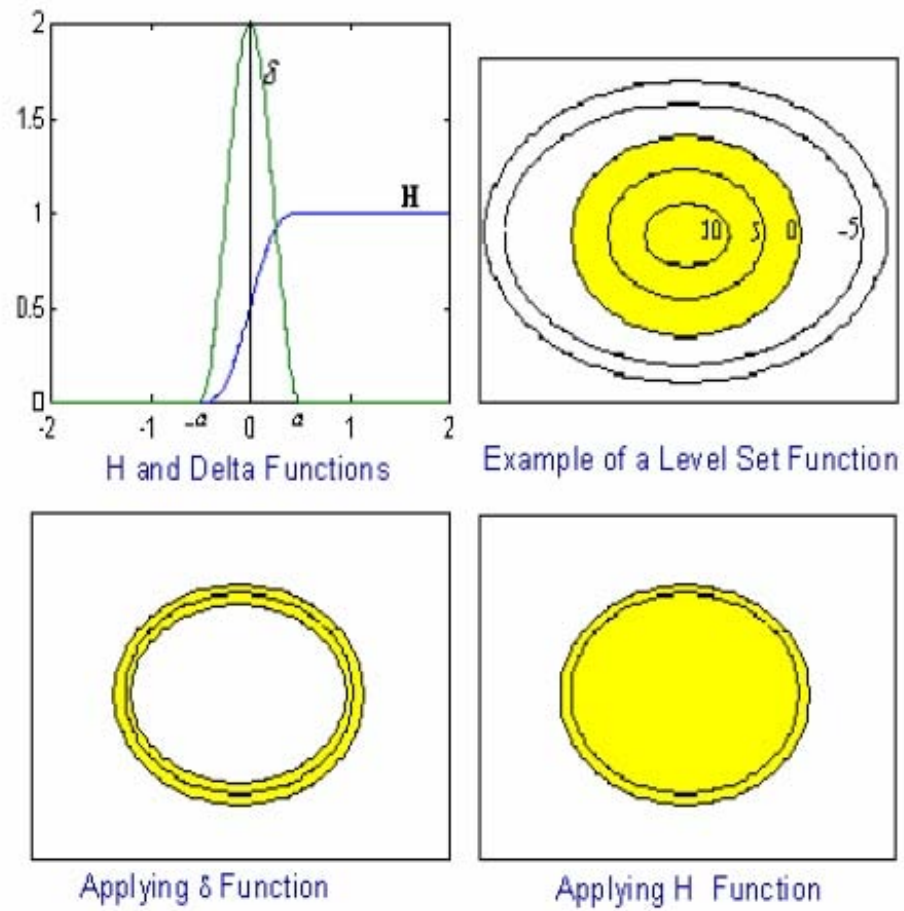
FIGURE 3 – The delta and step function and an example with a level set function.
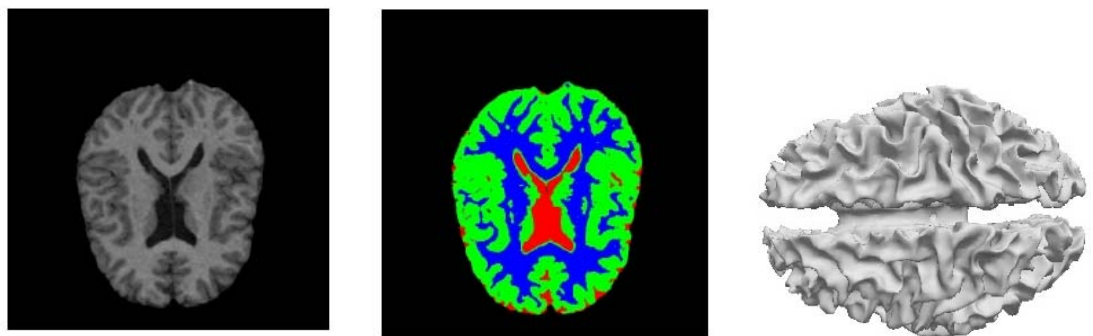
FIGURE 4 – The original image, the segmented image, and the 3D image of the segmented white matter from top to bottom.

Rigid (translation, rotation)

Elastic deformation
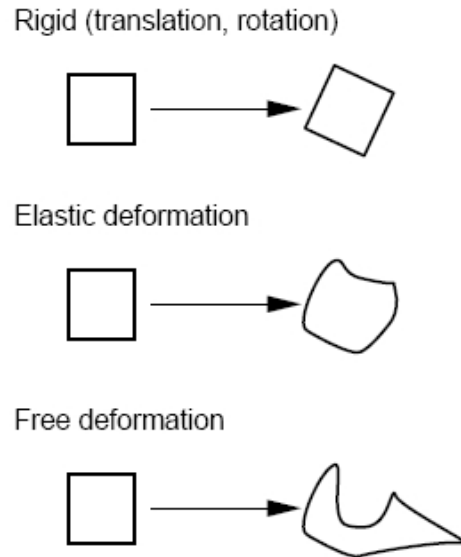
Free deformation

FIGURE 5 – The rigid, elastic, and freeform motion.

process to move the points in one source to another target. The motion can be global or local (also called elastic). Global transformations can rotate, translate, and scale the source instance. Elastic motion means that each point has its own local motion independent of the entire object shape where the point belongs to. The objective of the shape registration is to generate a point correspondences between two given shapes. Figure 5 shows three kinds of motion from one shape to another.

Usually, implicit functions are used as a matching criteria. For example, an energy function may be formulated to be the summation of squared differences between the source and target shapes as one implicit function. The gradient descent is also a commonly used optimization approach to solve the resulting PDEs in order to estimate the optimal transformation that maps the source to its target. At the CVIP lab, several elastic registration algorithm were developed ([58], [64] etc.).

For the surgical simulation project, the iterative closest point (ICP) registration algorithm [65] was employed to register 2D images to the 3D object from segmentation for tracking purpose at the beginning state. The implementation is straightforward ([66]. The iterative closest point (ICP) algorithm is a widely applied method for the registration of two data sets of points. For the ICP algorithm, the source point set is assumed to change or de-

form according to a certain known form of transformation and the target will remain fixed. Transformation parameters represent the way that the source data set moves to the target. The basic steps to implement the ICP algorithm to align two shapes (source P, target X) are as follows:

- Initialize transformation parameters.

- For every point in P, determine its closest point in X.

- Compute the transformation parameters that minimize the sum of square differences between the correspondences.

- Based on the new parameters, update the source points P to the new positions.

- If the change in the source points is less than a certain threshold, terminate, otherwise go to step 2

At the CVIP lab, object motion tracking can be performed accurately and the object is rendered on the computer screen to show the tracking process. The rigid registration was used in 3D position tracking. For the elastic registration and position tracking, the finite element modeling of the brain tissue made elastic registration and tracking possible at the CVIP lab. In the following subsection will address the software interface of the surgical simulation project.

4. Surgical simulator

The application of the FE method to predict brain deformation was performed according to the following main steps. The brain is segmented from from the MRI images to reconstruct an brain object. Then the brain object is meshed into finite elements (tetrahedral or cubes). For the three components of the brain, their Young's moduli are known. A linear weighted Young modulus can be determined for each element based on the number of voxels inside the element. This procedure appears to be a good approximation to the traditional finite element linear elastic model assuming the Young's modulus is constant

throughout the whole volume domain. The details of this finite element modeling of the brain tissue was expounded in the work [1] at the CVIP lab.

The CVIP lab has been developing medical project software after the research on the projects is completed. The following is the software developed for motion tracking and surgical simulation. Figure 6 is the main interface panel for several medical projects performed at the CVIP lab including surgical simulation, lung, virtual endoscopy, and others.

Figure 7 is the interface panel for motion tracking and surgical simulation with no existence of a probe inside the view. On the left of the panel, there are two columns, one for the tracking pipeline and the other for finite element analysis. The procedures are performed one after another from the top to the bottom by pressing the buttons. Computation is performed in background and the result is shown on the screen. The first step is the segmentation. There is the Segmentation button for several choices of segmentation algorithms from the simple intensity thresholding, statistical modeling, to the level set method as discussed in previous segmentation subsection. After segmentation, to save memory the segmented data are saved to computer hard drive for use. Then, the data can be loaded by pressing the Load button. The segmented 2D slices can be seen in the middle of the screen as shown in Figure 7. After this step, by pressing Rendering button, the 3D object will be displayed at the top left frame window in the middle region. The following two buttons are for registration and tracking processes. Figure 8 shows the interface panel with a probe away from the object in view. Figure 9 shows the instance of the probe on the brain.

The adjacent column is for finite element analysis commands from smoothing, stereolithographical (STL) file generation, mesh generation, and finite element analysis. When the Generate STL button is pressed, another single window will appear as in Figure 10. The lower portion is the place to show the volume, generated mesh, and the deformed volume. Here, the ABAQUS [67] is automatically called when the finite element analysis button is pressed and the deformed volume is rendered when the analysis is finished. There are other buttons for coloring, smoothing, spacing, and others which can be seen on the interface panel.
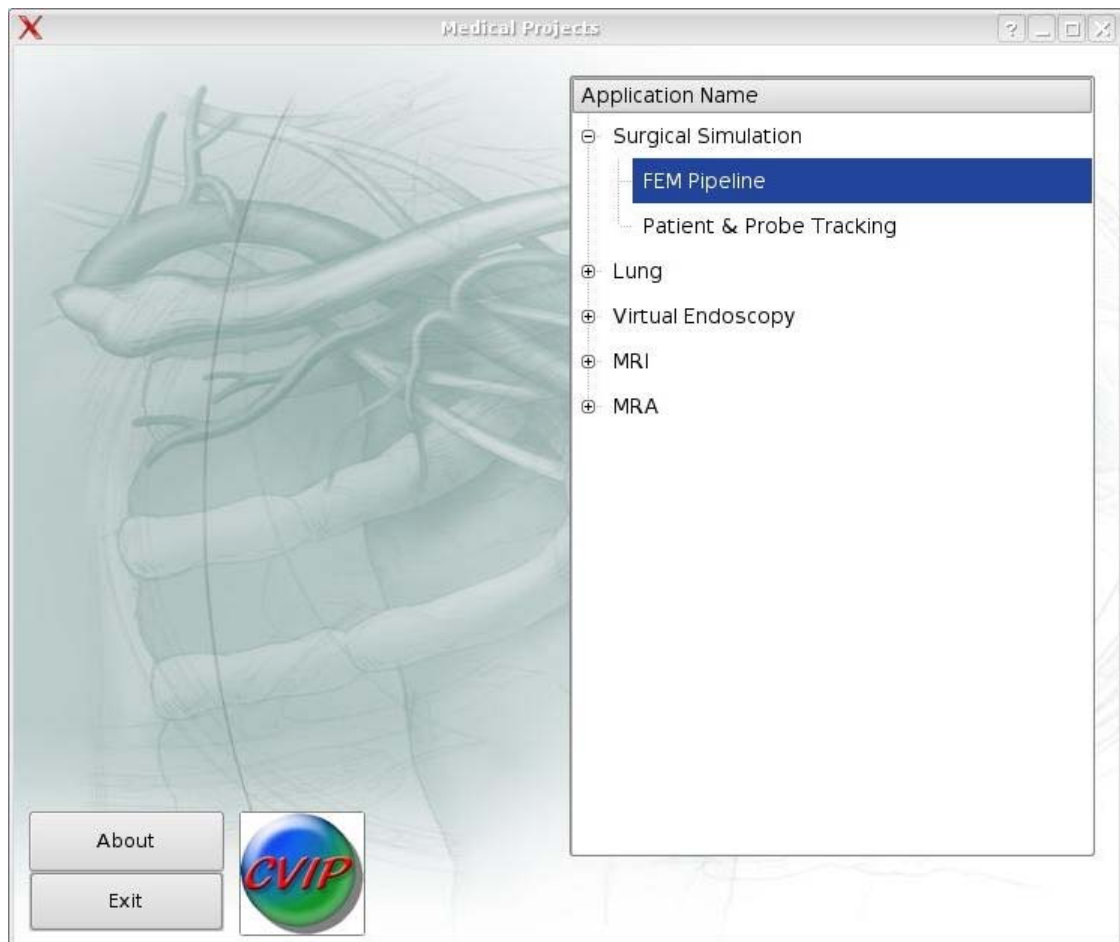
FIGURE 6 – The main menus of the software interface of medical projects at the CVIP.
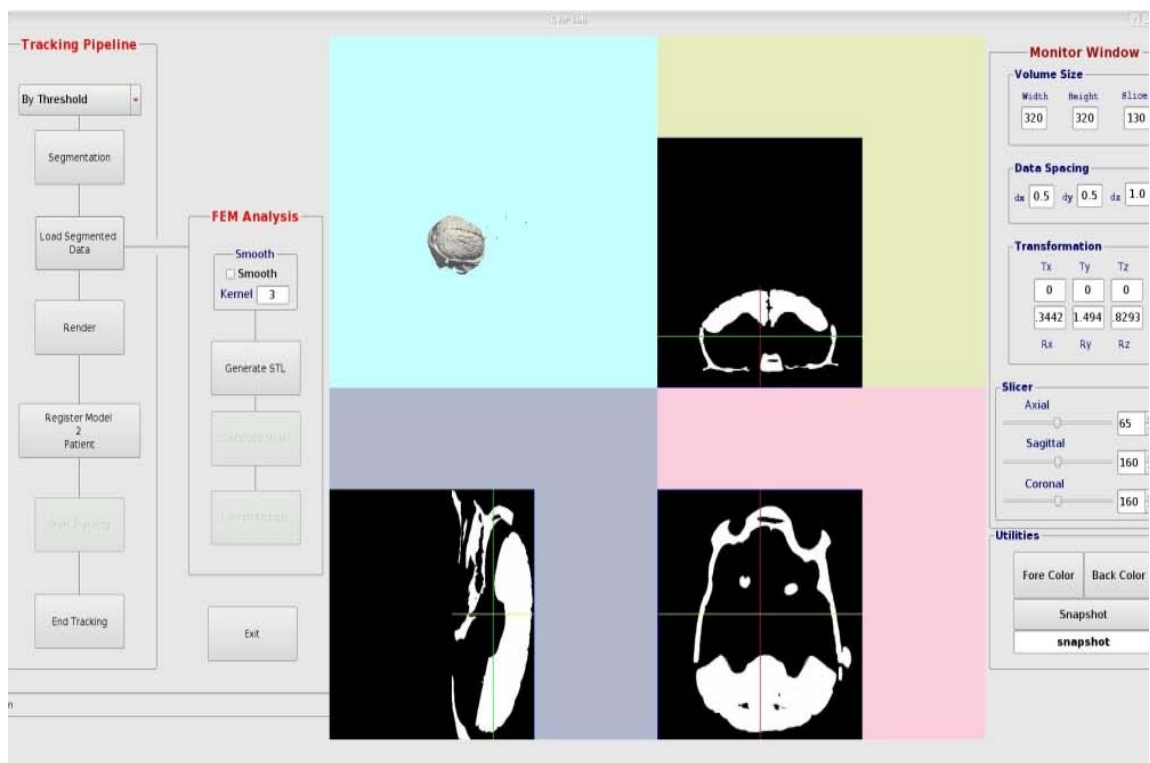
FIGURE 7 – The interface for motion tracking and surgical simulation with no probe existence.
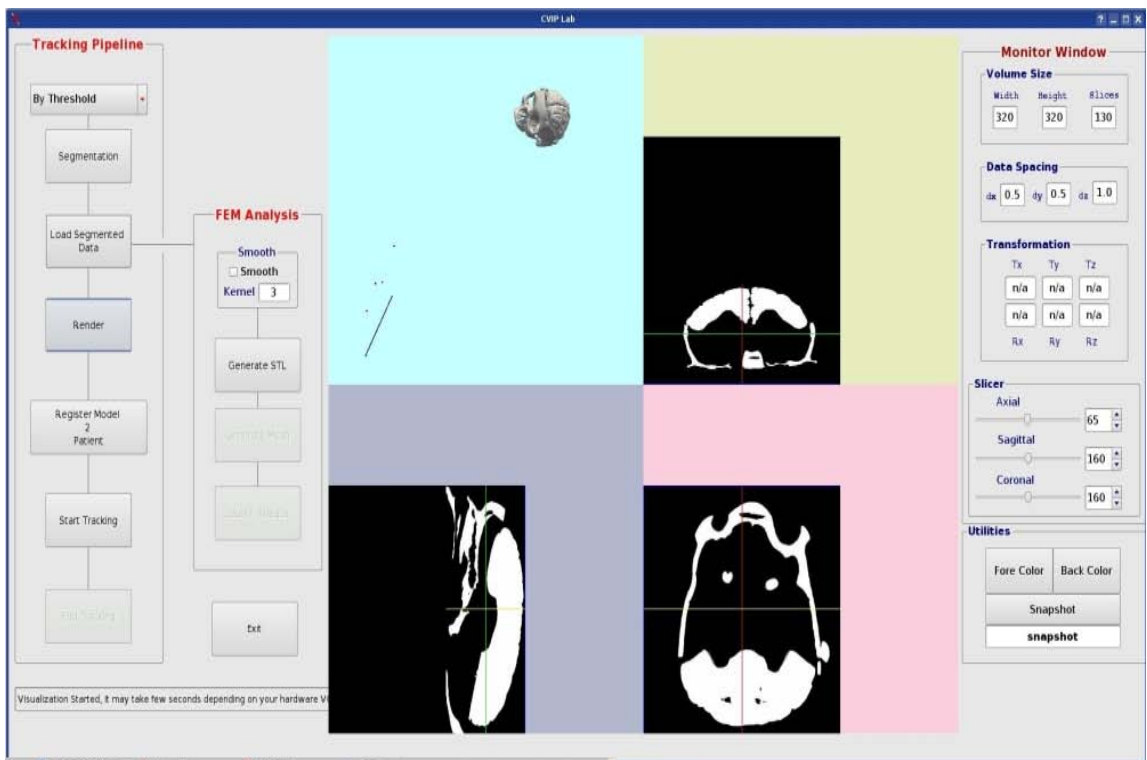
FIGURE 8 – The interface for motion tracking and surgical simulation with a probe away from the object.
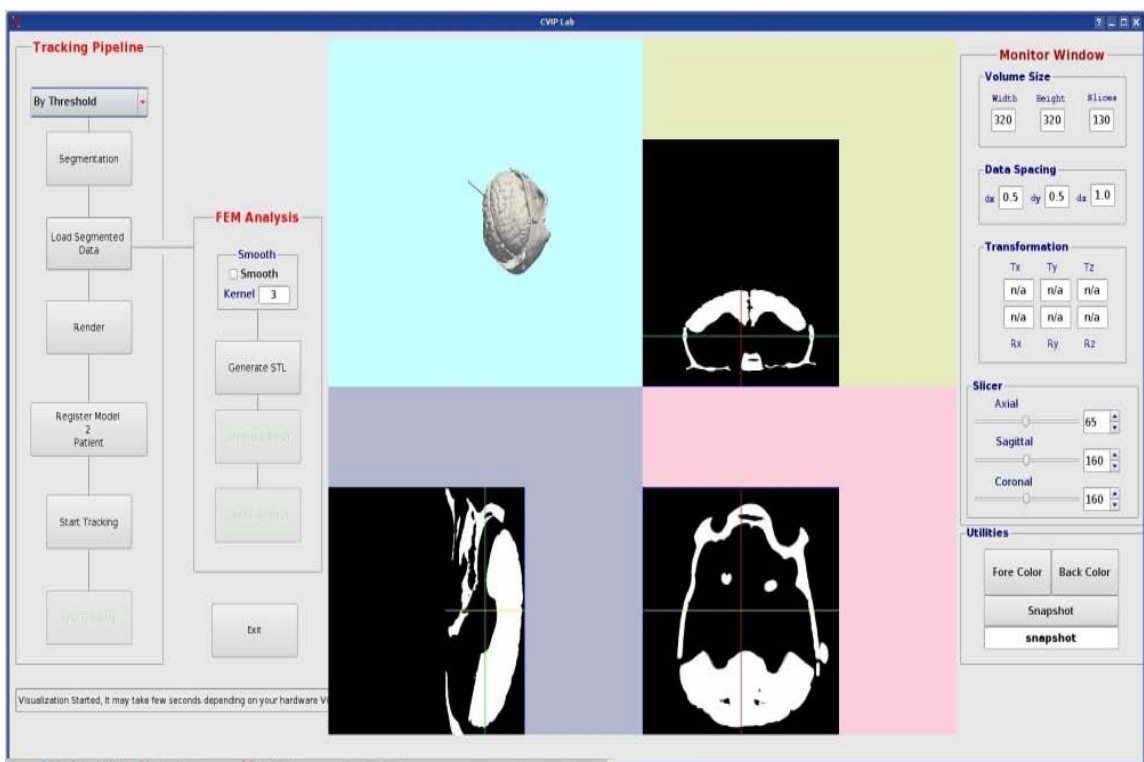
FIGURE 9 – The interface for motion tracking and surgical simulation on or in the object.

FIGURE 10 – The interface for the surgical simulation process.

5. Finite element modeling: the dissertation topic

It is crucial important of the realistic surgical simulation of soft tissue deformations under the impact of an external force. It is the task of the biomechanical modeling to assign reliable physical properties to the target object in order to make it interact according to the underlying physical laws. The nearer a physical model approaches the properties of the tissue the more realistic the simulation results can be obtained. This predication is the central paradigm of the physically based soft tissue modeling. As a start point, the liver with the relatively simple structure is employed for the target tissue for this study. The finite element biomechanical modeling of the liver tissue will be the main topic for the following chapters. Such a study of the finite element biomechanical models is the key part for the accurate surgical simulation on the soft tissues.

C. SUMMARY

This chapter addressed the surgical simulation project and its status. The whole procedure to build a surgical simulation tool was expounded in steps. The simulation tool were used to illustrate to some results for tracking path and surgical simulation. The physical model in surgical simulation is crucial for accurate tissue deformation prediction and position monitoring for surgical planning and real operations. The liver tissue was first considered to search a suitable biomechanical model.

CHAPTER III
HIGH RESOLUTION IMAGING TECHNIQUES

In the past decade, Magnetic Resonance Imaging (MRI) has evolved into one of the most powerful non-invasive techniques in diagnostic clinical medicine and biomedical research. The technique is an application of nuclear magnetic resonance (NMR), a well known analytical method of chemistry, physics and molecular structural biology. The MRI imaging scanner is very expensive and is hard to access. It occupies a very large space in clinical use. The Micro-CT scanners and CBCT scanners are relatively cheaper and easy to access. The imaging technologies Micro Computed Tomography (Micro-CT) and Cone Beam Computed Tomography (CBCT) are new imaging modalities used to complement MRI to provide high resolution images of the imaging targets. Such high resolution computed tomographies are also noninvasive imaging modalities that have been used for various purposes where high resolution images are needed, such as to quantify disease progression in a rabbit model of experimentally induced osteoarthritis [68], and to diagnose the temporomandibular joint syndrome which requires sub-millimeter accuracy [69]. These imaging techniques are relatively cheaper with only 20% to 10% cost compared to MRI imaging technology. The shorter X-ray exposure time and low radiation dose to patients are better features compared to conventional medical CT.

The Micro-CT scanner or CBCT can obtain correct sectional images of the interior of the study objects that are of high precision and density, without destroying or contacting inspection objects. Such state-of-the-art imaging technology allows high-precision and high-speed scanning, serving new applications in various fields. The principle is that the image data sets of the study object in a glass or on a support can be obtained using an X-ray image intensifier or a amorphous flat panel detector by gantry rotating around the study object while irradiating object with X-rays. Some CBCT scanners such as NewTom

32

3G (Quantitative Radiology, Verona, Italy), CB MercuRay (Hitachi Medical Corporation, Tokyo, Japan) use image intensifiers [70]. Micro-CT and CBCT technologies are ideally suited for bony structures and the transition regions from the bony structures to their neighboring soft tissues. This study is focused on the surface and volume changes of the liver tissue. Micro-CT and CBCT are suitable to capture these changes in high precision level. This is because the density of the liver tissue is still quite different from the background air in this experiment. The boundary of the soft tissue can be easily distinguished. In vivo, CT is better at detecting bone against a soft tissue background than distinguishing between different types of soft tissues of similar density.

Micro-CT has been widely used for anatomical structure analysis and Micro-CT machines are made in different types for different purposes. CBCT imaging has been proved successfully of its diagnosis functionalities in dentistry. There are a dozen CBCT scanner manufactures worldwide that make high resolution scanning possible. Strong research facilities at the University of Louisville provide these two imaging facilities for this study. Here, the purpose to use these high resolution techniques is to capture the surface and volume changes of liver tissue deformation under very small force loads to validate some mechanical models for their potential applications in surgery planing or robust surgery. The following section will briefly introduce basic specifications of these two imaging modalities.

A. MICRO COMPUTED TOMOGRAPHY

High resolution Micro-CT imaging technology provides great benefits to clinical engineering and practices since Micro-CT can provide much more detailed resolution than the traditional CT scan. Figure 12 shows the inside of the Micro-CT machine, the target liver, and the test chamber made for this imaging purpose. The outside of the Micro-CT machine is closed for safety purpose of X-ray source exposure. The scanning time is 40 seconds. The reconstruction of 2D images took one to four minutes depending the setting of resolution requirements. More information on Micro-CT technology can be found in

[71]. The basic specifications of the Micro-CT machine used are listed as follows.

- Image resolution - 100 millimeters for image matrix 1024x 1024 pixels

- Calibration - calibration is automatically decided/calibrated by CT system and scanning magnification is centered automatically during magnification change.

- Scan mode - Multiple continuous scanning of specified slices at specified pitch and scanning for full scan or half scan.

- Inspection object - it can be large or small but should be with proper support or container to hold the inspection object.

- Scanning method - rotation.

- Reconstruction time - 2 to 4 minutes depending the image resolution requirement.

- X-ray - Fan beam (see Figure 11) and Micro focusing with 50-70 KeV and 160 μA.

- Imaging system - X-ray image intensifier.

- Image storage - hard disk.

- Software - standard region-of-interest (ROI) setting, statistical calculations, zooming, multi-frame, profile, histogram etc.

B.   CONE BEAM COMPUTED TOMOGRAPHY

Cone beam computed tomography (CBCT) scanners use a cone shaped x-ray beam rather than a conventional linear fan beam to provide images of the bony structures of the skull as shown in Figure 11 and Figure 13. Such scanners are used for a number of applications such as Dental Radiology ([69, 72, 73]), Computed Tomography Angiography [74–76], Interventional Radiology and Mammography [77–79]. However it is mostly used in dental radiology. When compared with other methods of tomographic imaging, CBCT is characterized by rapid volumetric image acquisition from a single low radiation dose
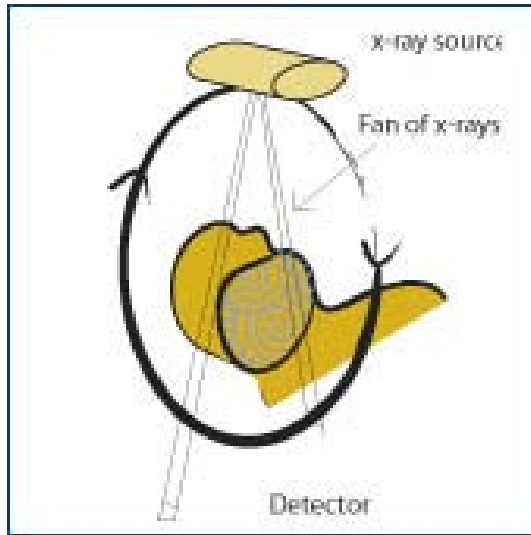
FIGURE 11 – Fan beam CT scanning.
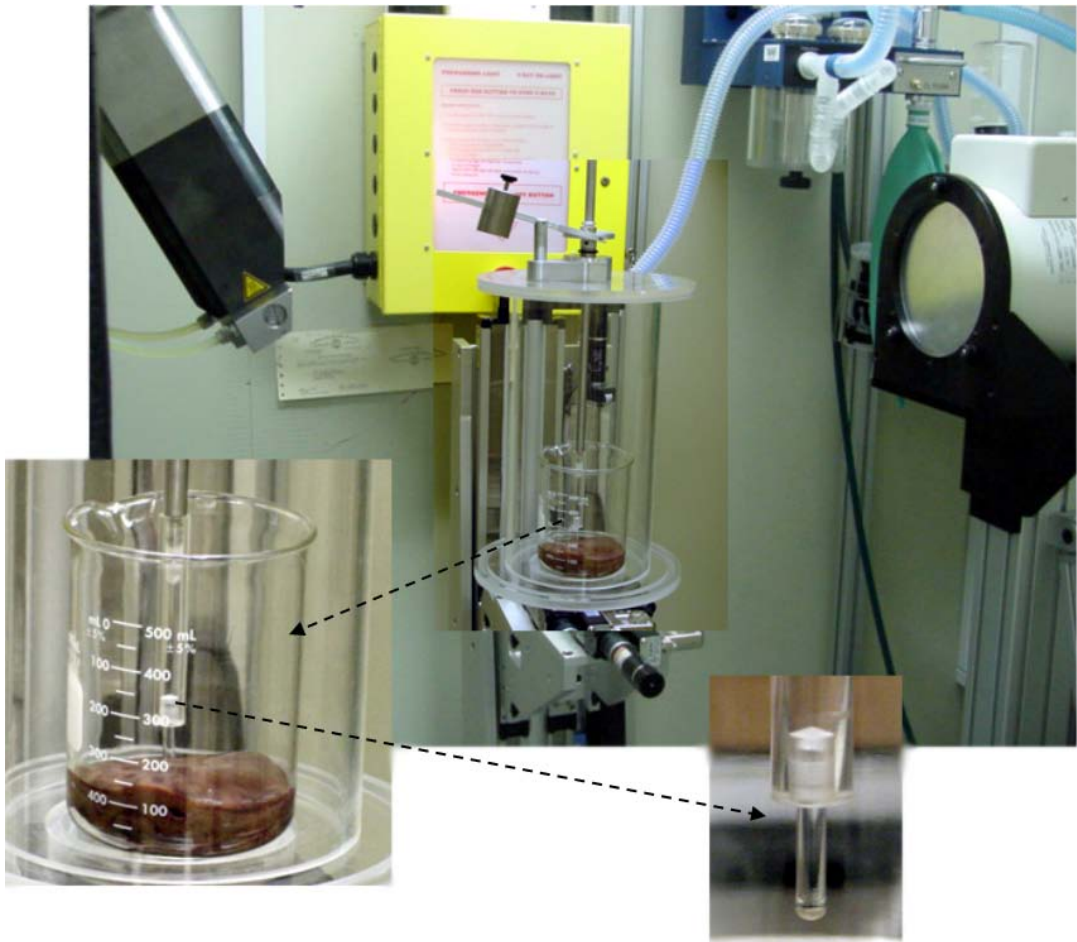
FIGURE 12 – Micro-CT machine and test chamber for liver imaging.
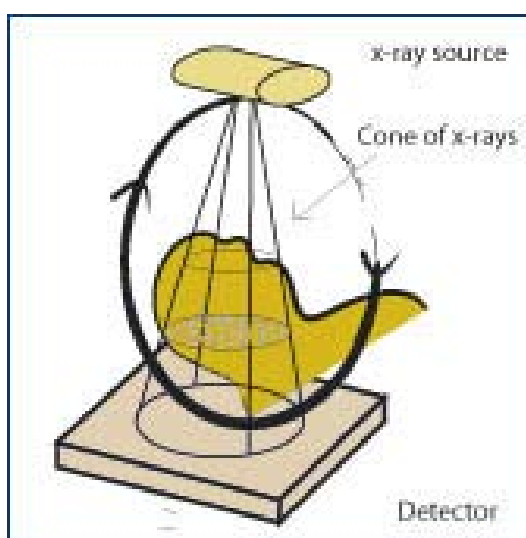
FIGURE 13 – Cone beam CT Scanning.

scan of the patient. Such a CBCT machine dedicated to dental and maxillofacial imaging, particularly for surgical and/or prosthetics implant planning in the field of dentistry. The compact size and relatively low radiation dosage of the CBCT scanner make it ideally suited for imaging the craniofacial region, including dental structures. With the increasing accessibility of CBCT imaging, this modality is emerging as the imaging "standard of care" for the number of diagnostic assessments of the bony components of the face.

Most CBCT scanners use flat panel image sensors instead of the image intensifiers as Micro-CT scanners used. The scanning time CBCT is similar to that of Micro-CT. The scanner is quite smaller than the Micro-CT scanner. Such scanner gives quite accurate images in that the bony information estimation from the image matches well with the real structures in human skull. CBCT scanners can also used to scan the liver tissue to show the volume and surface changes. Figure 14 shows the CBCT scanner from Dental School, University of Louisville. This scanner was used for liver scanning and good quality 2D images were obtained with high contrast to show the inside structure of the liver tissue.

C.   SUMMARY

Micro-CT and CBCT imaging techniques have been used for the bony structures

FIGURE 14 – CBCT scanner.

and the transition regions from the bone structures to their neighboring soft tissues. However, they can be used to study the surface and volume shapes of soft tissues and they can give more accurate results. In this chapter, the two imaging techniques were introduced for the study of soft tissue deformation. The specifications and functionalities of the Micro-CT and CBCT scanners were introduced respectively. The common advantages of these scanners are high resolution image acquisition, short time scanning and reconstruction, low dose X-ray, cheaper price, and small size.

CHAPTER IV
FINITE ELEMENT METHOD AND BASIC BIOMECHANICAL MODELS

As stated in the introduction chapter, the purpose of this study is to find proper mechanical models to describe the mechanical responses of the soft tissues. This chapter will simply introduce the general framework of the linear elastic model (LEM) and the neo-Hooke's hyperelastic model (NHM). These two models are representative basic models to describe the linear elastic and viscous properties.

A.   BASIC CONCEPTS

Continuum mechanics is the study of the response of continuous media to applied force or loading. It deals with continuous matter, including both solids and fluids. Since the matter is made of atoms and commonly has some sort of heterogeneous microstructure, to simplify the approximation to physical quantities, the microstructure is usually ignored and then differential equations can be employed to solve problems in continuum mechanics. Some differential equations are specific to the study material such as constitutive equations, while some capture fundamental physical laws such as conservation of mass. Continuum mechanics may be classified to solid mechanics and fluid mechanics.

Soft biological tissue is in the state between solid and fluid, and so it has a combinational behavior of solid and fluid in response to an applied force load. The liver tissue in this study mainly behaves elastically. However, there is great diversity of mechanical properties in soft biological tissue and it is characterized by very complex mechanical behavior. Soft tissues often have layered fibrous or an even more complicated structure. A most important component of soft tissues is elastin which provides elasticity to arteries, veins and lung parenchyma and keeps skin smooth. Elastin is the component with the most linear elastic properties of soft tissue. This study will test and use the elasticity to predict

tissue surface and volumetric changes under certain amounts of force loads.

Stress is the internal traction vector where force acting on a defined internal datum plane: $\sigma = F/A_o$ where A_o is undeformed cross sectional area.

Strain is the ratio of change in length to the original length.

The **Young's modulus** or **modulus of elasticity** is used to express the ratio of stress to strain. It is then a general property of the material, and is independent of the size or shape of the specimen, and independent of time. The greater the modulus, the stiffer the material.

Hooke's law states the linear relation between stress and strain for linear elastic objects.

Hyperelasticity refers to materials which can experience large elastic strain that is recoverable. Hyperelastic materials have very small compressibility.

Usually a biological soft tissue such as liver tissue is expected to behave as a linear elastic solid when the strain is very small. When the strain is larger, the liver may behave nonlinearly viscoelastic, or hyperelastic. It is the desire of this research to verify different biomedical models for liver tissue.

B.   FINITE ELEMENT METHOD

The theory of the finite element method is rich in textbook and literature such as [80] and [81], Mathematically, the FEM is used to find approximate solutions of partial differential equations (PDE) as well as approximate solutions of integral equations. The solution approach is based either on eliminating the differential equation completely (steady state problems), or rendering the PDE into an equivalent ordinary differential equation, which is then solved using standard techniques such as finite differences, etc. In solving partial differential equations, the primary challenge is to create an equation which approximates the equation to be studied, but which is numerically stable, meaning that errors in the input data and intermediate calculations do not accumulate and cause the resulting output to be meaningless. The FEM is a good choice for solving partial differential equations

over complex domains or when the desired precision varies over the entire domain. This section introduces the basic procedure using FEM to solve Dirichlet boundary value problem (PDEs) [81] in two-dimensional space. However, the procedure and principle are the same for higher dimensional spaces and different boundary value problems with different equations.

Example

$$u_{xx} + u_{yy} = f \quad \text{in} \quad \Omega$$
$$u = 0 \qquad \text{on} \quad \partial\Omega$$

where Ω is a connected open region in the (x, y) plane whose boundary $\partial\Omega$ is smooth, and u_{xx} and u_{yy} denote the second derivatives with respect to x and y, respectively. This is the steady state heat transfer equation. The following steps are used to solve the boundary value problem: formulating the problem as in variational form, discretization of the continuous domain, choosing a basis (shape functions), deriving the numerical matrix expression of the equilibrium equations for all elements and assembling them into a global matrix equation, and solving the derived matrix equation.

1. Variational formulation

Let a function v be a function in the space $H_0^1(\Omega)$ consisting of functions which are differentiable and have zero values on the boundary $\partial\Omega$ as a subset of the domain Ω. Such function space is called Soblev space and can be shown a Hilbert space. Multiplying the function v to both sides of the Direct equation and integrating by parts using Green's theorem, results in:.

$$\int_\Omega fv\,dxdy = -\int_\Omega \nabla u \cdot \nabla v\,dxdy = -\Phi(u, v) \tag{13}$$

The left side is a linear functional of functions v in the space $H_0^1(\Omega)$. Based on the famous Riesz representation theorem in functional analysis, a unique solution (in weak form) u exists for Dirichlet boundary value problem [80].
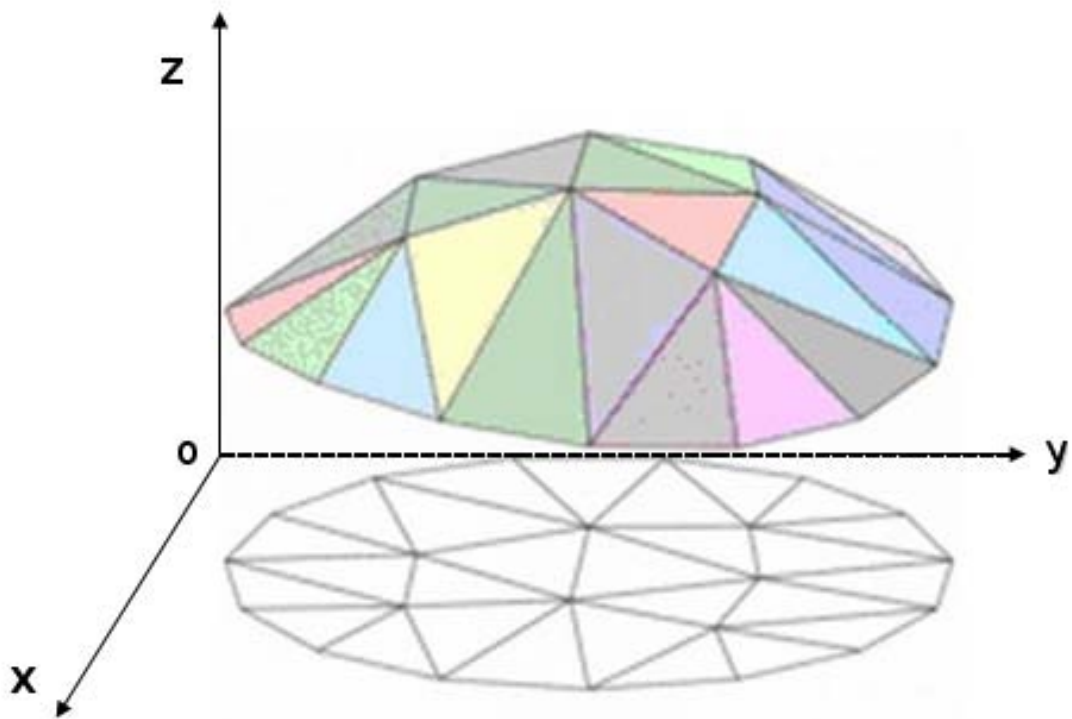
FIGURE 15 – Piecewise linear solution function u on subdivisions of a discretized domain.

2. Domain discretization

The basic idea is to replace the continuous form of Direct boundary value problem with a discretized form to find the solution u in a space V of functions which are linear on each subdivision as shown in Figure 15. The space consists of functions which are linear on each triangle. The triangular grid can be finer and finer so that the solution of the discrete problem can be more approximate to the real solution. However, for larger 3D solids, computational demand being quite large so the triangle size must remain above a minimum level.

Although different types of elements are allowed for one volume, normally one single type of elements is used for all elements. However, the mesh generation will be much complicated.

3. Choice of basis

For two-dimensional domain, one basis function per vertex of the triangulation of the planar region Ω is chosen. The basis function is a unique function of V with value 1 at one vertex and zero at other vertices of a triangular element. The basis function is zero on any other triangular regions. The inner product of any two different basis functions is zero. So, these basis functions are linear independent in the function space $H_0^1(\Omega)$. Let $\{u_k\}_{1 \le k \le n}$ be the basis functions. The solution u and the function f can be expressed as follows:

$$u = \sum_{k=1}^{n} u_k v_k$$

and

$$f = \sum_{k=1}^{n} f_k v_k.$$

Therefore, the Direct boundary value problem can be written as:

$$-\sum_{k=1}^{n} u_k \Phi(v_k, v_j) = \sum_{k=1}^{n} f_k \int_{\Omega} v_k v_j \quad \texttt{for} \quad j = 1, \cdots, n. \tag{14}$$

Once the basis functions have been determined, all values within an element can be interpolated.

4. Assembling the element equations

To find the responses of the overall system modeled by the network of elements, all the element equations must be assembled. The matrix equations expressing the behavior of the elements are combined to form the global system matrix equation expressing the behavior of the entire system. The basis for the assembly procedure stems from the fact that at a node, where elements are interconnected, the value of the field variable is the same for each element sharing that node. A unique feature of the finite element method is that the system equations are generated by assembly of the individual element equations.

From the derived expression using the basis functions, the column vectors u^t and $(f_1, \cdots, f_n)^t$ are denoted by $\mathbf{u}$ and $\mathbf{f}$. Then the global stiffness matrix equation yields:

$$-\mathbf{Lu} = \mathbf{Mf} \tag{15}$$

where $\mathbf{L} = (L_{ij}) = (\Phi(v_i, v_j))$, and $M = (M_{ij})$.

5. Imposing the boundary conditions

Before solving the global system equation, it is needed to impose the known boundary conditions including imposing known nodal values or force loads on known nodes. These conditions can be changed based on the real physical environment and the prior known information.

6. Solving the global system equation

The matrices L and M in Equation 15 are called sparse matrices ([80] and [82]). Most entries in these two matrices are zero. If these matrices are not large, it is easy to invert the matrix $\mathbf{L}$. If the number of elements is large and so the number of vertices (nodes) and the number of basis functions are large. In three-dimensional space, a fine mesh of a solid may have millions of vertices. So, efficient computing techniques are needed to find the solution instead of inverting the matrix L. The conjugate gradient method as an iterative technique is currently used in most FEM softwares. Such method solves large systems faster compared to the direct method. Such method was also called conjugate condensation technique in medical computing community.

7. FEM vs. finite difference method

Unlike the finite difference method which is easy to implement ([82]), the FEM can handle complex geometries but is not easy to implement and is influenced by computation largely. Also, the FEM provides more accurate solutions than the finite difference method. The finite difference method envisions the solution region as an array of grid points, while the FEM envisions the solution region as built up of many small, interconnected subregions or elements. A finite element model of a problem gives a piecewise approximation to the governing equations. The basic premise of the finite element method is that a solution

region can be analytically modeled or approximated by replacing it with an assemblage of discrete elements. Since these elements can be put together in a variety of ways, they can be used to represent exceedingly complex shapes.

C.   LINEAR ELASTIC MODEL

In this section, the linear elastic model is used as formulation to describe the linear elastic responses of an object using the minimum total potential principle and the FEM. An elastic solid is a volume consisting of all $\mathbf{p} = [x, y, z]^T$ where $\mathbf{p} \in V$. The displacement $\mathbf{u}$ of a particle $\mathbf{p}$ is defined as $\mathbf{u}(\mathbf{p}) = [u, v, w]^T$ so that the particle $\mathbf{p}$ is moved by the deformation to the new location $\mathbf{p} + \mathbf{u}$. The strain energy (also called internal potential energy [80], referring [82] for derivation) of a linear elastic body is defined as:

$$E_{strain} = \int_V \epsilon^T \sigma dV/2 \tag{16}$$

where the engineering strain vector $\epsilon = [\epsilon_x, \epsilon_y, \epsilon_z, \gamma_{xy}, \gamma_{xz}, \gamma_{yz}]^T$ consists of:

$$\epsilon_x = \frac{\delta u}{\delta x}, \epsilon_y = \frac{\delta u}{\delta y}, \epsilon_z = \frac{\delta u}{\delta z}, \gamma_{xy} = \frac{\delta v}{\delta x} + \frac{\delta u}{\delta y}, \gamma_{xz} = \frac{\delta w}{\delta x} + \frac{\delta u}{\delta z}, \gamma_{yz} = \frac{\delta v}{\delta z} + \frac{\delta w}{\delta y} \tag{17}$$

This can be rewritten in matrix form as $\epsilon = \mathbf{B}\mathbf{u}$ where

$$\mathbf{B} = \begin{pmatrix} \frac{\delta}{\delta x} & 0 & 0 \\ 0 & \frac{\delta}{\delta y} & 0 \\ 0 & 0 & \frac{\delta}{\delta z} \\ \frac{\delta}{\delta y} & \frac{\delta}{\delta x} & 0 \\ \frac{\delta}{\delta z} & 0 & \frac{\delta}{\delta x} \\ 0 & \frac{\delta}{\delta z} & \frac{\delta}{\delta y} \end{pmatrix}$$

The stress vector σ is related to the strain vector through Hooke's law [80]:

$$\sigma = \mathbf{M}\epsilon \tag{18}$$

where M is the material matrix. For a homogenous and isotropic material this matrix is

defined by the Lamé material constant λ and shear modulus μ:

$$\mathbf{M} = \begin{pmatrix} \lambda + 2\mu & 0 & 0 & 0 & 0 & 0 \\ 0 & \lambda + 2\mu & 0 & 0 & 0 & 0 \\ 0 & 0 & \lambda + 2\mu & 0 & 0 & 0 \\ 0 & 0 & 0 & \mu & 0 & 0 \\ 0 & 0 & 0 & 0 & \mu & 0 \\ 0 & 0 & 0 & 0 & 0 & \mu \end{pmatrix}$$

The Lamé's material constant and shear modulus are directly related to the Young's modulus E and Poisson's ratio ν for isotropic materials as follows [12].

$$E = \frac{\mu(2\mu + 3\lambda)}{\mu + \lambda} \tag{19}$$

$$\nu = \frac{\lambda}{2(\mu + \lambda)} \tag{20}$$

So, the material matrix can be rewritten for isotropic materials as:

$$\mathbf{M} = \frac{E}{(1+\nu)(1-2\nu)} \begin{bmatrix} 1-\nu & \nu & \nu & 0 & 0 & 0 \\ \nu & 1-\nu & \nu & 0 & 0 & 0 \\ \nu & \nu & 1-\nu & 0 & 0 & 0 \\ 0 & 0 & 0 & (1-2\nu)/2 & 0 & 0 \\ 0 & 0 & 0 & 0 & (1-2\nu)/2 & 0 \\ 0 & 0 & 0 & 0 & 0 & (1-2\nu)/2 \end{bmatrix}$$

where E is the Young's modulus and ν is the Poisson's ratio. The total potential energy is the sum of the internal energy and the external energy. For a conservative system, to achieve equilibrium state the loss in the external potential energy during the loading process must be equal to the work done. So, the total potential energy can be written:

$$E(\mathbf{u}) = \frac{1}{2} \int_V (\mathbf{B}\mathbf{u})^T \mathbf{M} (\mathbf{B}\mathbf{u}) dV - \int_V \mathbf{f}^T \mathbf{u} dV \tag{21}$$

where $\mathbf{f}$ is the external force. E is a functional of the displacement functions $\mathbf{u}$. The principle of finite element modelling is to decompose the whole volume or domain into many
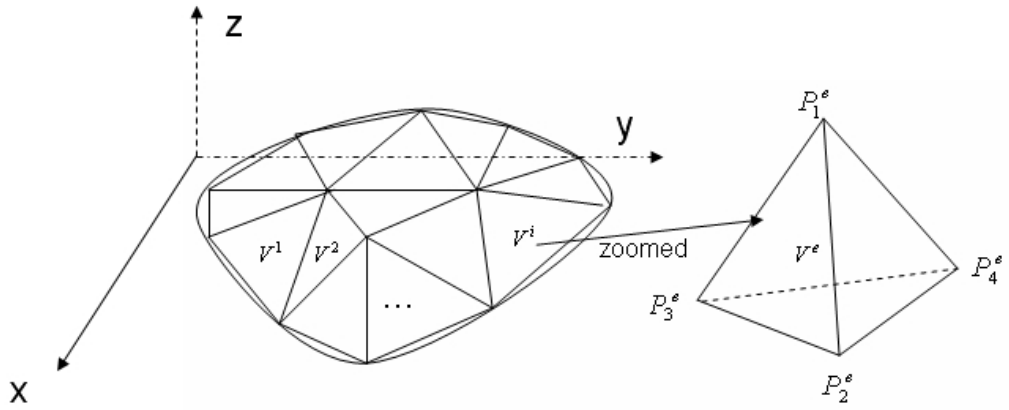
FIGURE 16 – Division of an object into elements and illustration of a tetrahedron.

finite elements, to establish equilibrium equations for each element, to combine all elements into a system equilibrium equation, and finally to solve the equation to find the displacements. By assembling all element equations into one system equation, the boundary conditions for the system equation can be used. For the global system to achieve equilibrium, the principle of the minimum total potential energy requires that the total potential energy be minimal. The superior advantage of the finite element method is that it employs comprehensively local information and can characterize detail variations during the deformation process, while much computation is needed in consideration of variation details.

The general total potential energy was formulated previously. From now on, the detailed derivation is focused on one particular element. In the derivation, constant strain tetrahedra are assumed. Figure 16 shows the volume subdivided into finite elements, while Figure 17 shows the real subdivision in implementation.

For a given element V^e, the total potential energy can be written as follows:

$$E^e(\mathbf{u}^e) = \frac{1}{2} \int_{V^e} (\mathbf{u}^e)^T \mathbf{B}^T \mathbf{M} \mathbf{B} \mathbf{u}^e dV^e - \int_{V^e} \mathbf{f}^T \mathbf{u}^e dV^e \qquad (22)$$

The nodes of each element V^e are denoted P_i^e, where i is the index of the four nodes of the element (see Fig. 16). $\mathbf{u}_i^e$ is used to denote the four nodal displacements of a tetrahedron. These displacements are used to compute the displacement at any given point

47
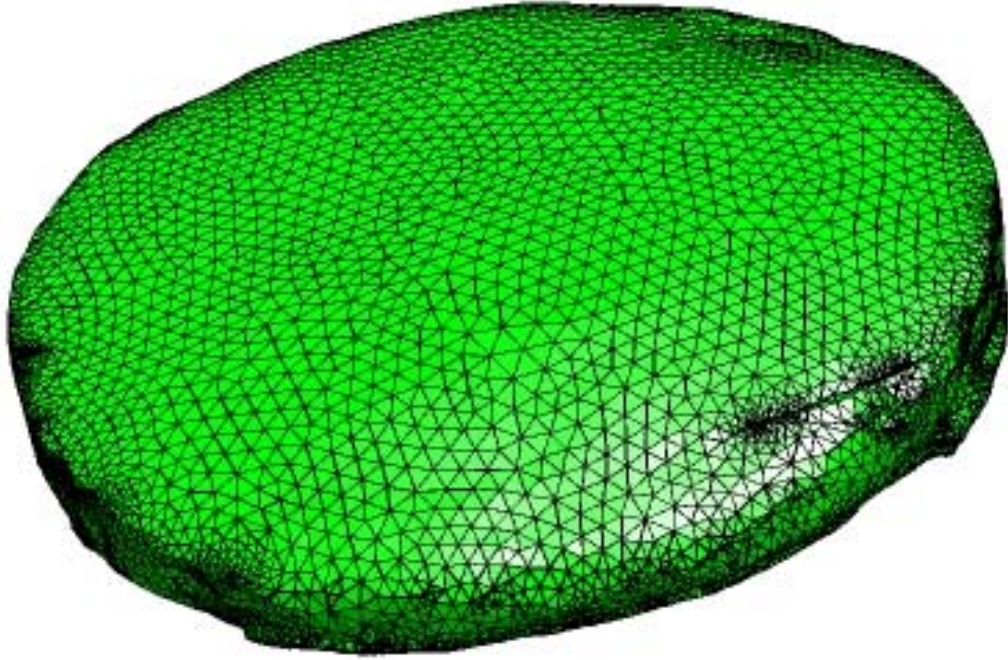
FIGURE 17 – Division of volume liver for implementation.

$p = \begin{bmatrix} x & y & z \end{bmatrix}^T$ inside the element V^e using linear interpolation:

$$\mathbf{u}(\mathbf{p}) = \sum_{i=1}^{4} N_i^e(\mathbf{p})\mathbf{u}_i^e \tag{23}$$

The shape functions $N_i^e(\mathbf{p})$ are the natural coordinates of the tetrahedrons. They are related to the global coordinates $x,\ y$ and z by the shape function as follows:

$$\begin{bmatrix} 1 \\ x \\ y \\ z \end{bmatrix} = \begin{bmatrix} 1 & 1 & 1 & 1 \\ x_1 & x_2 & x_3 & x_4 \\ y_1 & y_2 & y_3 & y_4 \\ z_1 & z_2 & z_3 & z_4 \end{bmatrix} \begin{bmatrix} N_1^e(\mathbf{p}) \\ N_2^e(\mathbf{p}) \\ N_3^e(\mathbf{p}) \\ N_4^e(\mathbf{p}) \end{bmatrix} \tag{24}$$

By inverting the matrix in the right side of the equation, the shape functions can be written as:

$$N_i^e(\mathbf{p}) = \frac{1}{6V^e}(a_i + b_i x + c_i y + d_i z), i = 1, 2, 3, 4 \tag{25}$$

48

Here,

$$V^e = \frac{1}{6} \begin{vmatrix} 1 & 1 & 1 & 1 \\ x_1 & x_2 & x_3 & x_4 \\ y_1 & y_2 & y_3 & y_4 \\ z_1 & z_2 & z_3 & z_4 \end{vmatrix},$$

$$a_1 = \begin{vmatrix} x_2 & x_3 & x_4 \\ y_2 & y_3 & y_4 \\ z_2 & z_3 & z_4 \end{vmatrix}, \ b_1 = - \begin{vmatrix} 1 & 1 & 1 \\ y_2 & y_3 & y_4 \\ z_2 & z_3 & z_4 \end{vmatrix},$$

$$c_1 = \begin{vmatrix} 1 & 1 & 1 \\ x_2 & x_3 & x_4 \\ z_2 & z_3 & z_4 \end{vmatrix}, \ d_1 = - \begin{vmatrix} 1 & 1 & 1 \\ x_2 & x_3 & x_4 \\ y_2 & y_3 & y_4 \end{vmatrix},$$

$$a_2 = - \begin{vmatrix} x_1 & x_3 & x_4 \\ y_1 & y_3 & y_4 \\ z_1 & z_3 & z_4 \end{vmatrix}, \ b_2 = \begin{vmatrix} 1 & 1 & 1 \\ y_1 & y_3 & y_4 \\ z_1 & z_3 & z_4 \end{vmatrix},$$

$$c_2 = - \begin{vmatrix} 1 & 1 & 1 \\ x_1 & x_3 & x_4 \\ z_1 & z_3 & z_4 \end{vmatrix}, \ d_2 = \begin{vmatrix} 1 & 1 & 1 \\ x_1 & x_3 & x_4 \\ y_1 & y_3 & y_4 \end{vmatrix},$$

$$a_3 = \begin{vmatrix} x_1 & x_2 & x_4 \\ y_1 & y_2 & y_4 \\ z_1 & z_2 & z_4 \end{vmatrix}, \ b_3 = - \begin{vmatrix} 1 & 1 & 1 \\ y_1 & y_2 & y_4 \\ z_1 & z_2 & z_4 \end{vmatrix},$$

$$c_3 = \begin{vmatrix} 1 & 1 & 1 \\ x_1 & x_2 & x_4 \\ z_1 & z_2 & z_4 \end{vmatrix}, \ d_3 = - \begin{vmatrix} 1 & 1 & 1 \\ x_1 & x_2 & x_4 \\ y_1 & y_2 & y_4 \end{vmatrix},$$

$$a_4 = - \begin{vmatrix} x_1 & x_2 & x_3 \\ y_1 & y_2 & y_3 \\ z_1 & z_2 & z_3 \end{vmatrix}, \ b_4 = \begin{vmatrix} 1 & 1 & 1 \\ y_1 & y_2 & y_3 \\ z_1 & z_2 & z_3 \end{vmatrix},$$

$$c_4 = - \begin{vmatrix} 1 & 1 & 1 \\ x_1 & x_2 & x_3 \\ z_1 & z_2 & z_3 \end{vmatrix}, \quad d_4 = \begin{vmatrix} 1 & 1 & 1 \\ x_1 & x_2 & x_3 \\ y_1 & y_2 & y_3 \end{vmatrix}$$

So, substituting the shape function (Eq. 23) into the total potential energy (Eq. 22), the following expression of the total potential energy yields for each element:

$$E^e(\mathbf{u}^e) = \frac{1}{2} \int_{V^e} \sum_{i=1}^{4} \sum_{j=1}^{4} (\mathbf{u}_i^e)^T \mathbf{B}^T \mathbf{M} \mathbf{B} \mathbf{u}_j^e dV^e - \int_{V^e} \sum_{i=1}^{4} \mathbf{f}^T \mathbf{u}_i^e dV \tag{26}$$

For the element to achieve equilibrium state, the principle of the minimum potential energy requires that the total potential energy for the element to be minimal. That is, its variation is zero:

$$\delta E^e(\mathbf{u}^e) = 0 \tag{27}$$

Note that

$$\delta E^e(\mathbf{u}^e) = \sum_{1}^{4} \frac{\partial E^e}{\partial \mathbf{u}_i^{e1}} \delta \mathbf{u}_i^{e1} + \sum_{1}^{4} \frac{\partial E^e}{\partial \mathbf{u}_i^{e2}} \delta \mathbf{u}_i^{e2} + \sum_{1}^{4} \frac{\partial E^e}{\partial \mathbf{u}_i^{e3}} \delta \mathbf{u}_i^{e3},$$

where $\mathbf{u}_i^{e1}$, $\mathbf{u}_i^{e2}$ and $\mathbf{u}_i^{e3}$ are the three coordinate components in the displacement space. The element equilibrium equation is equivalent to the following equation:

$$\frac{\partial E^e}{\partial \mathbf{u}_i^{e1}} = \frac{\partial E^e}{\partial \mathbf{u}_i^{e2}} = \frac{\partial E^e}{\partial \mathbf{u}_i^{e3}} = 0, i = 1, 2, 3, 4 \tag{28}$$

The resulting equilibrium equation can be written as follows:

$$\sum_{j=1}^{4} \left(\int_{V^e} (N_i^e)^T \mathbf{B}^T \mathbf{M} \mathbf{B} N_e^j dV^e \right) \mathbf{u}_j^e - \int_{V^e} \mathbf{f}^T \mathbf{u}_i^e dV^e = 0, i = 1, 2, 3, 4 \tag{29}$$

Here the partial derivatives of the displacement vectors were used:

$$\frac{\partial \mathbf{u}^e}{\partial x} = \sum_{i=1}^{4} \frac{\partial N_i^e(x)}{\partial x} \mathbf{u}_i^e \tag{30}$$

$$\frac{\partial \mathbf{u}^e}{\partial y} = \sum_{i=1}^{4} \frac{\partial N_i^e(x)}{\partial y} \mathbf{u}_i^e \tag{31}$$

$$\frac{\partial \mathbf{u}^e}{\partial z} = \sum_{i=1}^{4} \frac{\partial N_i^e(x)}{\partial z} \mathbf{u}_i^e \tag{32}$$

Rewriting (Eq. 32) and stacking the four nodal vectors of a tetrahedron into one nodal vector for the element, the following equilibrium equation yields:

$$K^e \mathbf{U}^e = \mathbf{F}^e \tag{33}$$

where K^e is a 12×12 element stiffness matrix, $\mathbf{U}^e = [\mathbf{u}_1^e, \mathbf{u}_2^e, \mathbf{u}_3^e, \mathbf{u}_4^e]^T$ is a 3×1 nodal displacement vector for the element V^e, and $\mathbf{F}^e$ is a 12×1 force vector. Now the minimization problem of the total potential energy is reduced into a linear equation but the boundary conditions of the element nodal displacement vector remain unknown. It is needed to assemble all element equilibrium equations into a systematic equation as follows so that the global boundary conditions can be employed:

$$K\mathbf{U} = \mathbf{F} \tag{34}$$

The dimension of the global stiffness matrix is $3m \times 3m$ and the dimension of the global force vector is $3m$, where m is the number of total nodes.

D. NEO-HOOKE'S HYPERELASTIC MODEL

Live tissue is flexible and is closer to rubber in its properties. Hence, it may be possible to adequately model the response of the liver tissue using the hyperelastic material models developed for rubbers. ABAQUS software [67] has several hyperelastic models designed for rubber materials. The general polynomial form of strain energy potential of a hyperelastic model is

$$W = \sum_{i+j=1}^{N} C_{ij}(\bar{I}_1 - 3)^i(\bar{I}_2 - 3)^3 + \sum_{i=1}^{N} \frac{1}{D_i}(J^{el} - 1)^{2i},$$

where W is the strain energy potential per reference volume, N is the polynomial order, C_{ij} and D_i are temperature-dependent material parameters, I_1 and I_2 are the first and second deviatoric strain invariants, defined as

$$\bar{I}_1 = \bar{\lambda}_1^2 + \bar{\lambda}_2^2 + \bar{\lambda}_3^2,$$

$$\bar{I}_1 = \bar{\lambda}_1^{-2} + \bar{\lambda}_2^{-2} + \bar{\lambda}_3^{-2}$$

where the deviatoric stretches $\bar{\lambda}_i = J^{-1/3}\lambda_i, \quad \lambda_i$ are the principle stretches, J is the total volume ratio and J^{el} is the elastic volume ratio. The D_i parameters allow for the inclusion of compressibility. Neo-Hooke's Hyperelastic materials are described in terms of a strain energy potential, which defines the strain energy stored in the material per unit of reference volume (volume in the initial configuration) as a function of the strain at that point in the material. The energy potential function W is

$$W = C_{10}(\bar{I}_1 - 3) + \frac{1}{D_1}(J^{el} - 1)^2,$$

The initial shear modulus μ_0 and bulk modulus $K_0 = 2/D_1$ can be estimated from the compression test. Therefore, the material parameters C_{10} and D_1 can be computed as follows.

$$C_{10} = \frac{\mu_0}{2}, \ D_1 = \frac{2}{K_0}.$$

One can refer to [67, 81] for more details about the neo-Hooke model and other hyperelastic models.

E. SUMMARY

In this chapter, basic concepts in continuum mechanics were reviewed. The basic application steps of the finite element method were described in solving partial differential equations. The famous Dirichlet boundary problem was used in the derivation process for illustration. The linear elastic model was formulated to describe the elastic response of an object using the minimum total potential principle, the equilibrium equation was established, and the detailed procedure of the finite element method to solve the equilibrium was expounded in content. The neo-Hooke's hyperelastic was also introduced briefly to predict soft tissue deformation.

CHAPTER V
PREPROCESSING OF SOFT TISSUES

To perform finite element analysis of soft tissue deformation, preprocessing techniques are needed: image segmentation, mesh generation, and measurement of the tissue mechanical properties. This chapter describes how each one of these pre-processing techniques has been performed in the present study.

A.   EQUIPMENT SETUP AND IMAGE ACQUISITION

In order to hold the liver tissue for image scanning, a general purpose device (*"testing chamber"*) (Figure 18 for the chamber was developed and its detailed parts in Figure 19). Such chamber was used for both Micro-CT scanning and CBCT scanning. Inside the chamber, the height of the support where the lamb liver was put can be adjusted for optimal scanning position. At the top portion, there are counterbalance and lever functions to impose force loads. It can be used to induce measurable deformations which can be captured by high resolution Micro-CT and CBCT machines (Figure 12 and Figure 14). Figure 20 shows the test chamber with Micro-CT machine. For the lamb liver scanning, the source voltage used is 75 KeV, the current was $0.107\ mA$, and the detector resolution was $0.1mm$. The testing chamber is formed of a cylindrical plexiglass compartment. The tissue is placed on the bottom of the compartment and an aluminium probe with half spherical tip touches the upper surface of the tissue. The specification of the diameter of the half spherical tip was $5mm$ but the actual one from the mechanical shop was $4.7mm$.

For the finite element modeling and validation purpose, the following procedure was performed to acquire the images under certain force loads. The Micro-CT and CBCT machine have automatic reconstruction softwares to achieve high quality stacks of two-dimensional axial slices to be used in this study.

FIGURE 18 – Test chamber to hold the lamb liver.

Item	Title	Quantity
1	Main Chamber	1
2	Chamber Lid	2
3	Slide Block	1
4	Linear Bearing	2
5	Probe Shaft	1
6	Weight Tray	1
7	Probe Tip	1
8	Counterbalance	1
9	Lever Fulcrum	1
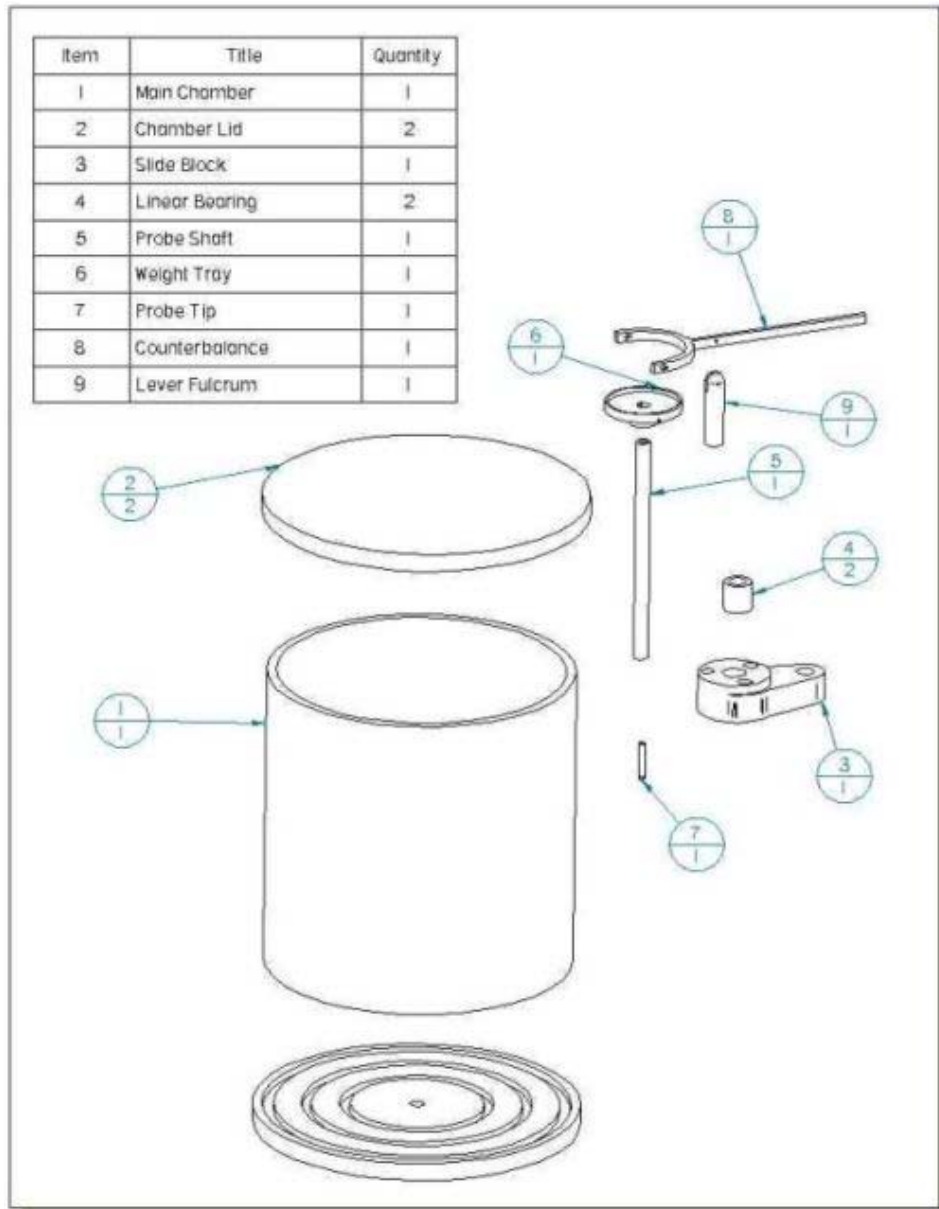
FIGURE 19 – Detailed parts description of the test chamber.

- Scan a piece of soft tissue using Micro-CT or Cone-Beam CT machine to collect a stack of undeformed images.

- Apply the small force load. After five minutes and the tissue reaches equilibrium, the deformed tissue was scanned.

- Segment the collected images of the undeformed tissue to reconstruct the liver and generate its volume mesh.

- Select a finite element model to perform finite element analysis on the meshed object with the same force loads and same boundary conditions as those for the object in the experiment.

- Superimpose the deformed objects from simulation and the corresponding ones in the experiment. Compute their volume difference as the model errors and measure the vertical displacements of the probe tip in the experiment and the simulation for comparison purpose.

B.   IMAGE SEGMENTATION

The acquired CT-reconstructed images of the lamb liver are segmented to perform finite element analysis. A typical Micro-CT liver image, as shown on the right of Figure 21, consists of cylindrical plexiglass compartment view, liver, indentor, and the air between liver tissue and the plexiglass compartment. For some images acquired at the beginning or at the end of the imaging process, the liver tissue or indentor may not exist inside the scanned images.

To separate the liver from the rest of the image, a robust variable thresholding technique was developed. The algorithm flow chart is described in Figure 22. Due to the fixation of the plexiglass compartment during scanning and the consistency of scanning orientation, the shape views of the plexiglass compartment in each slice are the same. Therefore, the plexiglass compartment can be stripped off from all scans. In each data set,
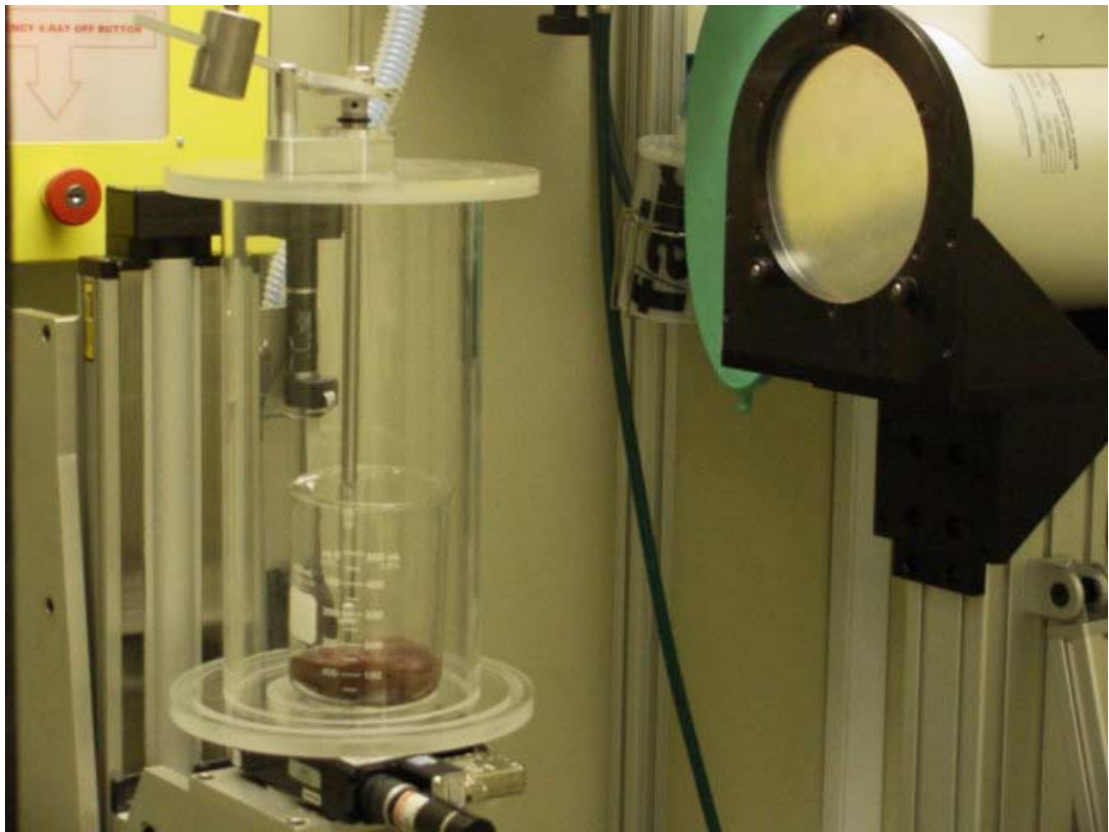
FIGURE 20 – Test chamber with Micro-CT machine.
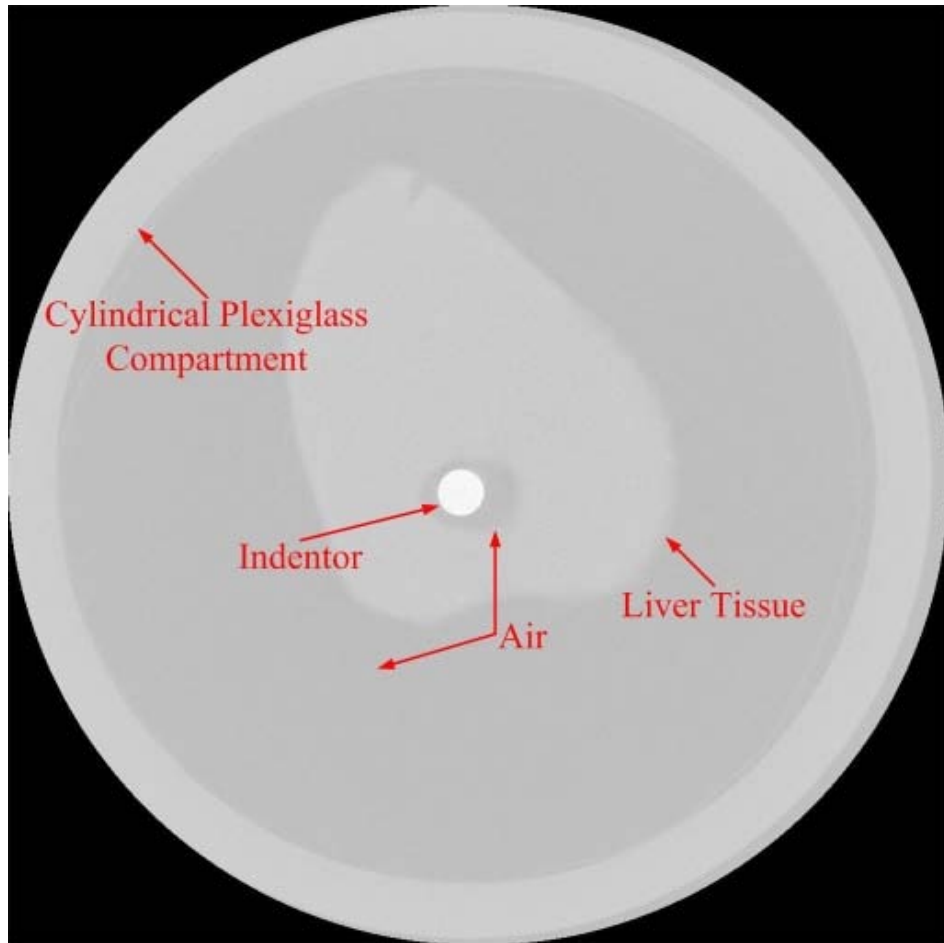
FIGURE 21 – Normal Micro-CT image.
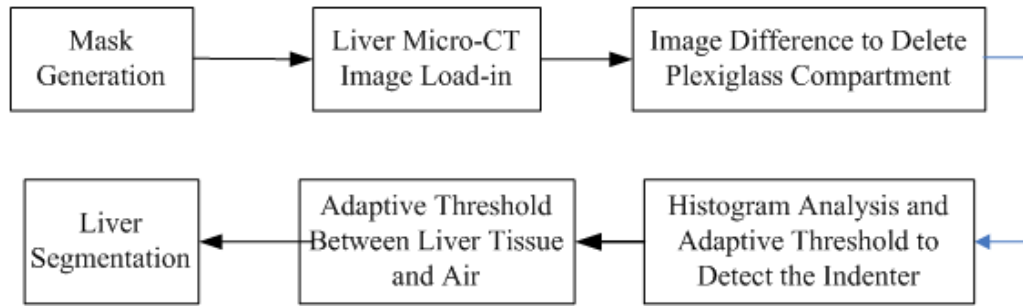
FIGURE 22 – Segmentation Algorithm Flow Chart.

for the first several slices containing no liver, the image intensity is set to 0. The intensity of the indentor is obviously higher than those of the air and the liver tissue. Hence, the indentor can be stripped off by automatically searching a threshold from the image histogram. Finally, the liver object can be obtained by stripping off the air in the same way. Fig. 23 shows three 2D slices of automatically segmented liver (top row), and their corresponding slices through manual segmentation. Figure 24 shows the superimposing of the algorithm segmented 3D image (red) and manually segmented 3D image (green).

C.   VOLUME MESH GENERATION

Volume mesh generation consists in decomposing the object volume into finite union of geometrically simple and bounded elements. Mesh generation techniques have been developed for different contexts and were aimed at different applications. A mesh is called structured if it consists of quadrilateral elements in 2D or hexahedral elements in 3D. Otherwise, it is called unstructured. In the medical imaging field, tetrahedral elements are by far the most commonly used forms of unstructured meshes. Such shape elements fit well the complex topology of the anatomical structures. Unstructured mesh generation techniques can be classified into three main categories: Octree, Delaunay, and Advancing Front [83].
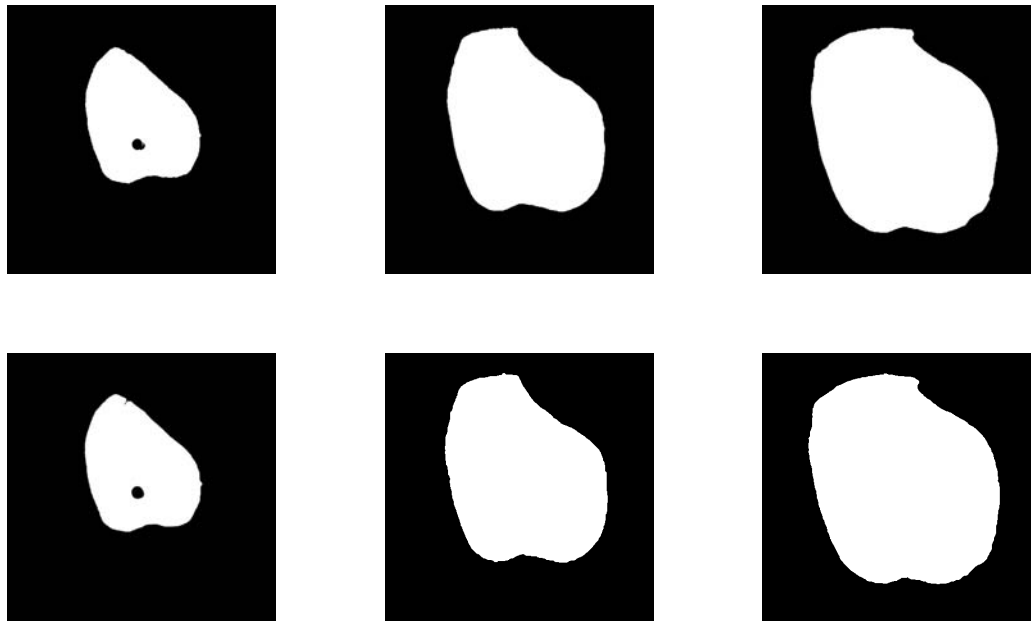
FIGURE 23 – Three automatically segmented 2D slices from liver scanning in the first row and their corresponding 2D slices segmented by hand in the second row.

FIGURE 24 – Superimposing of algorithm segmented object (red) and manually segmented object (right).

1. Octree

The Octree technique was originally developed by Mark Shephard et al. [84]. The geometric model is surrounded by a set of cubes, which are recursively subdivided until the desired resolution is reached. Irregular cells are created where cubes intersect the surface. Tetrahedra are generated from both the irregular cells on the boundary and the internal regular cells. Figure 25(a) shows the equivalent two-dimensional quadtree decomposition of a model.

2. Delaunay

The most popular tetrahedral meshing techniques are those utilizing the Delaunay criterion. The Delaunay criterion states that any object node must not be contained within the circumference of any tetrahedra within a mesh. Figure 25(b) is a simple two dimensional illustration of the validity of this criterion. A typical approach is to first mesh the boundary of the geometry to provide an initial set of nodes. The boundary nodes are triangulated, and new nodes are then inserted incrementally into the existing mesh, redefining the triangles or tetrahedrons locally according to the Delaunay criterion. It is the method chosen to define where to locate the interior nodes that distinguishes one Delaunay algorithm from another. The main drawback of the Delaunay meshing techniques is that they often require the object to be convex. This difficulty can be overcome, when an initial surface discretization is specified, by splitting non convex objects into small convex objects, and enforcing boundary conditions at seams between sub-objects.

3. Advancing Front

First, the surface boundary is triangulated and then tetrahedrons are built progressively inward from the triangulated surface. An active front is maintained where new tetrahedrons are formed ([85]). Figure 25(c) is a simple two-dimensional example of the advancing front, where triangles have been formed at the boundary. As the algorithm pro-
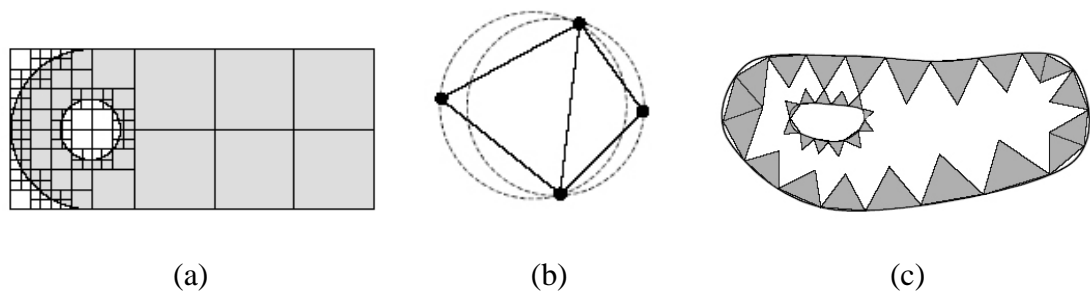
FIGURE 25 – Illustration of three methods of mesh generation: (a) Quadtree decomposition - the object is subdivided by cubes and recursively subdivided until the desired resolution is reached, (b) Delaunay decomposition - based on the criterion where any node must not be contained within the circumference of any tetrahedra, (c) Advancing front decomposition - the surface boundary is triangulated and then tetrahedrons are built progressively inward from the triangulated surface.

gresses, the front will advance to fill the remainder of the area with triangles. In three-dimensional space, for each triangular facet on the front, an ideal location for a new fourth node is computed. The algorithm selects either the new fourth node or an existing node to form a new tetrahedron. Intersection checks are required to ensure that the tetrahedrons do not overlap as opposing fronts advance towards each other.

In medical imaging, some mesh generators are created for image registration and tissue deformation ([86, 87]). This work is interested in generating high quality tetrahedral meshes that conform to the input surface mesh. To achieve this goal, the images are segmented first and then the segmented images are converted into a stereolithographic file which is input into NETGEN ([88]) to generate a 3D mesh of the liver. The NETGEN uses the advancing front technique combined with Delaunay tessellation. It is fast, robust and can generate high quality meshes. The density of tetrahedrons can be set by the user automatically. Figure 26 shows the procedure to generate volume meshes from a stack of medical images.

D.   MEASUREMENT OF MATERIAL PARAMETERS

Material parameters play an active role in biomechanical modeling. It is important to obtain mechanical properties of the soft tissue. Based on the composite structures, soft
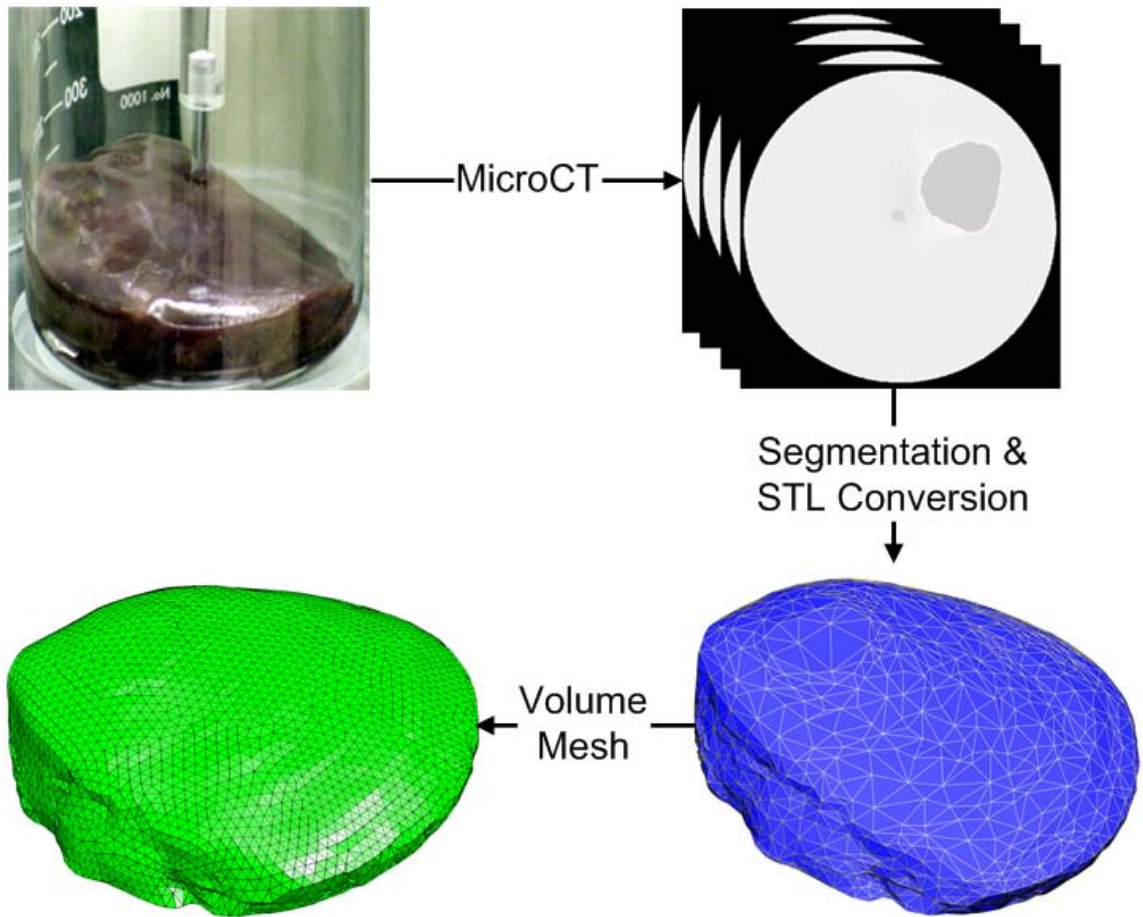
FIGURE 26 – Procedure from image acquisition, segmentation and stl conversion, to volume mesh generation.

tissues are generally in two classes, solid with tissue approximately even distributed, and hollow with some portions of the inside are empty. For a solid soft tissue such as liver, it consists of a dense connective tissue which can be assumed as isotropic, homogeneous, and incompressible. The mechanical properties of a type of tissue can be measured in both *in vivo* [10, 14, 15] and *ex vivo* [11] state. It is more attractive to measure the tissue properties using *in vivo* tests than using *ex vivo* tests. However, it is difficult to measure the tissue properties in *in vivo* state due to the accessibility, uncontrolled boundary conditions, noises, and motions.

In this study, two pieces of lamb liver were cut. One piece has a cylindrical shape with height of 0.5 *in*, and it is used for a compression test. A Dynamic Mechanical Analysis (DMA) machine mode RSA3 (TA Instruments, Wilmington, DE) in Dr. Roger Bradshaw lab was used for the compression test. The DMA measures the mechanical properties of materials as a function of time, temperature, and frequency. The linear drive motor in DMA provides precise stress control. It can be used for the compression test. Figure 27 shows the DMA machine with the piece of lamb liver for a compression test. From the compression test, the stress-strain curve was obtained as shown in Figure 28 and the stress-strain curve for the strain less than 10.5% in Figure 29. The test took 58 seconds to finish. The compression rate was 0.1 millimeters per second and the temperature was basically kept at 23.79^oC during the compression process. For the linear elastic model, the Young's modulus $E_0 = 11055$ *Pa* is the median of the eight pairs of stress-strain data in Figure 29. The Poisson's ratio of 0.4 is used from literature [11, 15]. For the neo-Hooke's hyperelastic model, the initial shear modulus $\mu_0 = 3948$ *Pa* and bulk modulus $K_0 = 18425$ *Pa* are computed from Figure 29, the Young's modulus E, and the above Poisson's ratio ν as follows.

$$\mu_0 = \frac{E_0}{2(1+\nu)}, \quad K_0 = \frac{E}{3(1-2\nu)}. \tag{35}$$

E. SUMMARY

In this chapter, the preprocessing procedure was described in details from equip-

FIGURE 27 – The Dynamic Mechanical Analysis (DMA) machine with RSA3 mode (TA Instruments, Wilmington, DE) from Dr. Roger Bradshaw lab, and the liver tissues for a compression test.
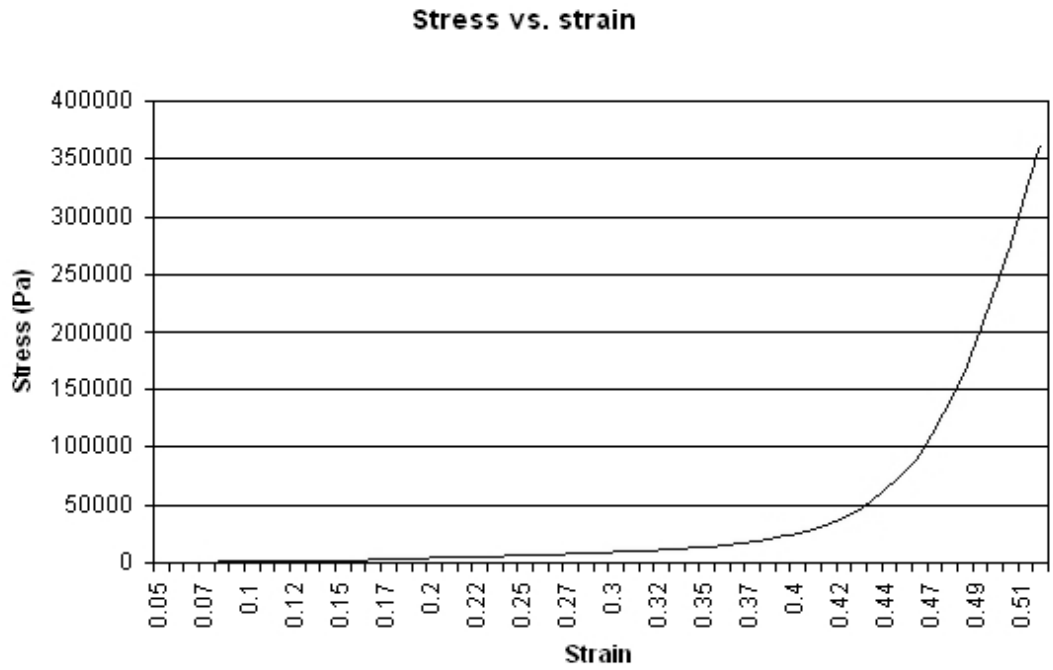
Stress vs. strain

FIGURE 28 – The stress vs. strain curve for the compression test in Figure 27.
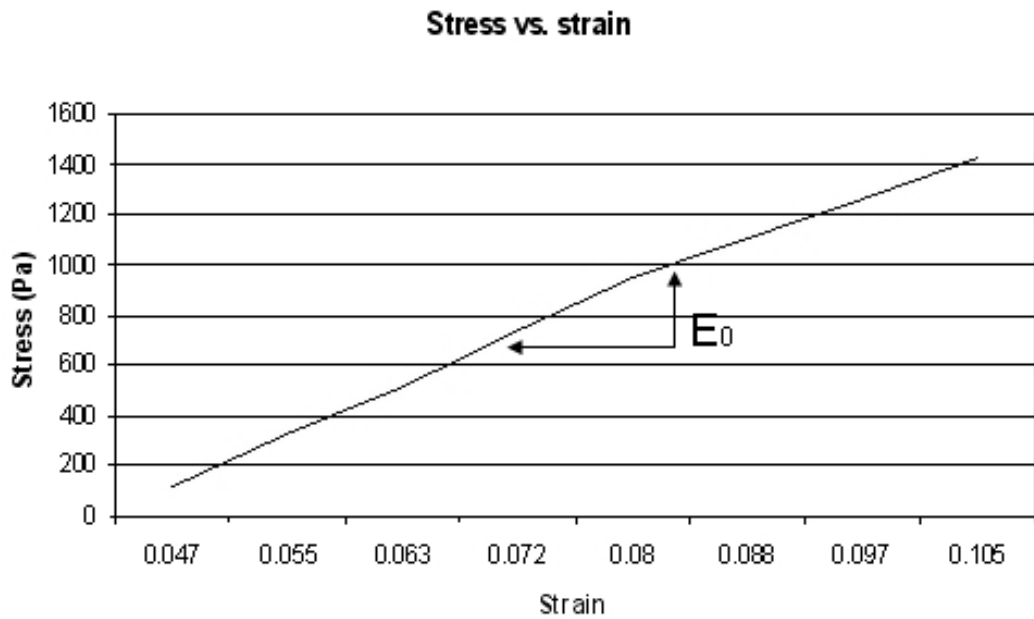
Stress vs. strain

FIGURE 29 – The stress vs. strain curve for the compression test in Figure 27.

ment setup, image acquisition, image segmentation, and volume mesh generation to material parameters measurement. A compact chamber for image acquisition was made to hold the liver tissue for scanning and imposing force load on the indentor. One automatic algorithm was developed to strip off the liver tissue from the compact chamber, indentor, and the air. The volume mesh generation of the separated liver was introduced before finite element analysis is performed. In the last, a DMA machine was used for compression test to obtain the material parameters for the linear elastic model and the neo-Hook's hyperelastic model. The material parameters obtained are slightly different but close to those recorded in literature.

CHAPTER VI
FINITE ELEMENT MODELING OF LIVER TISSUE

This chapter will use the linear elastic model and the neo-Hooke's hyperelastic model to describe the liver tissue responses under small force loads. The study uses the high resolution images acquired using recent Micro-CT and CBCT imaging technologies which can identify very small changes of the liver tissue in surface, and volume. Theoretically, for very small force loads, the soft tissue essentially behaves as a linear elastic material. However, such behavior does have some discrepancy between those observed and measured from the real experiments.

A.   PROPOSED FE MODEL VALIDATION SYSTEM

Before one geometric or physical model is employed in real surgical practice to monitor or predict the soft tissue changes, validation should be performed to verify the applicability of the model to the target soft tissue so that the prediction reflects the real changes in operations. So, it is important to establish a solid validation system to test the model to be employed in surgical simulation. This section presents a validation standard of FE models to verify the LEM and the NHM ([89]). The image acquisition is an important step for FE model validation and is integrated into the validation standard. The criterion of validation is the maximum vertical deformation of the soft tissue and the difference of the volumes between the undeformed liver and the deformed liver. The proposed soft tissue validation system can be described as follows.

A piece of soft tissue is scanned using Micro-CT to collect a stack of images of the undeformed tissue. Four force loads (5, 10, 20, and 40 grams) are gradually applied to the lever of the chamber, adding 5 grams force load at a time interval of 5 minutes. For each force load, the deformed tissue is scanned when the equilibrium is reached. The collected

images, both for the undeformed tissue and the deformed tissues, are then segmented and a volume mesh is generated. A FE model (LEM, or NHM) is selected to perform FE analysis on the meshed undeformed object with the same force loads and same boundary conditions as those for the object in the experiment (see Fig. 27:top-right for deformed object). Finally, the deformed objects from simulation and the corresponding ones in the experiment are superimposed, and their volume difference is computed. The measurements are performed of the maximum vertical displacements of the liver tissues in the experiment and the simulation for purpose of comparison. The simulation of finite element analysis was performed as expounded in Chapter VII. The proposed soft tissue validation procedure to quantify the modeling error can be summarized as follows.

- Scan a piece of soft tissue using Micro-CT or Cone-Beam CT machine to collect a stack of undeformed images.

- Apply a small force load on the lever. After 5 minutes, the deformed tissue is scanned.

- Repeat the last step following additional force loads to collect scans of the deformed tissue at different force loads.

- Segment the collected images of the undeformed tissue to reconstruct the liver and generate its volume mesh.

- Select a finite element material model (the LEM, or the NHM, one at a time) to perform finite element analysis on the meshed object with the same force loads and same boundary conditions as those for the object in the experiment.

- Superimpose the deformed objects from simulation and the corresponding ones in the experiment. Compute their volume differences as the model errors and measure the vertical displacements of the probe tip in the experiment and the simulation for comparison purposes.

The weights are put on the lever and the force loads are applied vertically downwards. The indentor contact with the liver surface, also the stereolithographical file, and mesh generation are left in the next chapter for details.

B.   RESULTS AND DISCUSSIONS

To compute the deformation volume difference between the deformed object from simulation and the one from experiment, a cylinder with radius of $20mm$ and height of $19.6mm$ is used to cover the deformed region. The cylinder is positioned vertically and centered at the probe contact, and the top surface of the cylinder takes the shape of the undeformed liver surface. The deformed volume is computed by the number of voxels between the deformed surface and the top surface of the cylinder. The vertical displacements of the probe tip in real deformation and simulation are estimated from the acquired images and from the simulated object. All the deformed volume using the LEM, and the NHM and their differences with the real deformed volume are listed in Table 1. The vertical displacements of the probe tip are listed in Table 1. The abbreviations RD, LED, and NHD stand for the vertical displacement of the probe tip in real deformation, and the vertical displacements of the probe tip in simulation using the LEM and the NHM, respectively. RDV, LEDV, NHDV, LEVD, and NHVD stand for the real deformed volume, the deformed volumes using the LEM, and the NHM and their volume differences from the real deformed volume, respectively. Figure 5 shows the tip displacements listed in the real experiments, and in the simulations for the LEM and NHM in Table 1. Figure 30, Figure 31, Figure 32, and Figure 33 show the superimposing of the deformed liver from simulation and the real deformed liver from experiments for the three models on the left and their corresponding wire-zooms of the contact regions under the force loads of 5, 10, 20, and 40 grams respectively. This can be seen from Figure 30, Figure 31, Figure 32, and Figure 33. For the superimposing purpose, the volumes from the experiments needed to be smoothed to generate the suitable meshes. The choice of the indentor tip with such small tip was to reduce the functional friction of the lever and the entire chamber. From Table 1, Figure 30,

Figure 31, Figure 32, and Figure 33, it can be seen that for small force loads ($< 40g$), the LEM is more applicable to the modeling of the lamb liver tissue. One can conclude that the liver deformation using the LEM is less than the real deformation of the liver in depth, but is gradually approaching it with the increasing force load from 5 grams to 20 grams (Table 1). At the force load of 40 grams, the liver deformation using the LEM exceeds the real deformation of the liver $3.39mm$ in depth as shown in Table 1. One can conclude also that the liver deformation using the LEM is gradually going deeper with the increasing force load. At the force load of 40 grams, the liver deformation using the LEM is greater than the real deformation. The liver deformation using the NHM is gradually approaching the real deformation with the increasing force load. The root mean square values of the nodal displacements for each FE model are computed for different force loads (Table 2). These results are consistent with the results in Table 1. The strain repartition plots from ABAQUS for the two FE models and for the force loads up to 40 grams, show that the maximal strains do not exceed 10%. Figure 29 shows that the material behaves approximately linear for the strain less than 10%. This confirms that all simulations are carried out in the small deformation regime. The observed difference in displacements for the LEM might be attributed to the following cause: the elastic components in the two models generating slight different elastic effects, and the existing geometric nonlinearity which was not considered in the experiment and the simulation in the LEM. As the larger force is applied to the probe, it moves more deeply into the tissue and more tissues are pushed out. Consequently, there is more surface area in contact with the probe to provide support. For the NHM, the geometric nonlinearity is considered in simulation.

Finite element analysis was performed on the entire liver but found that the volume difference of the deformed volume using modeling and the real deformed volume is quite small, less than 20% of the volume difference within the cylinder. Table 3 shows the entire deformed volumes from real experiment and simulations. WRDV, WLEDV, WNHDV, WLEVD, and WNHVD stand for the entire real deformed volume, the entire deformed volumes using the LEM, and the NHM and their corresponding volume differences with the real deformed volume, respectively. The small volume differences of the simulated
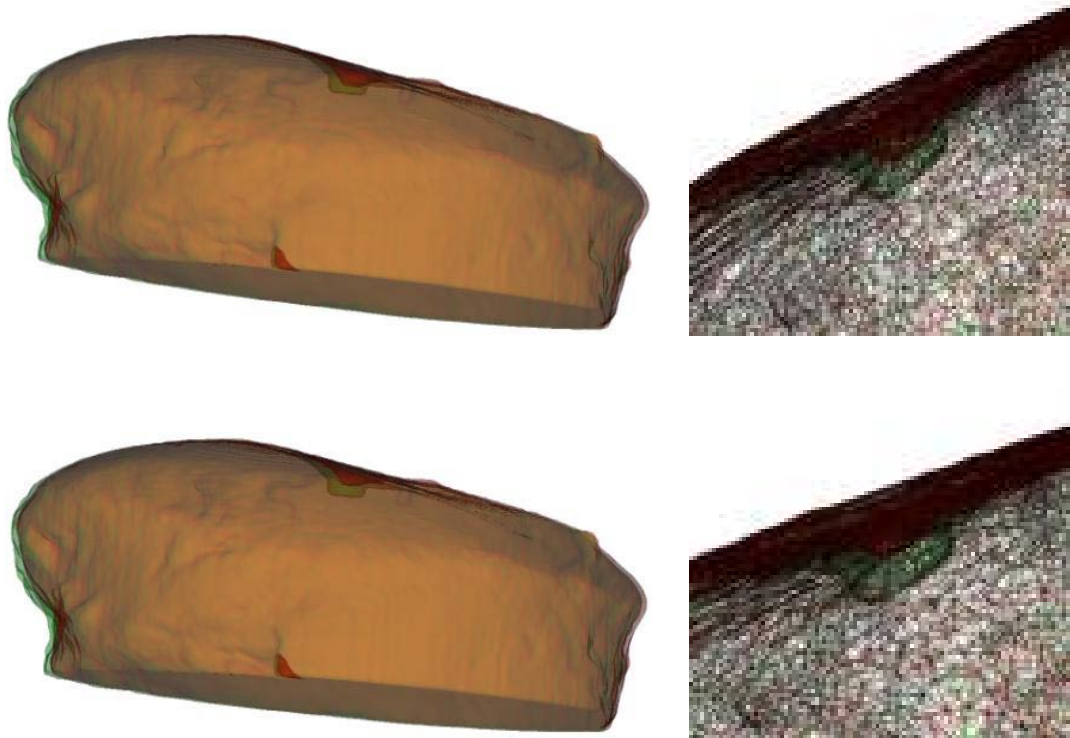
FIGURE 30 – Superimposing of the simulated livers and the real deformed ones under the force load 5 grams and their corresponding wire-framed zooms around the contact regions for the LEM and NHM respectively from top row to bottom row; The green indicates the real deformation and the red indicates the deformation from simulation.
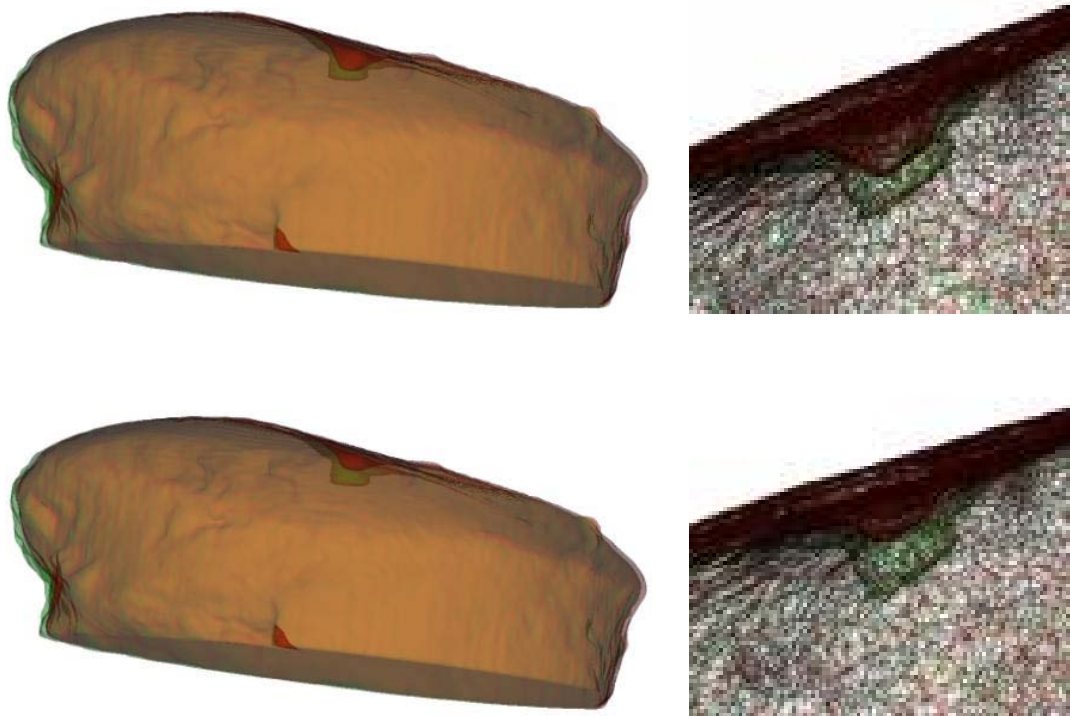
FIGURE 31 – Superimposing of the simulated livers and the real deformed ones under the force load 10 grams and their corresponding wire-framed zooms around the contact regions for the LEM and NHM respectively from top row to bottom row; The green indicates the real deformation and the red indicates the deformation from simulation.

FIGURE 32 – Superimposing of the simulated livers and the real deformed ones under the force load 20 grams and their corresponding wire-framed zooms around the contact regions for the LEM and NHM respectively from top row to bottom row; The green indicates the real deformation and the red indicates the deformation from simulation.
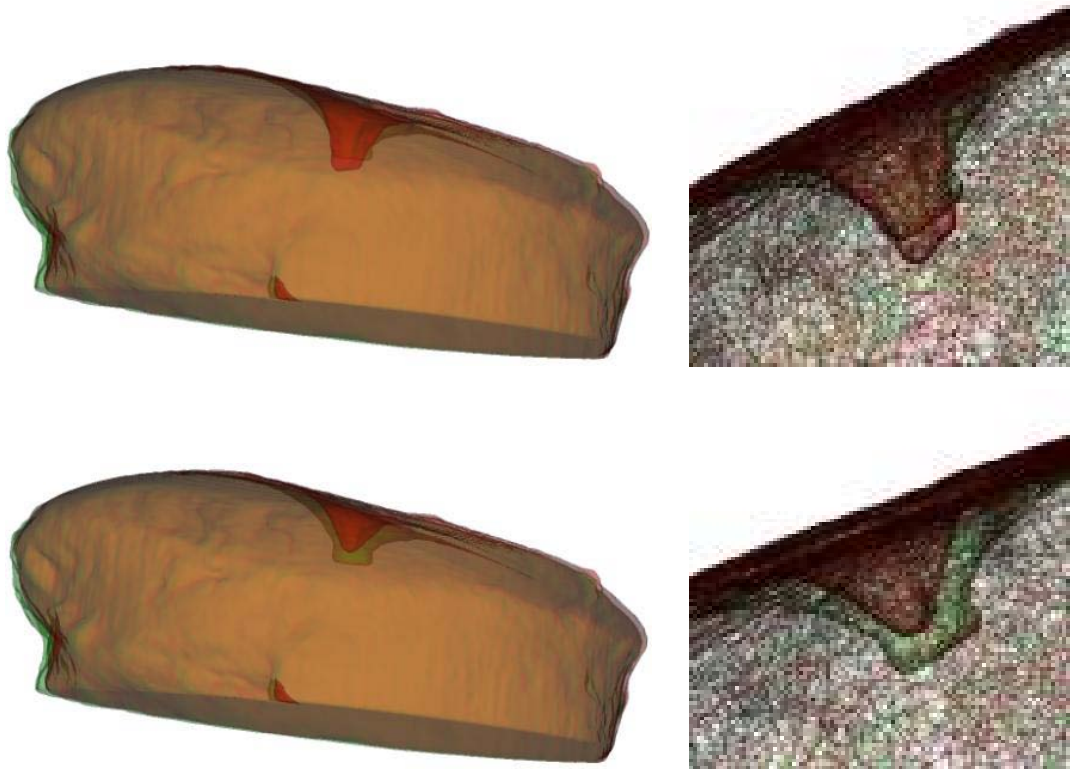
FIGURE 33 – Superimposing of the simulated livers and the real deformed ones under the force load 40 grams and their corresponding wire-framed zooms around the contact regions for the LEM and NHM respectively from top row to bottom row; The green indicates the real deformation and the red indicates the deformation from simulation.

TABLE 1
VERTICAL DISPLACEMENTS RD OF THE PROBE TIP, THE SIMULATED
DISPLACEMENTS LED AND NHD USING THE LEM, AND NHM RESPECTIVELY,
REAL DEFORMED VOLUMES RDV, DEFORMED VOLUMES LEDV, NHDV USING
THE LEM AND THE NHM RESPECTIVELY, AND THEIR VOLUME DIFFERENCES
LEVD, NHVD WITH THE REAL DEFORMED VOLUMES.

		(unit)	5 g	10 g	20 g	40 g
Tip Disp.	RD	mm	1.8	2.6	4.2	6.2
	LED	mm	0.77	1.54	4.39	9.59
	NHD	mm	0.68	1.32	2.57	5.04
Volume	RDV	mm^3	956	1075	1241	1527
	LEDV	mm^3	765	835	996	1228
	NHDV	mm^3	736	773	882	1051
Volume Diff.	LEVD	mm^3	191	240	245	299
	NHVD	mm^3	220	302	359	476

TABLE 2
RMS VALUES (MM) FOR THE LEM AND NHM FOR DIFFERENT FORCE LOADS.

	5 g	10 g	20 g	40 g
LEM	0.0488	0.0976	0.1952	0.3944
NHM	0.0307	0.0611	0.1213	0.2397

TABLE 3
THE ENTIRE REAL DEFORMED VOLUMES WRDV, THE ENTIRE DEFORMED
VOLUMES WLEDV AND WNHDV USING THE LEM AND THE NHM
RESPECTIVELY, AND THEIR VOLUME DIFFERENCES WLEVD AND WNHVD
WITH THE ENTIRE REAL DEFORMED VOLUMES.

	WRDV mm^3	WLEDV mm^3	WLEVD mm^3	WNHDV mm^3	WNHVD mm^3
5 g	16158	16190	42	16192	44
10 g	16009	16182	173	16187	177
20 g	15985	16169	184	16179	194
40 g	15925	16143	218	16161	236
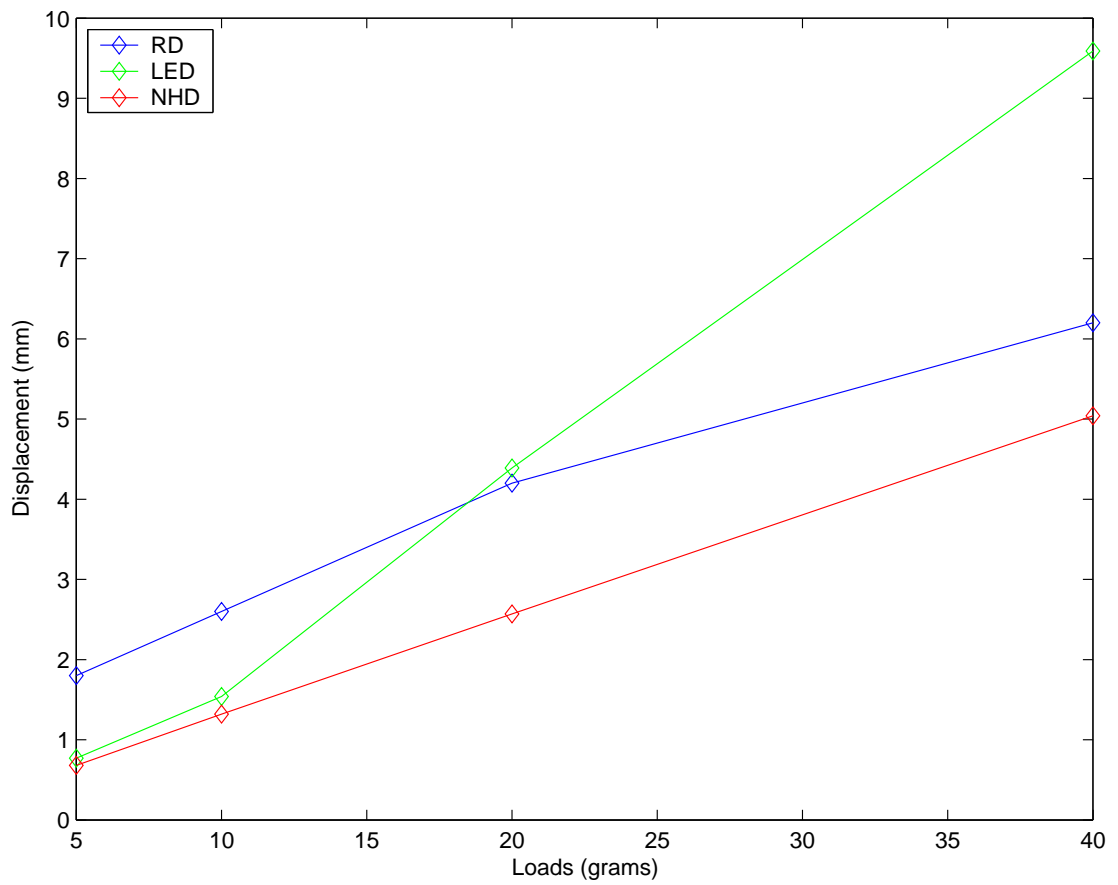
FIGURE 34 – The indentor tip displacements for the real deformation and the simulated deformation using the LEM and NHM under different force loads.

volumes using three models and the real deformed volumes are due to the very small force loads, mainly elastic property, non-linear geometry, and the interaction of liver boundaries touching the test chamber for the real deformed volume. There will be detailed discussions in a further report focusing on finite element modeling over different regions around the contact.

The purpose for this study aimed for applications of computer aided surgery inside an endoscopy. Finite element analysis was performed on the entire liver but found that the volume difference of the deformed volume using modeling and the real deformed volume outside the above mentioned cylinder is quite small, less than 20% of the volume difference within the cylinder. Study focusing on region-of-interest finite element modeling will be reported in Chapter IX.

C. SUMMARY

This study presented FE modeling of soft tissues from Micro-CT images. This type of images shows the volume and surface shape changes for small force loads. The FE method is used to analyze the lamb liver deformations under certain force loads using the LEM and the NHM. The deformations are measured from the models and compared to the real deformations measured by the experiment setup. It is found that the LEM is applicable to the lamb liver for the force load under $20g$. Also, the LEM is more applicable to lamb liver than the NHM for small force loads ($< 40g$) and that the NHM is closer to reality than the NHM for the force loads greater than $40g$. The presented results show that the range of the force loads where the three models perform well has large overlaps. The comparability of the results presented herein to the *in vivo* tissue, which is valuable for future surgery simulation design, is beyond the scope of this work and will be investigated in future studies.

CHAPTER VII
DEBRIEFING OF FE MODELING AND ANALYSIS

This chapter addresses the details of stereolithographical file (STL) generation, volume mesh generation, the contact of the indentor with the volume mesh surface for finite element analysis. The stress and strain relation chart will be presented for some key nodes and elements for the nonlinear neo-Hooke's hyperelastic model.

A. STEREOLITHOGRAPHICAL FILE GENERATION

STL files describe the three-dimensional geometry of an object by a set of adjacent triangular facets [90]. Each facet is defined by both a normal vector and an ordered list of its three vertices. This order states which side of the facet contains the inside volume. The STL file is generated from the segmented binary 2D images in this study. The main steps are as follows:

- Generate triangular net.

- Classify the surface into plane segment, smooth segment, and rough segment.

- Delaunay triangulation.

- Generate STL file.

There are dedicated researches focused on each step such as [91], [92], [93] etc. In this study, a program was developed in VTK-TCL programming language [94] to generate STL file. The program used the existing libraries and functions in VTK [94]. The marching contour filter was used to generate triangular surface. The smoothing and decimation filters were also used to smooth the triangular surface and delete redundant triangles based on

the surface curvature. Figure 26 (bottom right) shows the generated STL and the surface triangles. The main steps in the program are listed as follows:

- Get the interaction user interface source.

- Set the origin and data spacing of x, y, z in 3D space.

- Set the 3D image size in x, y, z three directions.

- Create the render window if the STL is displayed on computer screen.

- Read the segmented binary 2D images automatically from the computer hard drive.

- Use the VTK marching contour filter to create surface triangles where Delaunay criterion is maintained.

- Use the smoothing filter to smooth and correct errors.

- Use the decimation filter to delete redundant triangles.

- Set the background and object color.

- Use the VTK write and save functions to output triangles and save the resulted object geometry.

B.   VOLUME MESH GENERATION

Chapter V briefly introduced the volume mesh generation for finite element modeling. As mentioned, NETGEN [88] was used for volume mesh generation in this study. It is open source for education purpose and can be downloaded at the NETGEN web site. This section addresses the details of volume mesh generation using the NETGEN [88] software.

NETGEN is an automatic mesh generation tool with a graphical user interface. Its C++ library can be linked into other applications such as its linked to the CVIP surgical project for direct mesh generation. NETGEN can generate triangular or quadrilateral meshes in 2D, and tetrahedral meshes in 3D. The 3D volume input can be in the standard
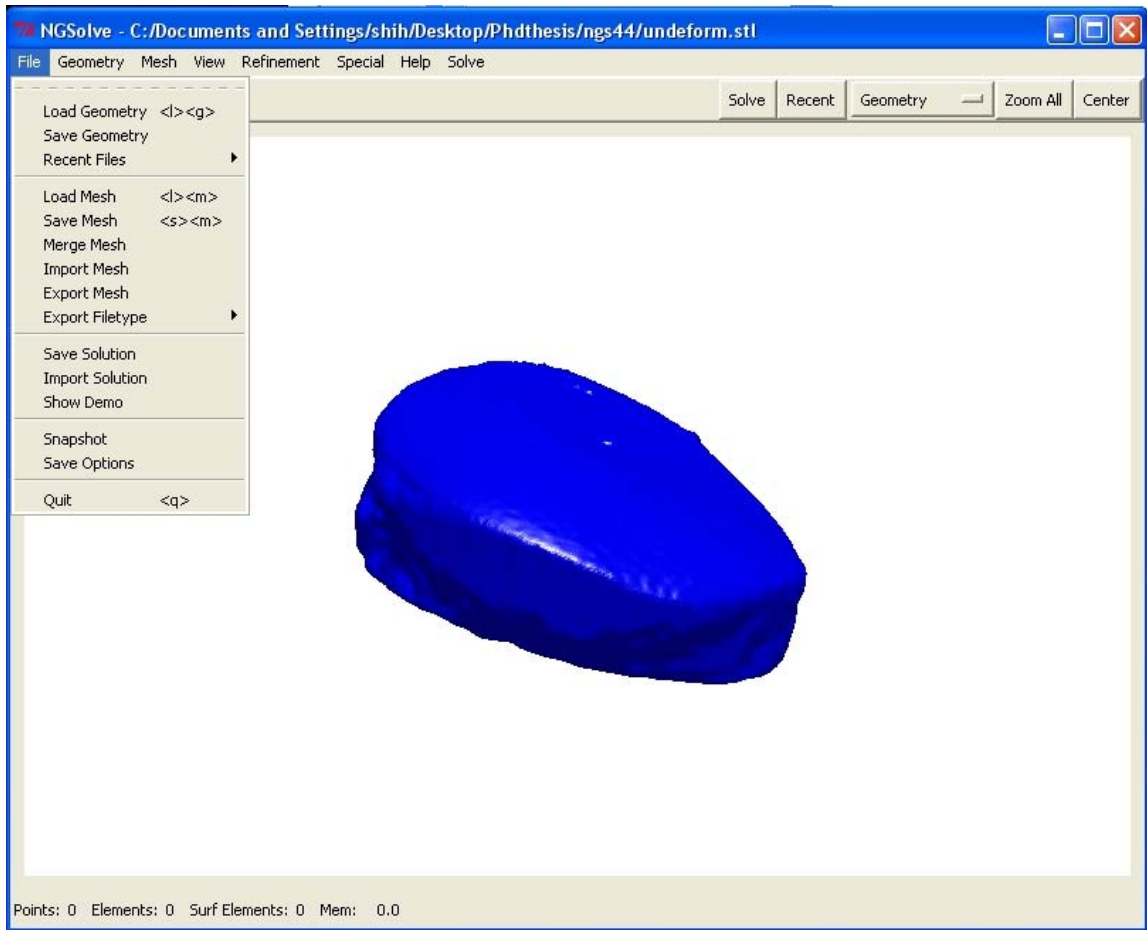
FIGURE 35 – NETGEN interface panel showing the File menus to load the object.

STL file format, or constructive solid geometry format [88]. NETGEN is an advanced mesh generation software which combines the Delaunay criterion and front advancing meshing techniques. It contains modules for mesh optimization and hierarchical mesh refinement. Figure 35 shows NETGEN interface panel and the File menu and its submenus to load the STL geometry. The option Load Geometry can be selected to load the STL file from the computer hard drive. Under the Geometry menus adjacent to the File menus, there are several submenus can be selected for smoothing and deleting some inconsistent triangles on the geometry surface. Figure 36 shows two options, one for the general submenus and the other for editing geometry submenus under the Geometry. At this step, some inconsistent surface triangles need to be removed by marking them on the geometry.

Figure 37 shows the Mesh menu and its submenus in the NETGEN interface panel.
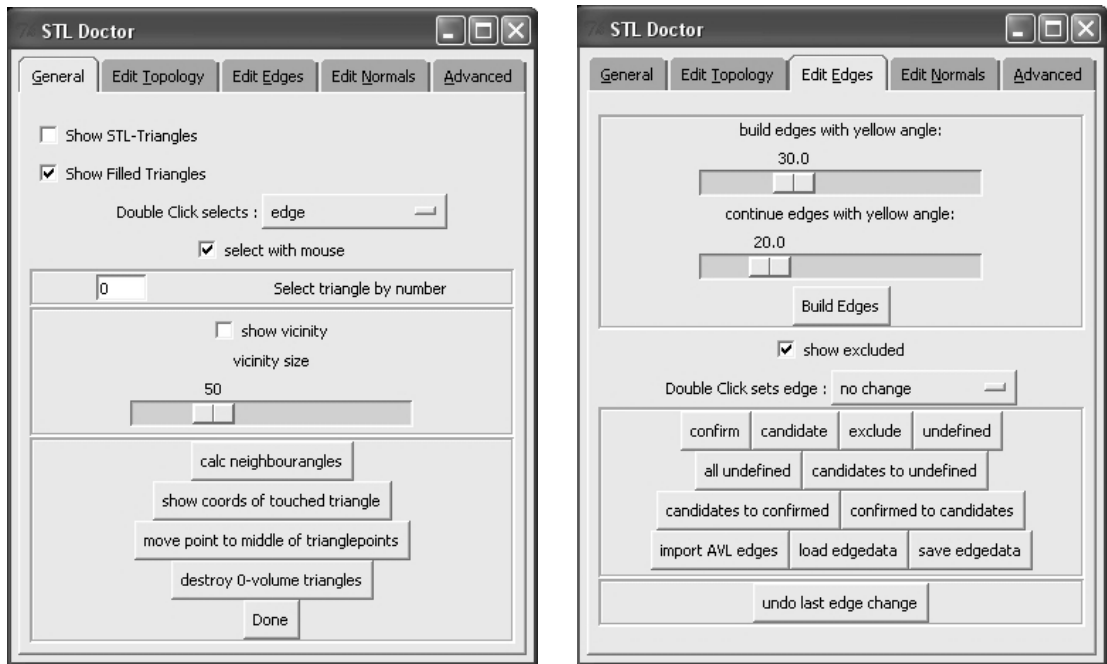
FIGURE 36 – Submenus of the Geometry in NETGEN to use STL Doctor to smooth the STL.

There is a submenu called Meshing Option which is used to select the mesh density and ratio control of the maximum side length to the minimum side length. Figure 38 shows two options to edit and control meshes. As known, the mesh generation is based on the geometrical curvature. The definition and computation of the surface curvature has been introduced in Chapter II. If the curvature at one location is higher, the geometry surface at the location has sharper turning and the number of tetrahedra is larger in the neighborhood of the higher curvature location. If the curvature at one location is lower, the geometry surface at this location is quite flatter and the number of tetrahedra is smaller. The Meshing option controls the ratio of the maximum side length to the minimum side length of the tetrahedra. So, the number of tetrahedra around the higher curvature location can be controlled and the number of tetrahedra at the lower curvature can be increased. However, if the option choices are not consistent, a mesh generation may fail if the object surface is not smooth enough or the different inconsistence of various option selections under the menus on the NETGEN interface panel, though the mesh generation itself has a process to smooth
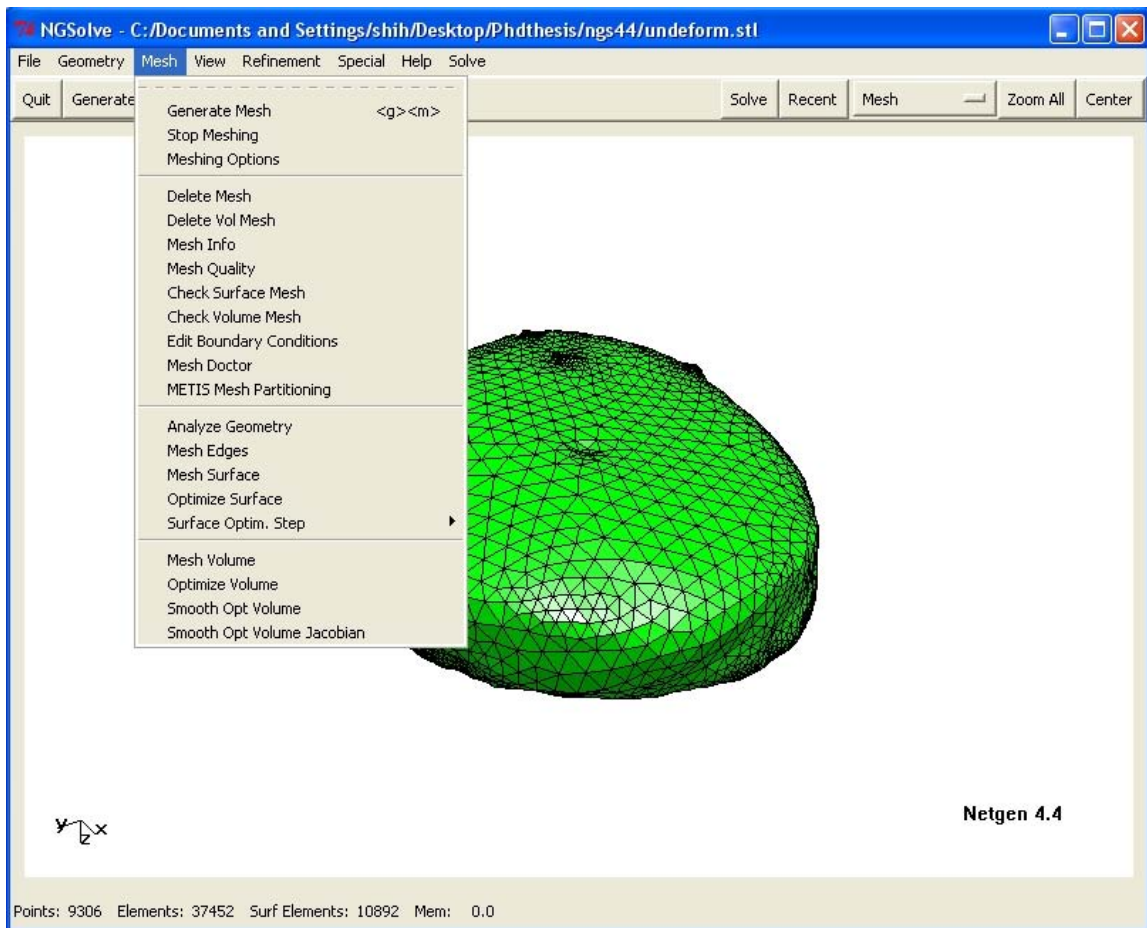
FIGURE 37 – NETGEN interface panel showing the Mesh menus and the meshed object.

the mesh. Besides the inconsistence of option selections, a common reason is that the De-launay may not be maintained for very high curvature and the choice of large element size. So, repetitive mesh generations may be needed for a desired high quality mesh.

After a mesh is generated, the generated mesh can be exported into a file by select-ing a submenus under the File menus in the NETGEN interface panel. There are thirteen file formats including the ABAQUS format available to export the volume mesh as shown in Figure 39. Inside the exported file for the ABAQUS format, the nodes with the ordered node number from the first node to the last and their coordinates are listed first. Then the elements with their connected nodes are listed from the number one element to the last. The exported volume mesh file has the *inp* extension which can be recognized by AQBAQUS finite element software.
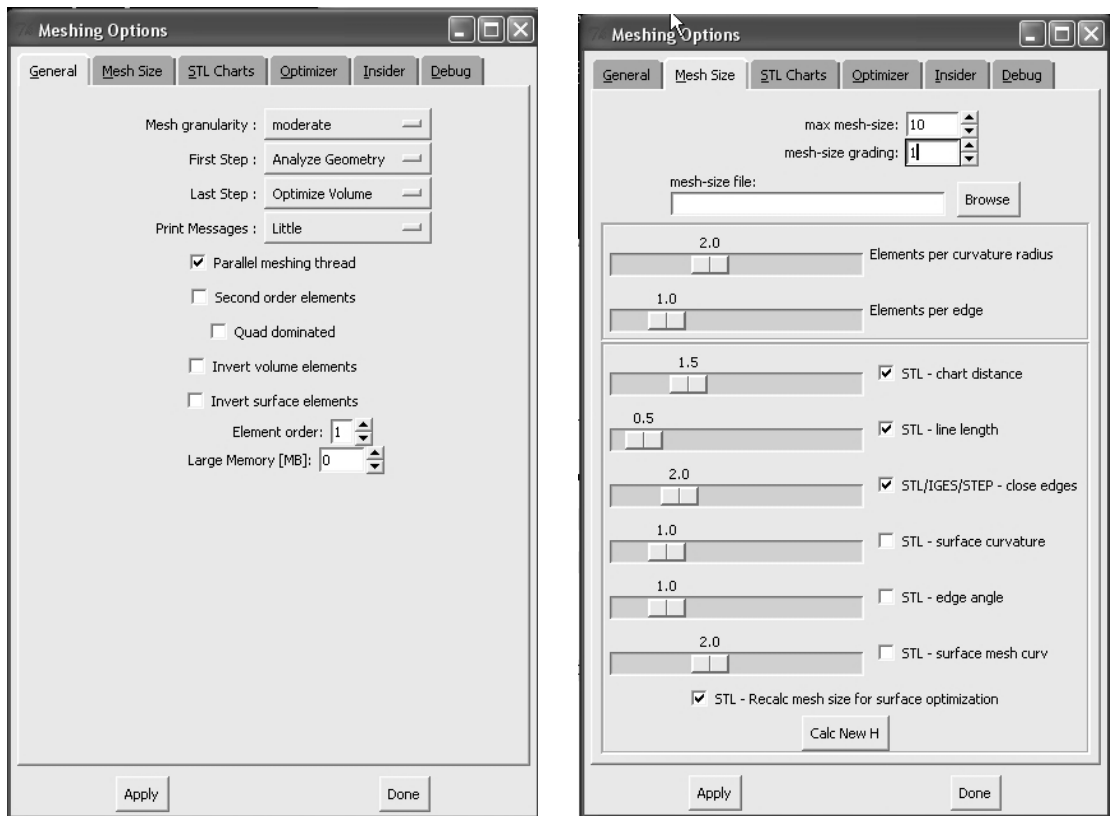
FIGURE 38 – Submenus of the Mesh in NETGEN to use the choice of options.
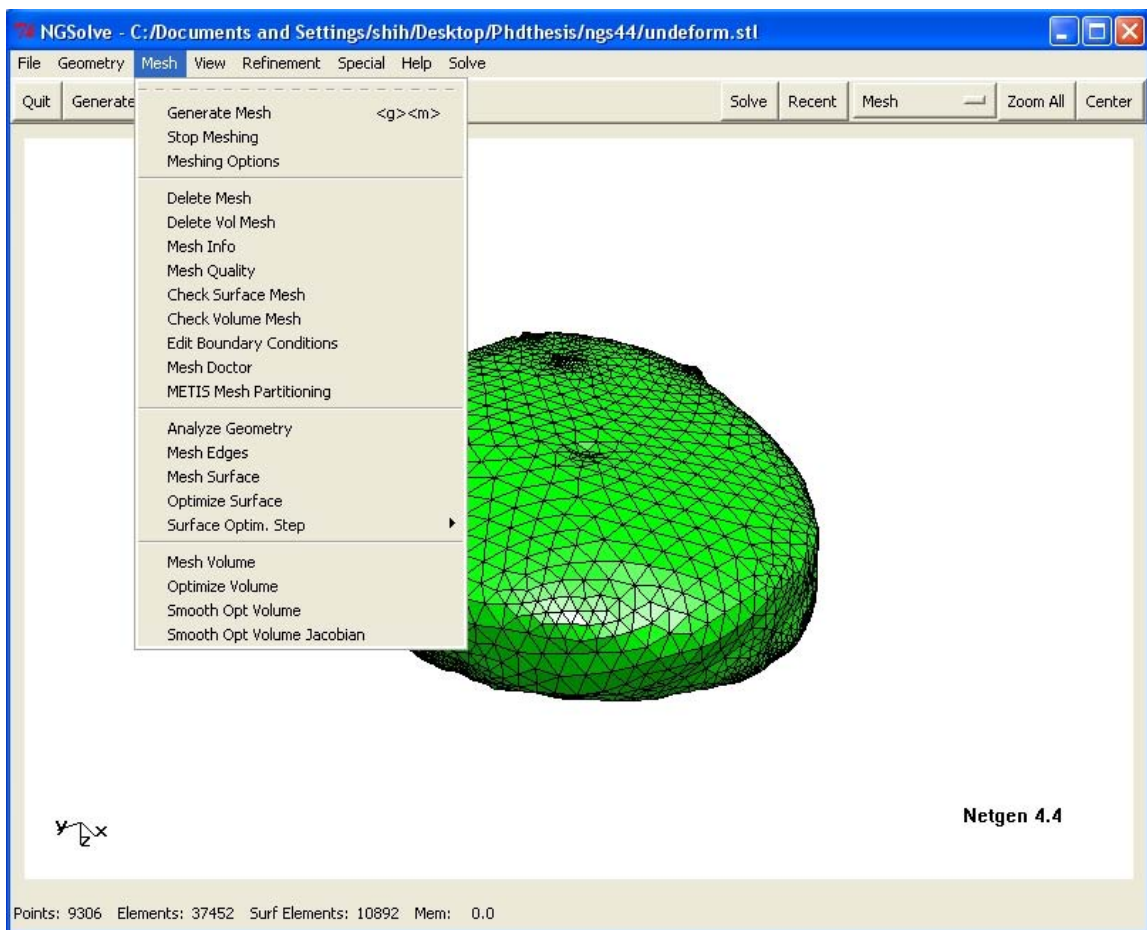
FIGURE 39 – NETGEN interface panel showing the submenus to export the volume mesh.

C.   INDENTOR CONTACT WITH MESH SURFACE

This section addresses the contact of the indentor with the surface of the volume mesh. In this study, the indentor was made of aluminum with the flat tip and was considered rigid. The liver was considered as deformable. The simulation was the surface contact simulation between the rigid indentor and the deformable liver.

The options of the small sliding and frictionless between the indentor and liver surface were selected for the actual simulations. The indentor shape is flat and its diameter is 4.76 centimeters. The liver mesh surface is quite dense so that under the indentor there are more than six nodes as required by ABAQUS manual. In actual simulation, more than thirty surface triangles around the indentor were selected to form the local contact surface so that the indentor cannot push through holes within one surface triangle. Figure 40 shows the profile codes for the indentor which is a rigid body and contacted with the liver surface. Figure 41 shows the portion of codes for the contact of the indentor with the mesh surface. It can been that the elements in the set *PickedSurf8* formed the contact surface of the liver with the rigid indentor for the neo-Hooke's hyperelastic model. The first few lines are the boundary nodes which are not related to the contact region. Figure 42 shows the indentor contact with the mesh surface of the liver tissue after the volume mesh is exported into the ABAQUS and the indentor is designed. The indentor is the cylinder with the flat tip. The indentor just touch the liver without deforming the surface. There are more than six surface triangles under the cylinder.

D.   FINITE ELEMENT ANALYSIS USING ABAQUS

In the previous sections, the generation of stereolithographical file and mesh, and the indentor contact with the mesh surface were expounded in details. In this section, finite element analysis is performed using the ABAQUS software [67]. The use of the ABAQUS step by step is illustrated. Two indentors are used, one with the half spherical tip and the other with the flat tip. The results and procedures are performed for both indentors for comparison. The deformed volumes from the linear elastic modeling and the neo-Hooke's

```
** Section: Section-1
*Solid Section, elset=_PickedSet2, material=Material-1
1.,
*End Instance
**
*Instance, name=Part-2-1, part=Part-2
        52.,          50.4,           13.
        52.,          50.4,           13.,          51.,        50.4,        13., 89.9999990194245
*Node
        1,            0.,            30.,           0.
*Nset, nset=Part-2-1-RefPt_, internal
1,
*Surface, type=REVOLUTION, name=RigidSurface_, internal
START,            0.,           30.
 LINE,            2.5,          30.
 LINE,            2.5,           0.
 LINE,            0.,            0.
 LINE,            0.,           30.
*Rigid Body, ref node=Part-2-1-RefPt_, analytical surface=RigidSurface_
*End Instance
*Nset, nset=_PickedSet10, internal, instance=Part-2-1
 1,
*Nset, nset=_PickedSet11, internal, instance=Part-2-1
 1,
*Elset, elset=PART1, instance=PART-1-1, generate
    1,  71704,        1
*Nset, nset=_PickedSet9, internal, instance=PART-1-1
  483,  529,  581,  586,  587,  589,  597,  642,  655,  685,  691,  733,  751,  755,  759,  782
  790,  802,  804,  843,  855,  856,  857,  869,  885,  892,  899,  903,  904,  906,  908,  910
  912,  948,  969,  971,  973,  975,  979,  985,  991,  992, 1002, 1004, 1005, 1007, 1026, 1037
```

FIGURE 40 – Profile for the rigid indentor

```
*Elset, elset=_PickedSurf8_S1, internal, instance=PART-1-1
  4404, 10514, 10517, 13015, 14740, 15342, 23610, 29104, 30733, 33803, 33805, 35382, 37119, 45978
 56698, 56706, 58134, 58522, 58524, 61931, 69541, 70981, 70984
*Elset, elset=_PickedSurf8_S2, internal, instance=PART-1-1
  6467, 24765, 25140, 28561, 52950, 57233, 57399, 57638, 57939, 58010, 61428, 62381, 67004, 69429
*Elset, elset=_PickedSurf8_S3, internal, instance=PART-1-1
 14029, 27415, 28357, 30380, 33801, 33807, 33951, 34194, 35018, 36479, 46251, 46818, 49348, 57635,
57639, 58153, 59835, 61929, 68713, 68714
*Elset, elset=_PickedSurf8_S4, internal, instance=PART-1-1
  1652, 11377, 11378, 23835, 24401, 28174, 32777, 33947, 34109, 36476, 36477, 37635, 46347, 48234
 48781, 51353, 51419, 55019, 57436, 57477, 58073, 58077, 58135, 64660, 66212, 68609
*Surface, type=ELEMENT, name=_PickedSurf8, internal
__PickedSurf8_S1, S1
__PickedSurf8_S2, S2
__PickedSurf8_S4, S4
__PickedSurf8_S3, S3
*End Assembly
**
** MATERIALS
**
*Material, name=Material-1
*Density
 1.1343e-09,
*Hyperelastic, neo hooke
0.001974, 108.55
**
** INTERACTION PROPERTIES
**
*Surface Interaction, name=IntProp-1
1.,
*Friction
0.,
**
** INTERACTIONS
**
** Interaction: Int-1
*Contact Pair, interaction=IntProp-1, adjust=1.
_PickedSurf8, Part-2-1.RigidSurface_
```

FIGURE 41 – Profile for liver surface contact elements and interaction.
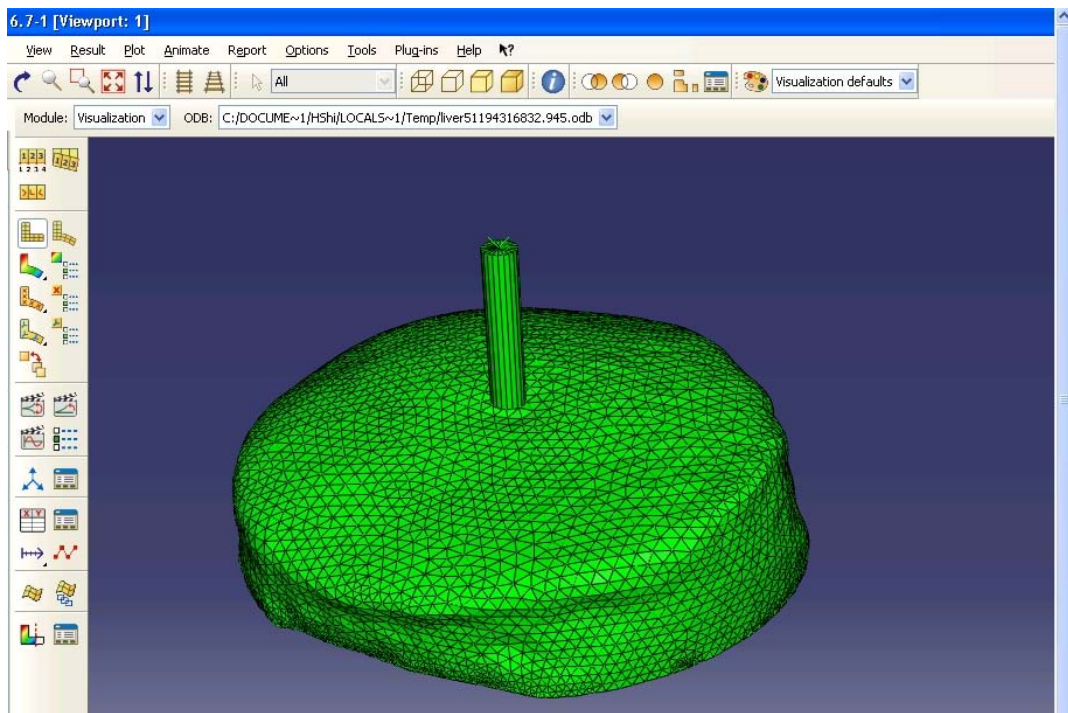
FIGURE 42 – The indentor with the flat tip touches but not deforms the mesh surface of the liver tissue.

hyperelastic modeling are presented and superimposed with the undeformed volume to show the differences. The stresses and strains for some key element nodes from the neo-Hooke's hyperelastic modeling are charted and curved. Here, the indentor is a cylinder with the flat tip.

1. Basic steps for the LEM and NHM before simulation

To perform the finite element analysis using ABAQUS, the basic steps before simulation are as follows:

- Import the volume data file into the ABAQUS. This data file was generated from NETGEN export. The liver object can be displayed in the ABAQUS interface environment as in Figure 43. The liver object is defined as Part-1.

- Design an indentor with the half spherical tip and set the reference point to the top surface central of the cylinder opposite to the indentor tip.

- Move it to touch the the liver mesh surface as shown in Figure 42. There are more than a dozen of triangles under the indentor if viewed parallel to the cylinder bar.

- Impose the restriction and boundary conditions - there are two restriction and boundary conditions: one is on the reference point to make the reference can move only vertically (in z-direction), and other is fixation of the liver tissue bottom.

- Set the force load vertically onto the indentor. The force load is the concentrated force acting on the reference point.

- The finite element simulation can be performed from the ABAQUS/CAE interface panel, or export the inp file and run simulation under the command prompt line using ABAQUS commands.

- After simulation is done, the deformed volume can be seen as in Figure 44 and the real time deformation process can be seen in video form by selecting the video option to play the deformation process.

The above steps (modules as called in ABAQUS) have specific name for finite element analysis in ABAQUS. These steps are Part for part design, Property to set the property of the part, Assembly to assembly parts together, Step for static or dynamic, Interaction for the interaction between the parts, Load to impose the force load needed and the boundary conditions on parts for simulation, Mesh to decompose the parts into tetrahedra or cubes depending on need, Job to set the duty for simulation and perform simulation, Visualization to see the simulated results, and Sketch to draw the required picture using ABAQUS. The following are detailed procedures for simulation.

Part Design the parts for simulation. The liver volume mesh file from NETGEN as part one, the rigid cylinder was designed as the indentor using the drawing tools listed in the left of the ABAQUS interface panel as shown in Figure 45. In the indentor design, the point was selected as a reference point. There is no need for the step Mesh for the liver tissue since the liver mesh is imported from a volume mesh file.
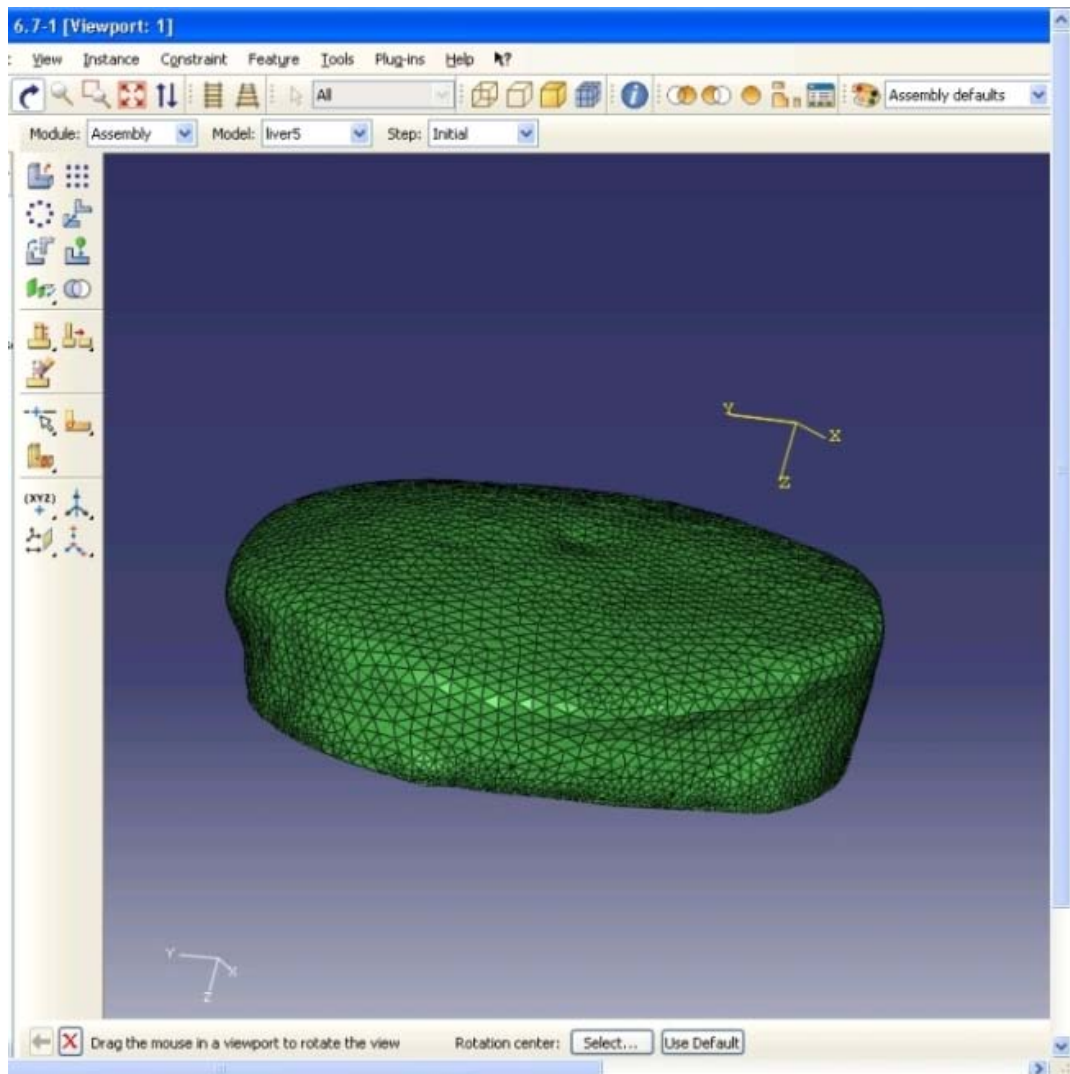
FIGURE 43 – The meshed volume from NETGEN is imported into ABAQUS.
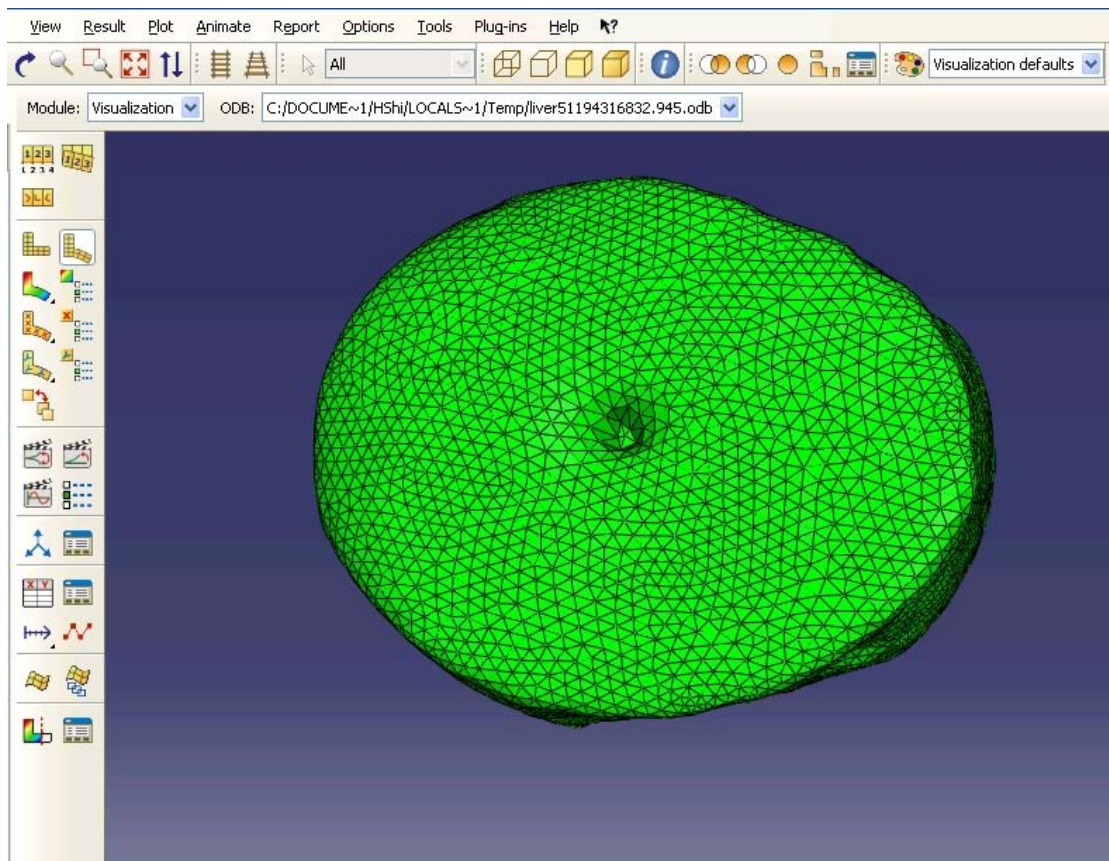
FIGURE 44 – The deformed volume after FE modeling simulation.
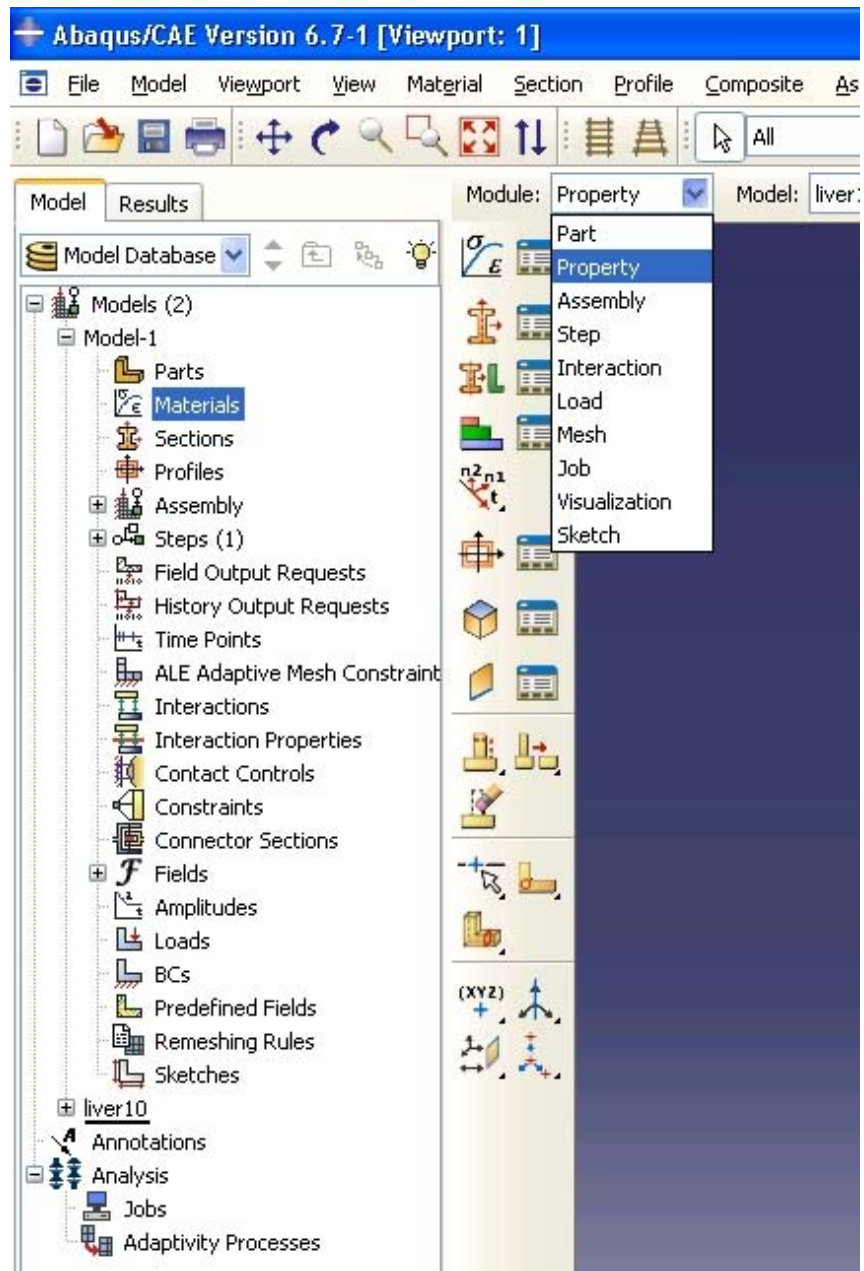
FIGURE 45 – Steps to perform finite element analysis in ABAQUS.

Property The second step is to set the material properties of the two parts. Select the Material module as listed in Figure 45. Then select the Material Manager under the Material menus to set the material properties. An interface window appears for one to set the properties under the four buttons General, Mechanical, Thermal, and Other. In this study, the liver density was set from the measurement. Actually, the density was measured by the weight and the volume. From the Mechanical menus, there are several models to be selected. The first two are the linear elastic and the hyperelastic. For the linear elastic model, the Young's modulus and the Poisson's ratio are needed to fill in. For the linear elastic model, the Young's elastic modulus $E = 1105kPa$ was obtained from the compression test as in Chapter V. The poisson's ratio of the liver tissue was around 0.4 which was used for the simulation. For the hyperelastic materials, there are several options to choose. For this study, the Neo Hooke item was selected. Also, there are several options to set the material properties. The Coefficients option was selected for the input source in this study. Then a window came up to ask the inputs $C10$ and $D1$ which were obtained in Chapter V. The indentor property can be set in Part section. When the indentor is designed or created using sketch, an option asked to set the part is an rigid or non-rigid three-dimensional body.

Assembly This step is to assemble the parts together. In this study, the indentor was moved to touch the liver mesh. Under the indentor, there were more than six surface triangles so that the the indentor had support in simulation.

Step The procedure is to set the static or dynamic types for simulation. In this study, the General, Static was selected.

Interaction This step is to set how the parts are interacted each other. In this study, it was to set how the indentor and the liver was interacted. Under the Interaction menus, selected the property to choose the Contact for simulation. The Edit Contact Property submenus was pressed and a window came up to select contact property. Tangential Behavior and frictionless were selected. Under the Mechanical menus, the tangential behavior was selected. Another interaction property was selected for the part indentor. The surface to surface contact was selected in Create Manager menus. Then the master and slave were

selected for the indentor and the liver tissue for interaction.

Loads This step is to impose the force load on parts. In this study, a force load was vertically imposed on the indentor at the top central (the reference point selected in the part design section) as the concentrated force.

BCs This step is to impose the restrictions and boundary conditions on the parts. A restriction was set on the reference point to allow the reference point moved only vertically. The boundary condition on the liver was to fix the bottom. No displacements of the nodes on the bottom surface was imposed by selecting the bottom nodes and setting their displacements in all three directions to zeros.

Job This step is to set the job name and to perform finite element analysis. Usually it took about 15 minutes to finish for this study each time. The ABAQUS interface panel would notice when the simulation is finished. Also, the simulation can be watched by selecting the monitor menus to see the simulation process.

Visualization This step is to see the results after simulation. In this module, choose the item under the menus Result to see the result as needed from the formed object file. There are many options and tools to make colors, superimposing, wire form, and drawing graphs of the relations of various variables such as stress to strain, energy change during process etc.

2. Supplemental results and discussions

In this subsection, the contours of the deformed objects were shown for both the LEM in Figure 46 and NHM in Figure 47. ABAQUS software has the functionality to show these. The stress contours were shown on the deformed liver with different colors based on their strengths. The Mises stress is a scalar function of the deviatoric components of the stress tensor that gives an appreciation of the overall magnitude of the shear components of the tensor. The superimposing of the deformed volume and the undeformed volume is illustrated for each force load (5g, 10g, 20g, or 40g). Figure 48 shows the superimposed of deformed volumes using LEM with the undeformed volume for the force loads 5g, 10g,
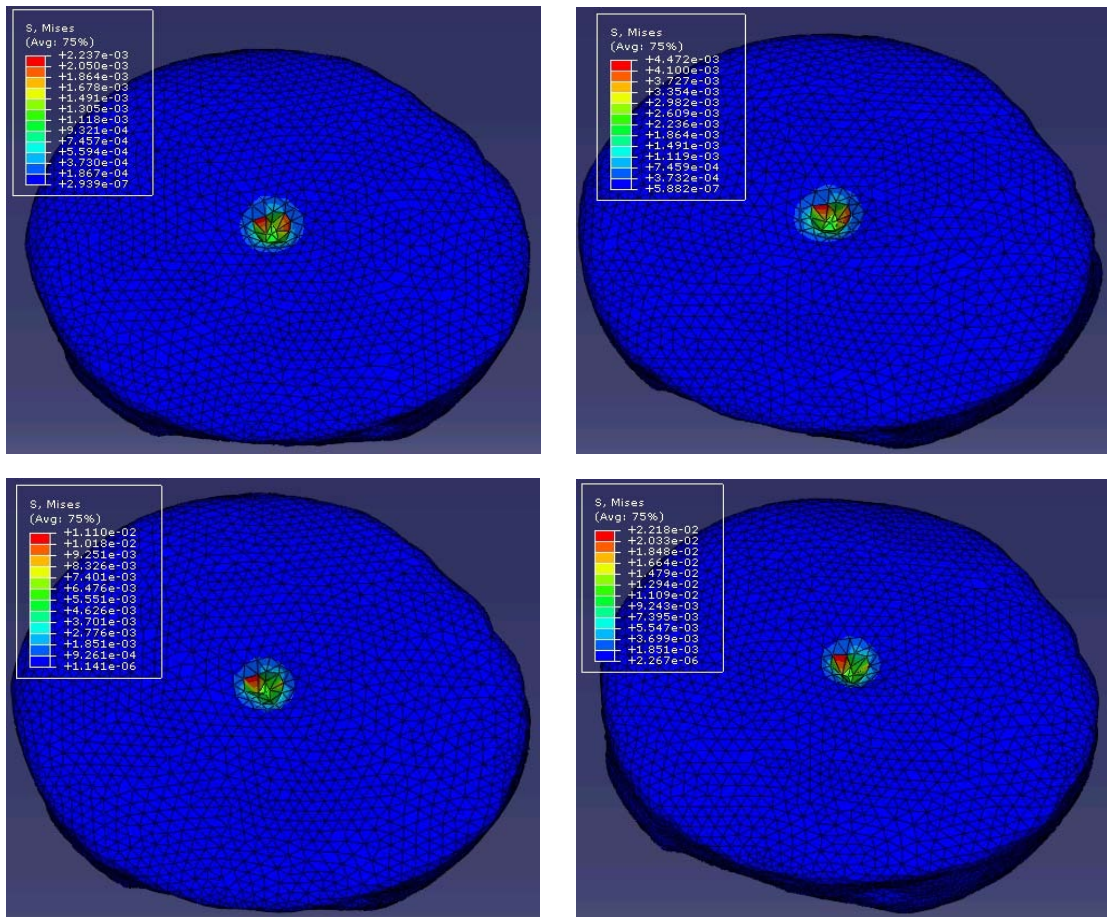
FIGURE 46 – The stress contours of the deformed livers using the LEM under the force loads 5g, 10g, 20g, and 40g from left to right and from the top to bottom.

20g and 40g from top to bottom and from left to right respectively. Figure 49 shows the superimposed of deformed volumes using NHM with the undeformed volume for the force loads 5g, 10g, 20g and 40g from left to right and top to bottom and from left to right respectively.

3. Stress vs. strain for key element nodes

For the LEM, the stress and strain keep proportional for all nodes. For the NHM, since it is nonlinear, the stress and strain are no longer kept proportional from time to time. Also the stress and strain also changing for different nodes. Two elements immediately under the indentor were selected to check the stress and strain relation for each nodes
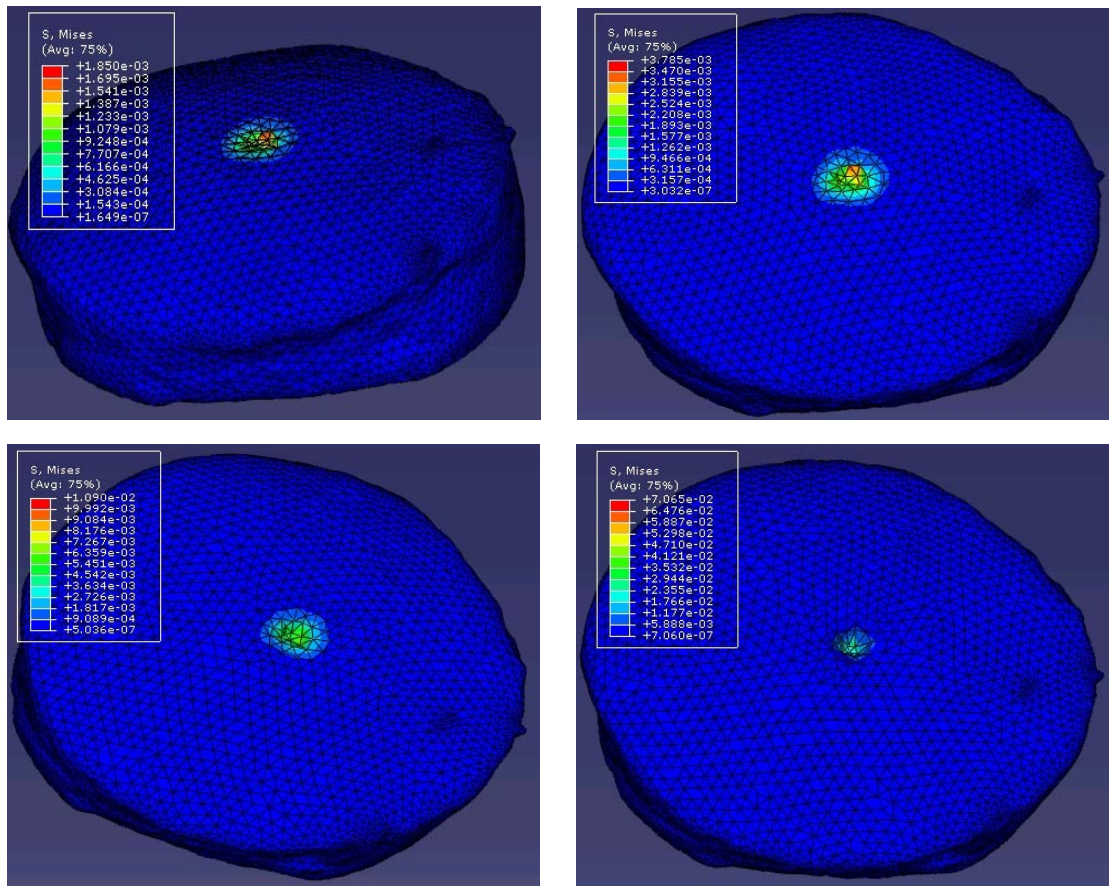
FIGURE 47 – The stress contours of the deformed livers using the NHM under the force loads 5g, 10g, 20g, and 40g from left to right and from the top to bottom.
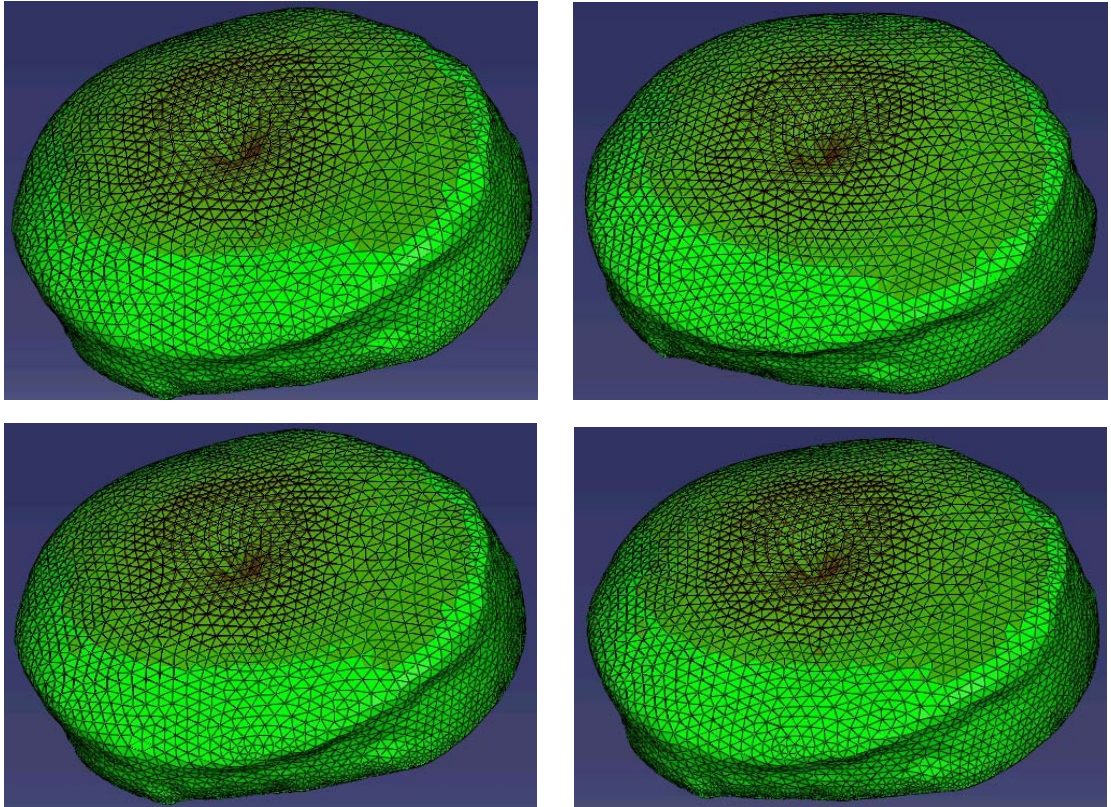
FIGURE 48 – Superimposing of the deformed livers using the LEM with the undeformed volume under the force loads 5g, 10g, 20g, and 40g from left to right and from the top to bottom.
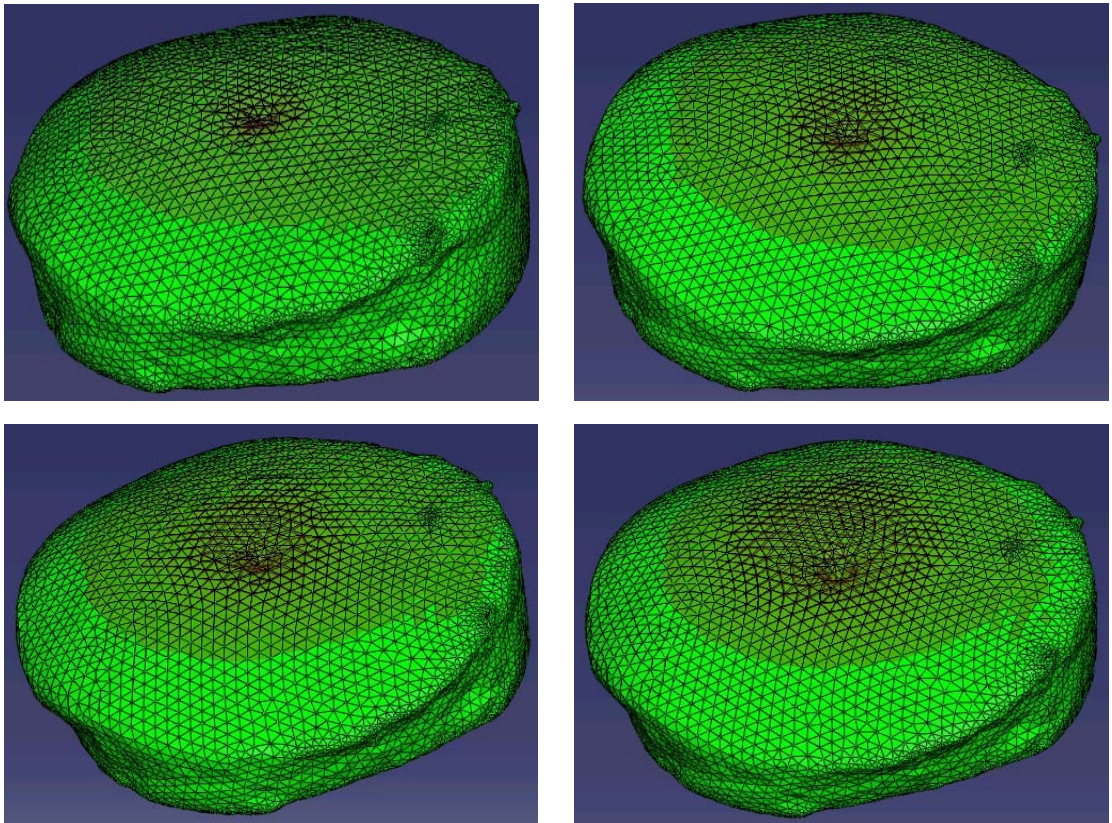
FIGURE 49 – Superimposing of the deformed livers using the NHM with the undeformed volume under the force loads 5g, 10g, 20g, and 40g from left to right and from the top to bottom.

for these two elements. The menus Tool is very useful to find the element numbers and node numbers. There is Query submenus under the menus Tool. From this submenus, the element numbers and their associated nodes. Figure refnodesElements illustrated this process.

Two of the elements immediately under the indentor were found. Their element numbers are 56706 and 49012. The associated nodes to the element 56706 are nodes 5126, 5136, 5313, and 6386. The associated nodes to the element 49012 are 5201, 5126, 5313, and 6386. It can be seen that the two elements have a common triangle with nodes 5126, 5313, and 6386. In the visualization module, the data sets of the strain with time, and the stress with time can be extracted by using the submenus XY-Plot under the menus Tool. Data sets were extracted from the generated output object (odb file). Each tetrahedron has four nodes. The stress and stain are changing from time to time for the neo-Hooke's hyperelastic model. The following figures illustrate the stress change with respect to the strain. ABAQUS combined the two data sets of stresses with time, and the strains with time into a new data set of the stresses with strains. The curve of the stresses with respect to the strain is displayed for each node of the two elements. The stress-strain curves for the force loads of 5 grams, 10 grams, 20 grams, and 40 grams are listed for all nodes of the two selected elements to show the curve changes for different force loads and the changes of the stresses and strains for different nodes. Figures 51, 52, 53, and 54 illustrated the stress vs. strain curves for all the nodes of the element 56706 which was immediately under the indentor. Figure 55 shows the stress vs. strain curve for the node 5201 of the element 49012 which shares a common triangle in its tetrahedron element formation. The other three nodes of the element 49012 are the nodes 5126, 5313, and 6386 of the element 56706.

From the deformed object shape, for the indentor with the flat tip, the deformed area with the indentor was not flat. This is due to the use of the tetrahedron element shape. There were less than twelve element under the indentor and the sizes of the elements were different, and the stress vs. strain curves for different nodes were quite different. These may be two of the reasons that that the deformed area with the indentor from simulation
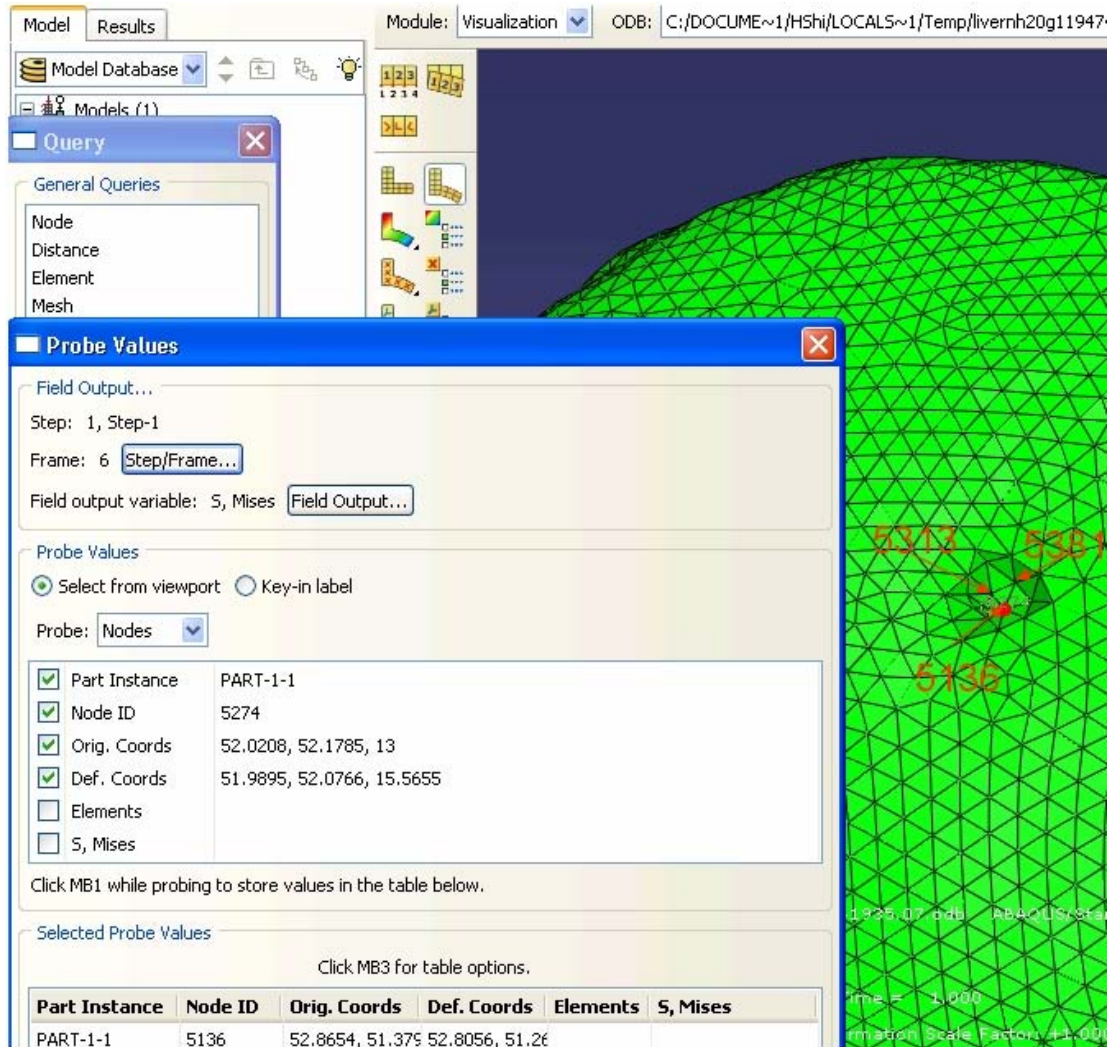
FIGURE 50 – Find the element numbers and their associated using ABAQUS.
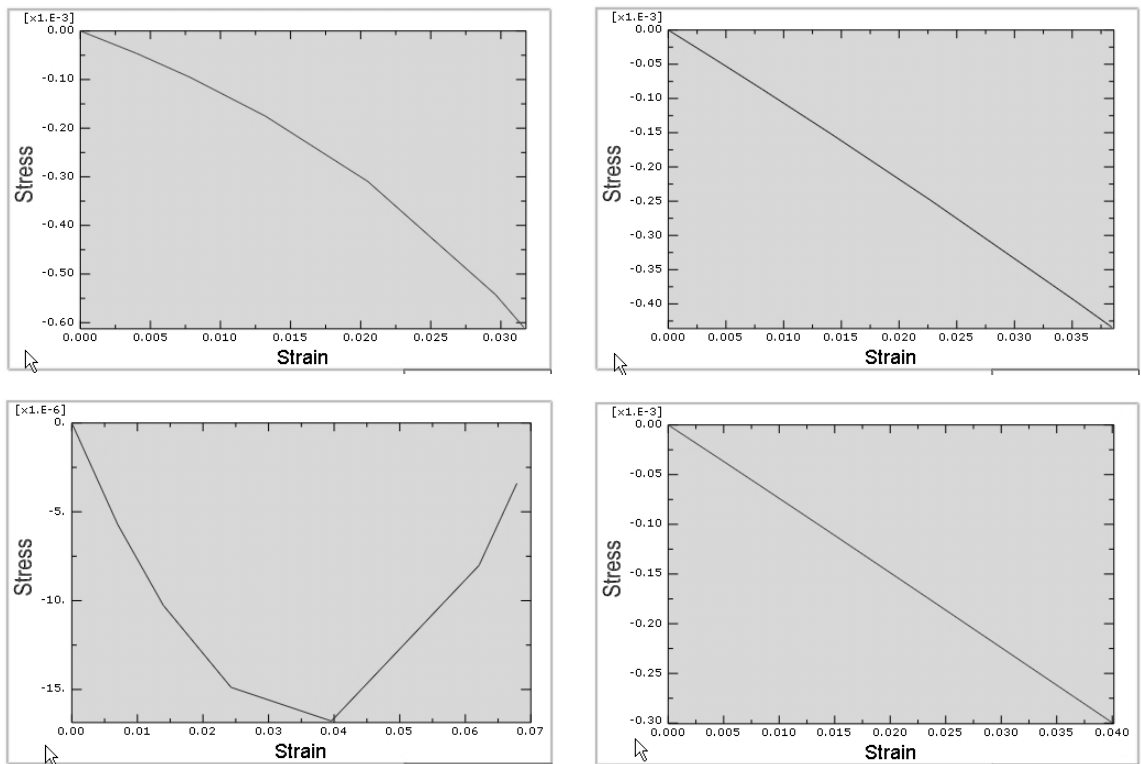
FIGURE 51 – The stress vs. strain curves for all the nodes of the element 56076 under the force load of 5 grams, the node numbers for the four nodes are 5126, 5136, 5313, and 6383 from left to right and top to bottom respectively.
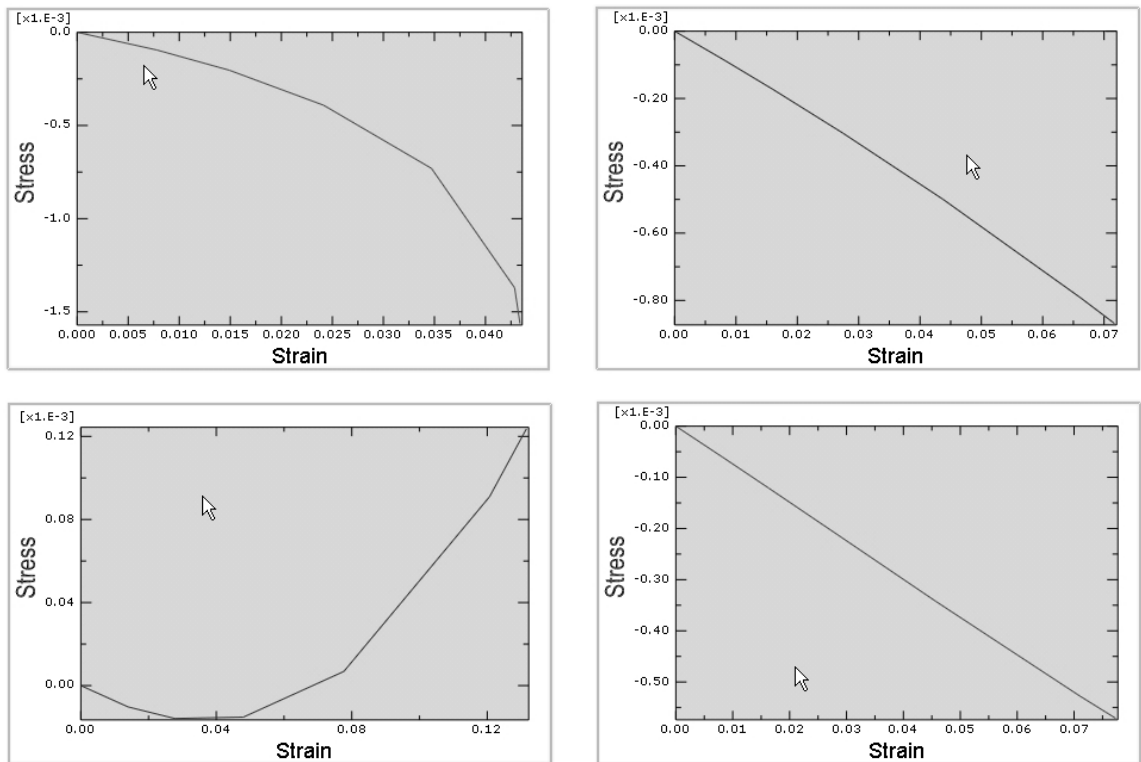
FIGURE 52 – The stress vs. strain curves for all the nodes of the element 56076 under the force load of 10 grams, the node numbers for the four nodes are 5126, 5136, 5313, and 6383 from left to right and top to bottom respectively.
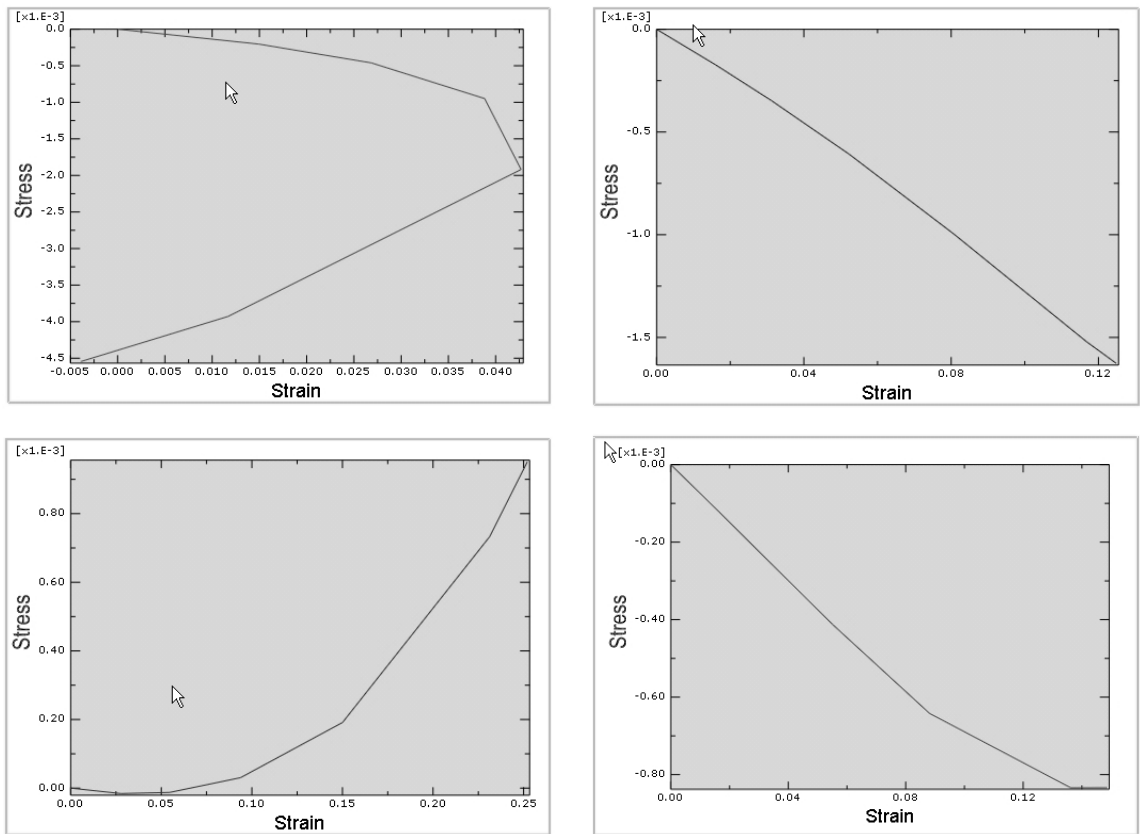
FIGURE 53 – The stress vs. strain curves for all the nodes of the element 56076 under the force load of 20 grams, the node numbers for the four nodes are 5126, 5136, 5313, and 6383 from left to right and top to bottom respectively.
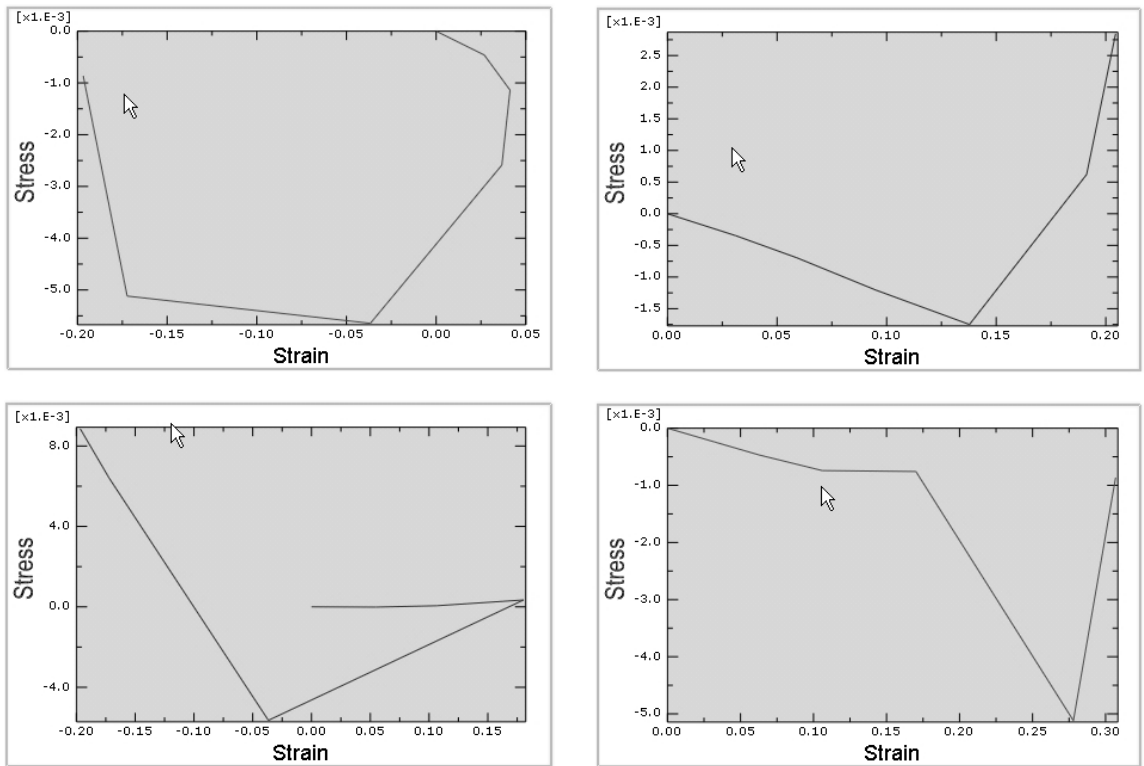
FIGURE 54 – The stress vs. strain curves for all the nodes of the element 56076 under the force load of 40 grams, the node numbers for the four nodes are 5126, 5136, 5313, and 6383 from left to right and top to bottom respectively.
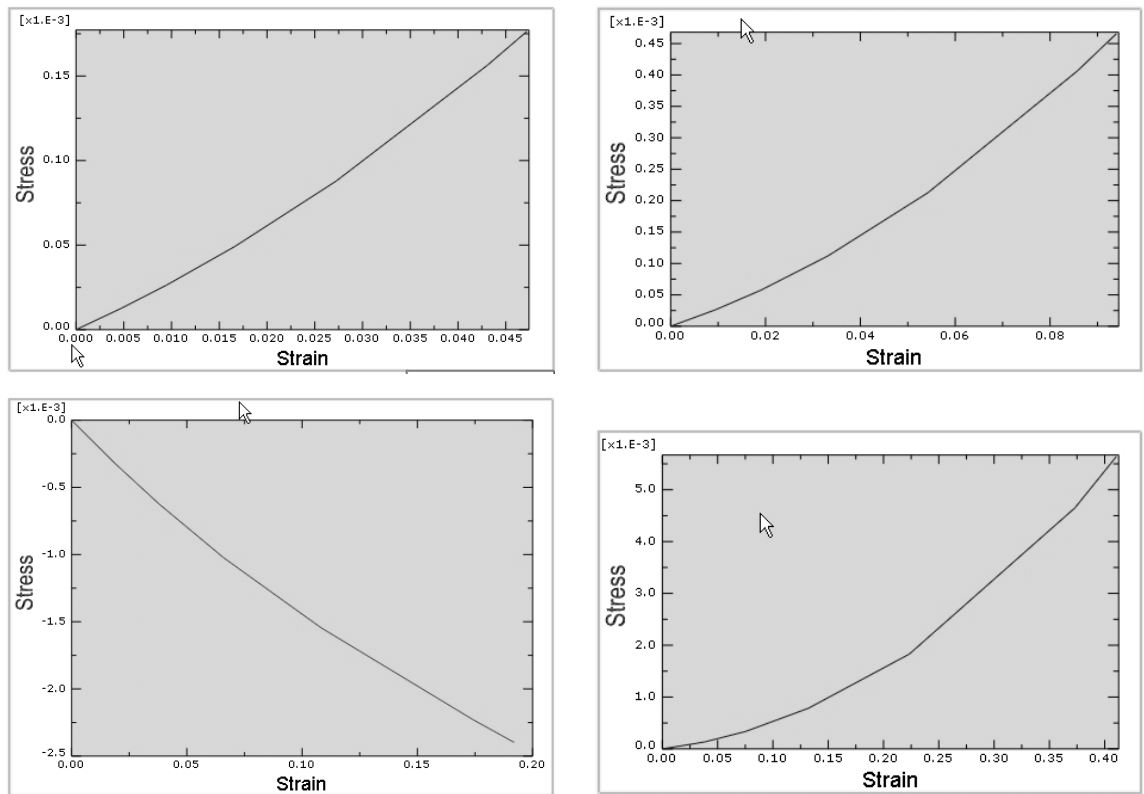
FIGURE 55 – The stress vs. strain curves for the node 5201 of the element 49012 under the force load of 5, 10, 20, and 40 grams from left to right and top to bottom respectively.

was not flat. The results shown in Chapter VI also had this phenomenon. The indentor used there also had the flat tip.

E.   SUMMARY

This chapter addressed the details of the stereolithographical file generation using VTK-TCL language. The volume mesh generation using NETGEN was expounded in detail. The mesh density control was discussed. The contact of the indentor with the volume mesh surface in this study was explained for finite element analysis. The stress and strain were charted for some key element nodes from the finite element analysis using the neo-Hooke's hyperelastic model. All the sections in this chapter constitute the whole procedure for the finite element modeling of soft tissues except the different segmentation methods and biomechanical models.

CHAPTER VIII
MATERIAL PARAMETERS ESTIMATION OF LIVER TISSUE

A.   INTRODUCTION

Accurate prediction of tissue deformation depends on the accuracy of tissue material parameter values [12]. The simple biomechanical model for small force loads is the linear elastic model (LEM) which has been used widely in applications such as the modeling of the force driven left ventricular deformation ([27]), the modeling of ultrasonic waves ([95]), and registration of intraoperative MR images of the brain ([30, 40]). It is important to use accurate material parameters. The works such as [11, 15, 96–98] focused on material parameter measurement from actual deformation of a prescribed shape tissue under a force load in a single process. The errors may arise due to the limitations of measurement devices.

Kauer *et. al.* in [99] determined the optimal material parameters of synthetic material by an objective function which consists of the square differences between simulated and experimental data globally using a nonlinear viscoelastic model. Soza *et. al.* in [46] used the normalized mutual information ([100]) as a criterion to determine the Young's modulus and the Poisson's ratio in the linear elastic model of brain tissue. The criterion related the gray value distributions between the image reconstructed from simulation and the intraoperative brain data. Both methods were applied in the material parameter estimation. However, their image resolutions were quite low and may affect the accuracy of the material parameter determination. Also, in this case, an actual indentor was used to push the liver and gradually capture high resolution images of the deformed liver as in practice.

This chapter aims to use high resolution images to estimate the material parameters of the liver tissue under small force loads through comparison of the results using various

material parameters in the linear elastic model. From these deformation results, The suitable values of the material parameters can be determined and the influence of the tissue dehydration and the limitations of the measurement devices can be found. The criterion to find suitable material parameters using the linear elastic model for very small force loads is the minimization of the absolute difference of the maximum deformation depth from simulation and the one from real experiment. Micro-CT can capture images of high resolution of $0.1 \times 0.1 \times 0.1 mm^3$. As a benefit, the shape of tissue surface in the contact region between the tissue and the indentor can be captured under small force loads ranging from several grams to tens of grams. For comparison, the tissue's material parameters are also acquired using a DMA.

B.   DEFORMATIONS USING VARIOUS MATERIAL PARAMETERS

In the linear elastic model, the Young's modulus for liver tissue is around 10 kPa ([37]) and the Poisson's ratio is around 0.4 ([11, 15]). However, for the *ex vivo* liver tissue, due to the dehydration, the Young's modulus and the Poisson's ratio may change around these values. In this section, the liver deformations in experiments are estimated and then finite element analysis of the liver deformations is performed using the Young's moduli from 5 kPa to 14kPa and the Poisson's ratios from 0.35 to 0.44. Then, suitable Young's modulus and Poisson's ratio can be found for the linear elastic model to predict the deformation close to the real deformation from experiments.

For a fixed force load, the tissue displacement from the real experiment is unique. The maximum tissue displacement can be found automatically from the scanned Micro-CT images of the deformed liver and the undeformed liver. To compute the deformation volume difference between the deformed object from simulation and the one from experiment, considering the smallness of the deformation range, a cylinder with radius of 25 mm and height of 50 mm is used to cover the deformed region. The cylinder is positioned vertically and centered at the indentor contact. The deformed volume is computed by the total number of voxels between the deformed surface and the bottom surface of the cylin-

TABLE 4

MAXIMUM DISPLACEMENTS AND VOLUME CHANGES IN REAL
EXPERIMENTS FOR DIFFERENT FORCE LOADS

	5g	10g	20g	40g	60g
Displacement (mm)	2.5	4.0	5.2	8.1	9.7
Volume change (mm^3)	135.88	250.46	425.86	581.91	780.72

der. Table 4 lists the maximum displacements of the liver tissue, and the volume changes from the undeformed liver to the deformed liver for five different force loads. Figure 56 shows the curves of maximum displacements and volume changes. From these curves, it is seen that the liver deformation is approximately linear for the force loads less than 10 grams but it looks parabolic as the force load increases, and the linear elastic theory may be applied to modeling of the liver deformation for small force loads. However, as the force load increases, the deformation deviates from the linearity gradually. Figure 57 shows the superimposing of the deformed liver from simulation and the deformed liver from experiments under the force loads of 5 grams (a), 10 grams (b), 20 grams (c), and 40 grams (d), respectively.

C.   RESULTS AND DISCUSSIONS

Finite element analysis was performed repeatedly for various material parameters under different small force loads using high resolution Micro-CT images. With the force load changing, the better material parameters to match the real displacement varied slightly for the linear elastic modeling. There are several reasons for this phenomenon. The first one is the assumption of the linear and isotropic properties of the liver tissue. The second reason is the dehydration of the *ex vivo* liver cut from the lamb. Another reason is the geometric nonlinearity of the liver structure and the indentor with the half spherical tip.

For the force load of 5 grams, the maximum displacement from simulation close to the maximum displacement from experiment is at the Young's modulus of 7 kPa and the
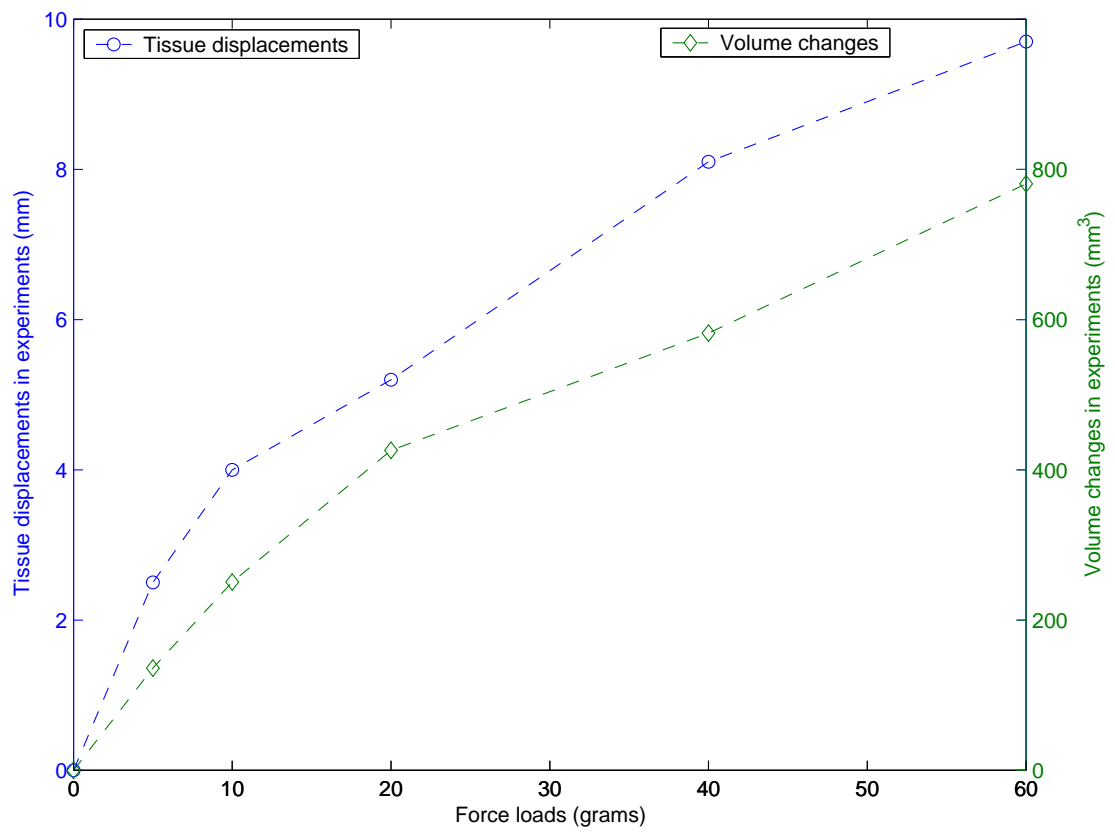
FIGURE 56 – The curves of maximum displacements and volume changes under different force loads.
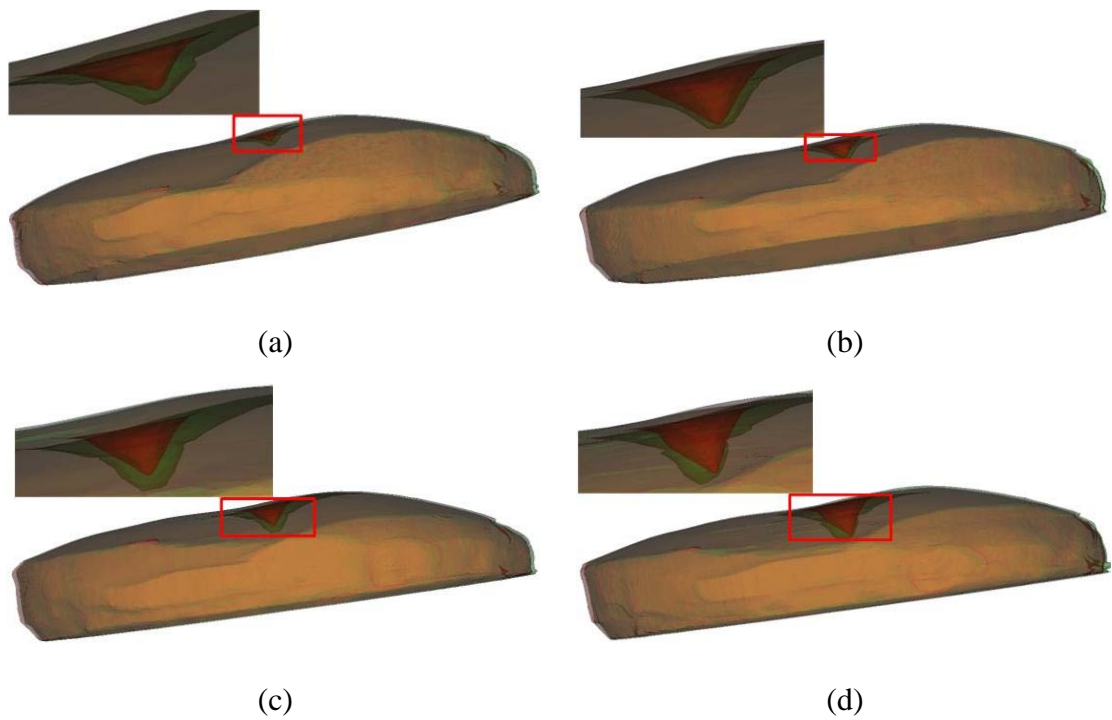
FIGURE 57 – Superimposing of the deformed livers from simulation (red) and experiment (green) under the force loads of 5, 10, 20 and 40 grams respectively (a, b, c, and d). The pairs of Young's modulus and Poisson's ratio for 5, 10, 20, and 40 grams are (7 kPa, 0.4), (7 kPa, 0.39), (12 kPa, 0.4) and (14 kPa, 0.43) respectively.

Poisson's ratio of 0.4. For the force load of 10 grams, the maximum displacement from simulation close to the maximum displacement from experiment is at the Young's modulus of 7 kPa and the Poisson's ratio of 0.39. For the force load of 20 grams, the maximum displacement from simulation close to the maximum displacement from experiment is at the Young's modulus of 12 kPa and the Poisson's ratio of 0.4. For the force load of 40 grams, the maximum displacement from simulation close to the maximum displacement from experiment is at the Young's modulus of 14 kPa and the Poisson's ratio of 0.43. Fig. 58 shows that for various material parameters, the tissue displacements change larger with the Young's modulus increasing than those with variance of the Poisson's ratios.

From the simulation results above, it was found that the material parameters obtained under the force load of 20 grams is quite matched with those in [11, 15]. The Young's modulus of 1200 kPa is also matched with that of 1105 kPa from the measurement using the DMA machine. For the force loads of 5 and 10 grams, the Young's modulus should be close to 10 kPa. But, due to the geometric nonlinearity of the liver and the imperfect initial contact under the low load, the resistance to the moving of the indentor makes the tissue displacement less than that predicted. The material parameters were determined by minimizing the absolute differences between the displacements from real experiment and the ones from simulation. The material parameter measurements were also performed using the DMA for comparison with those obtained from simulation. A piece of lamb liver with dimensions of $12.7 \times 50.8 \times 3.81 \ mm^3$ was used for measurement. From the compression test, a global stress-strain curve was obtained. The portion of the stress-strain curve for the strain less than 10% was used to compute the Young's modulus yielding $E = 11055 \ Pa$ which is comparable with that obtained under the force load of 20 grams.

D.   SUMMARY

The high resolution Micro-CT images were employed to show the liver tissue deformations for different material parameters using the linear elastic model. The optimal material parameters are determined by minimizing the absolute differences between the
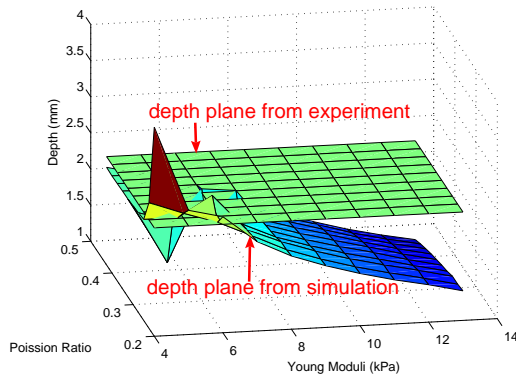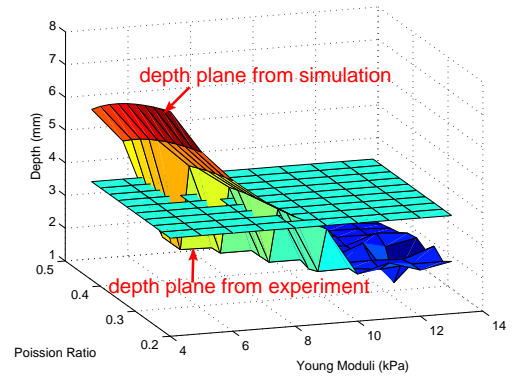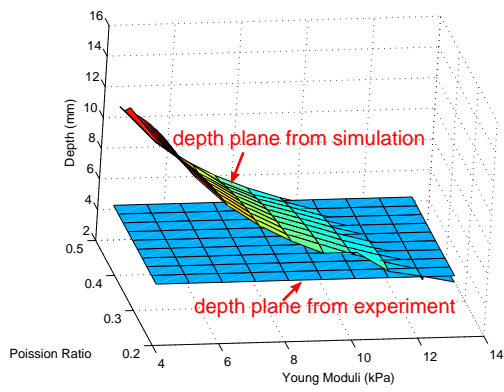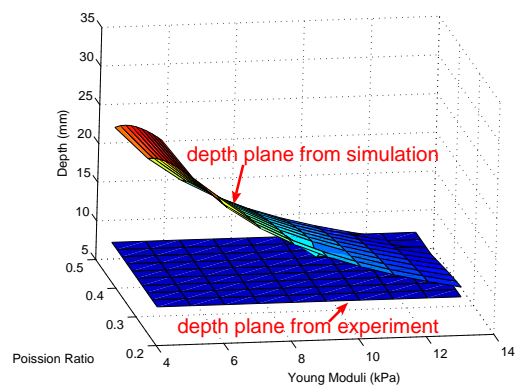
FIGURE 58 – Displacements from simulation and experiment under the force loads of 5 grams (a), 10 grams (b), 20 grams (c), and 40 grams (d) respectively.

displacements from real experiment and the displacements from simulation. For the force load of 20 grams, the determined Young's modulus and Poisson's ratio are quite consistent to those in literature and the measurements using DMA machine. It was also found that for small force loads of 5 and 10 grams, the determined material parameters are not matched well with those from literature and the measured ones using DMA machine. For the larger force load of 40 grams, the material parameters determined from simulation deviated from the measured ones. There is a future plan to investigate more complicated biomechanical models using Micro-CT images.

CHAPTER IX
REGION-OF-INTEREST FINITE ELEMENT MODELING

A. INTRODUCTION

In recent years, image guided minimally invasive surgical simulation has attracted researchers and surgeons. In laparoscopic surgery, only a small hole is opened and the endoscopic instrument is inserted to minimize the damage of the surrounding healthy tissue caused by surgery on internal organs, such as liver and spleen, [101, 102]. The instrument can be a camera, probe, or scissor. One main challenging problem is to determine the region of interest (ROI) for diagnosis and surgical treatment so that the surgical tool can be applied over a well specified region of the internal organ. On the other hand, the traditional finite element analysis over large or entire organ is quite computationally expensive, and may not be suitable for real-time analysis of the deformation induced during surgery, which may lead to errors in localization of the tumors. To reduce the simulation time or realize real-time performance, the finite element method which produces local mesh-based models has been employed for different types of surgical simulations [51, 103–105]. In reality, the affected area in the surgery is only a small region instead of the large or entire organ while the affection of the rest region is very small or can be ignored in real practice. So, as expected, finite element modelling over the ROI in real-time is promising in laparscopic surgery if the ROI is well determined.

In Chapter VI, the linear elastic model and the neo-Hooke's hyperelastic model were employed to simulate the liver tissue responses to small force loads in the strain range less than 10%. For the probe with spherical tip, it was shown that the linear elastic model performs better than the other two for the force loads less than or equal to 20 grams, while

the neo-Hooke's hyperelastic model performed better than the linear elastic model for the force load larger than 20 grams. So, the neo-Hooke's hyperelastic model is chosen for the finite element analysis over regions of interest. This chapter, the neo-Hooke's hyperelastic model is used to test the liver deformation over different concentric regions of interest centered at the tip of surgical probe for very small force loads. An indentor with half spherical tip is employed in this study. The tissue deformations over different ROIs centered at the tip of the surgical tool are investigated. They are compared with those from finite element modelling over the whole piece of liver, and further, the results are verified using those from real experiments.

B. LIVER DEFORMATIONS OVER CONCENTRIC REGIONS

1. Experiments and Simulations

In the process of mesh generation, the coordinate system has been set up. The position of the probe tip can be identified from the acquired deformed images easily. In this study, the tip position is around the center of the liver tissue and the center of the 2D image. The tip coordinates are $(50.0512, 49.21)$ in the entire slice with dimension of 102.4 mm $\times$ 102.4 mm. The gaps between two neighboring concentric regions are all equal to 3.2 mm for the purpose of finite element analysis over different regions. Figure 59 shows the tip position and concentric regions. The maximum deformed depths over these regions are recorded and compared with the ones from finite element analysis over the whole liver domain. The applied force loads are 5, 10, 20, 40, and 60 grams at different times. There are two boundary conditions in finite element analysis. One is that the reference point on the probe has only vertical freedom in z-axis direction to go up or down. The other boundary condition is the fixation of the liver bottom. Since the friction between the liver and the chamber bottom (glass) is relatively larger compared to the force loads applied, it is reasonable to assume the bottom of the liver is fixed. It is also observed from conducted real experiments that the bottom of the liver has almost no movement.
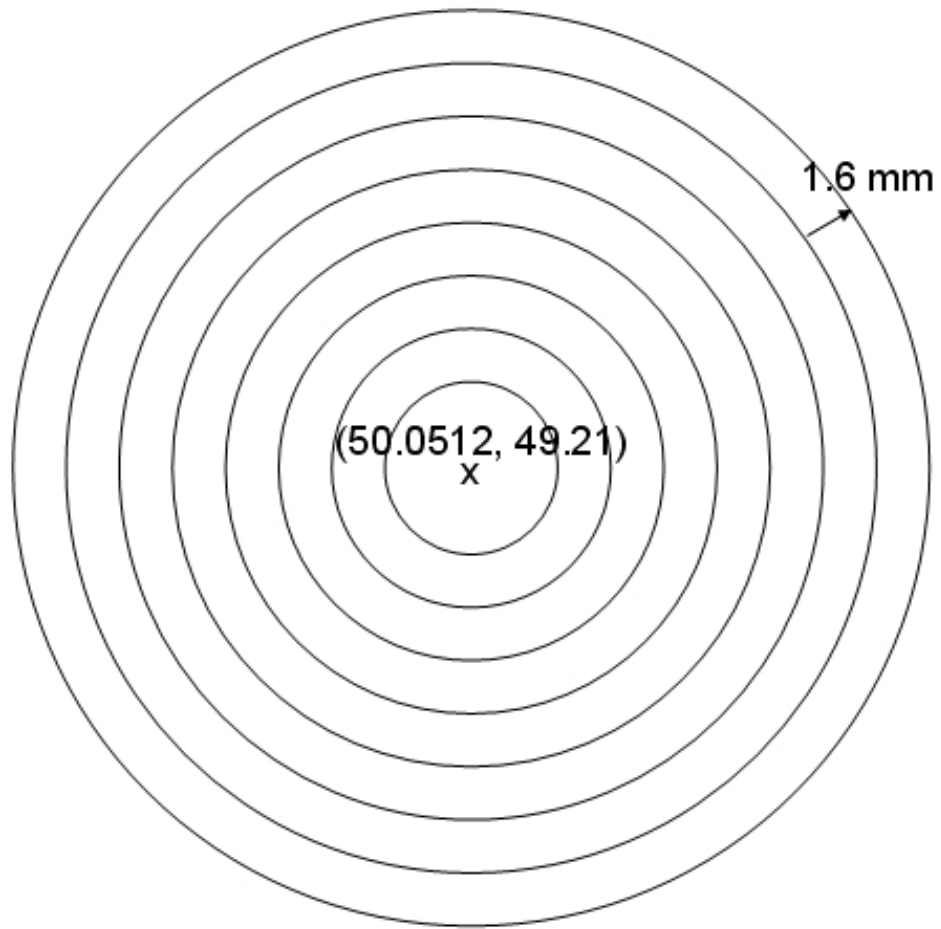
FIGURE 59 – The concentric regions centered at the probe tip with equal spacing gap, and z-axis pointing out from the plane.

Again, the ABAQUS finite element software was used for these simulations. The force loads in simulation are 5, 10, 20, 40, and 60 grams. For the force loads of 40 and 60 grams, the simulation results showed that the solutions were not converging and the past simulations failed for many attempts to search for equilibrium establishment. One reason could be due to the geometric nonlinearity in simulations. Another reason might be the non-applicability of the neo-Hooke's hyperelastic model to liver tissue response under larger force loads for the probe with half spherical tip.

2. Quantitative Analysis

For quantitative comparison, three tasks of computation are performed as follows.

- Computing the maximum liver displacements on the z-axis direction over concentric regions from finite element analysis over the entire liver.

- Computing the maximum liver displacements on the boundaries of different concentric circles, and the maximum liver displacements outside these concentric regions from finite element analysis over the entire liver.

- Computing the maximum liver displacement on the boundary of each concentric region of interest where finite element analysis is performed separately over the concentric region.

The goal of all is to compute the probe displacement in the z-axis direction. For all three tasks, the boundary conditions are the fixation of the bottom, and the the reference point on the probe has only vertical freedom in z-axis direction to go up or down. Since the position change is mainly on the z-axis direction as the force is applied vertically, the displacement is mainly the change on the z-axis direction. The results shows that the displacements on the x-axis and y-axis direction are less than 10% of the displacement on the z-axis direction.

Table 5 lists the maximum liver displacements from finite analysis over different concentric regions of interest centered at the tip $(50.0512, 49.21)$ of the probe and the max-

imum displacement from experiment on the test piece of liver. The displacements from simulations are only for successful simulations under the force loads of 5, 10, and 20 grams. The "Radii" denotes the radii of the regions of interest. The "Whole" denotes the whole tested liver on which finite analysis is performed, and "E-Whole" also denotes the whole tested liver but the results are from experiments. Compared with those results in Chapter 5 and [89] where the probe has the flat tip, the maximum displacement of the liver tissue is larger for each same force load.

It is noted that the maximum displacements for the ROI with radii of 13.2mm, and 19.6mm respectively are less than those of their neighboring ROIs for all force loads of 5, 10 and 20 grams. This behavior appears at the two neighboring regions of interest with radii of 26.0mm and 29.2mm, which means that these lower maximum displacements has larger cycle than the previous one. The deformed surface behaves like a sinusoidal wave extension after the force load applied. The finite element analysis is performed in a complete similar manner and same condition except the the difference of concentric circle domains with different radii. A reasonable thought is that when a stone is drop into water, the water propagated in decayed sinusoidal wave outwards. Since the fresh liver is quite soft and contains much water in its composites. However, this phenomenon has no theoretic proof and integrated view.

Table 6 lists the maximum liver displacements on the boundaries of the concentric regions of interest. In consideration of the positions of nodes on the boundaries, the maximum displacements on the boundaries are computed by computing the maximum displacements of nodes in the actual region extending 2mm inwards from the boundaries (circles). It is seen that the maximum displacements on the boundaries are quite small (less than 10%) compared to the maximum displacements for larger regions (radius larger than 19.6mm).

Table 7 lists the maximum liver displacements over the same regions as in Table 6 from finite element analysis over the whole liver domain. It can be seen that the maximum displacements on the specified regions from finite element analysis over the whole domain are comparably smaller than those from finite element analysis over the concentric regions

TABLE 5
MAXIMUM DISPLACEMENTS FROM FINITE ELEMENT ANALYSIS ON
DIFFERENT CONCENTRIC REGIONS OF INTEREST, THE WHOLE LIVER, AND
THE MAXIMUM DISPLACEMENT FROM REAL EXPERIMENTS (ALL THE DATA
ARE WITH UNITS OF MILLIMETERS).

Radii	5g	10g	20g
10mm	1.1664	1.8537	1.9066
13.2mm	0.8399	1.5746	1.5746
16.4mm	1.0153	1.9430	2.0689
19.6mm	0.9401	1.1508	1.1510
22.8mm	1.0228	2.0230	2.8405
26.0mm	0.8202	1.5746	1.6268
29.2mm	1.0123	1.5734	1.5758
32.4mm	0.8893	1.7163	2.4206
Whole	1.0042	1.8847	3.2772
E-Whole	2.2	2.6	4.8

TABLE 6
MAXIMUM DISPLACEMENTS ON THE BOUNDARIES OF CONCENTRIC
REGIONS OF INTEREST FROM SEPARATE FINITE ELEMENT ANALYSIS OVER
THESE CONCENTRIC REGIONS.

Radii	5g	10g	20g
10.0mm	0.3899	0.5684	0.7148
13.2mm	0.0938	0.2094	0.2100
16.4mm	0.0765	0.1328	0.1403
19.6mm	0.0515	0.0758	0.0771
22.8mm	0.0238	0.0573	0.0739
26.0mm	0.0064	0.0167	0.0203
29.2mm	0.0109	0.0289	0.0296
32.4mm	0.0087	0.0219	0.0426

TABLE 7
MAXIMUM DISPLACEMENTS ON THE BOUNDARIES OF CONCENTRIC
REGIONS OF INTEREST FROM FINITE ELEMENT ANALYSIS OVER THE
WHOLE LIVER DOMAIN.

Radii	5g	10g	20g
10.0mm	0.0668	0.1251	0.2233
13.2mm	0.0297	0.0543	0.0990
16.4mm	0.0110	0.0198	0.0328
19.6mm	0.0030	0.0048	0.0099
22.8mm	0.0032	0.0066	0.0116
26.0mm	0.0033	0.0067	0.0105
29.2mm	0.0028	0.0055	0.0083
32.4mm	0.0018	0.0036	0.0056

TABLE 8
MAXIMUM DISPLACEMENTS OUTSIDE THE CONCENTRIC REGIONS OF
INTEREST FROM FINITE ELEMENT ANALYSIS OVER THE WHOLE LIVER
DOMAIN.

Radii	5g	10g	20g
10.0mm	0.0668	0.1251	0.2233
13.2mm	0.0297	0.0543	0.0990
16.4mm	0.0110	0.0198	0.0328
19.6mm	0.0071	0.0138	0.0191
22.8mm	0.0071	0.0138	0.0191
26.0mm	0.0071	0.0138	0.0191
29.2mm	0.0071	0.0138	0.0191
32.4mm	0.0071	0.0138	0.0191

of interest. So, region of interest based finite element modelling of liver tissue must sacrifice some loss in the estimation of the liver deformation and reconstruction. However, the loss is quite small for small force loads. As the force load increases, on a same region the difference of the deformation from finite element analysis over a concentric region of interest and the deformation from finite element analysis over the whole domain is increased. Such a difference may be partially caused by the specific sharp anatomic structures of the liver which may move relatively large due to even a very small load. However, it is largely caused by the reduction of surrounding tissue enclosing the concentric regions of interest. The surrounding tissue provides support to the central regions. It is difficult to describe such support in boundary conditions for finite element analysis. In this finite element analysis, it is assumed that the side surface of the liver can freely move and rotate.

In the following, if the unit is not indicated, the unit is millimeters. Table 8 lists the maximum liver displacements outside the concentric regions of interest from finite element analysis over the whole liver domain. The special sharp anatomical structures may cause some relatively large displacement. This can be seen from comparison of Table 7 and Table 8. In Table 8, the maximum liver displacements are the same outside concentric regions of interest with radii equal or larger than 19.6mm. For better visualization, Figure 60, Figure 61, Figure 62, and Figure 63 shows the curves corresponding to Table 5, Table 6, Table 7 and Table 8, respectively.

From the quantities listed in the four tables, it can be seen that the finite element analysis over the concentric regions of interest may generate different results. With the expansion of the concentric region, the liver tissue deformation from the finite element analysis over the concentric region approaches the liver tissue deformation from finite element analysis over the whole liver domain.

3.   Visualization

For visual comparison, the deformed liver tissue from the finite element analysis over each concentric ROI is superimposed with that from finite element analysis over the
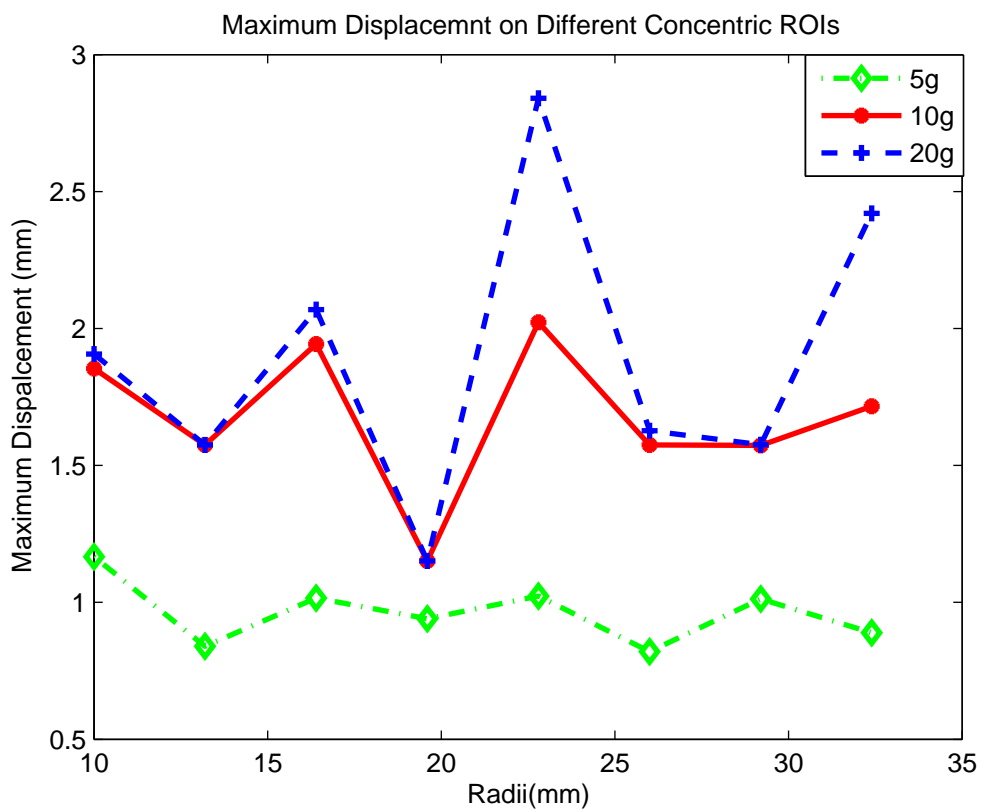
FIGURE 60 – Maximum displacements from finite element analysis on different concentric regions of interest, corresponding to Table 5.
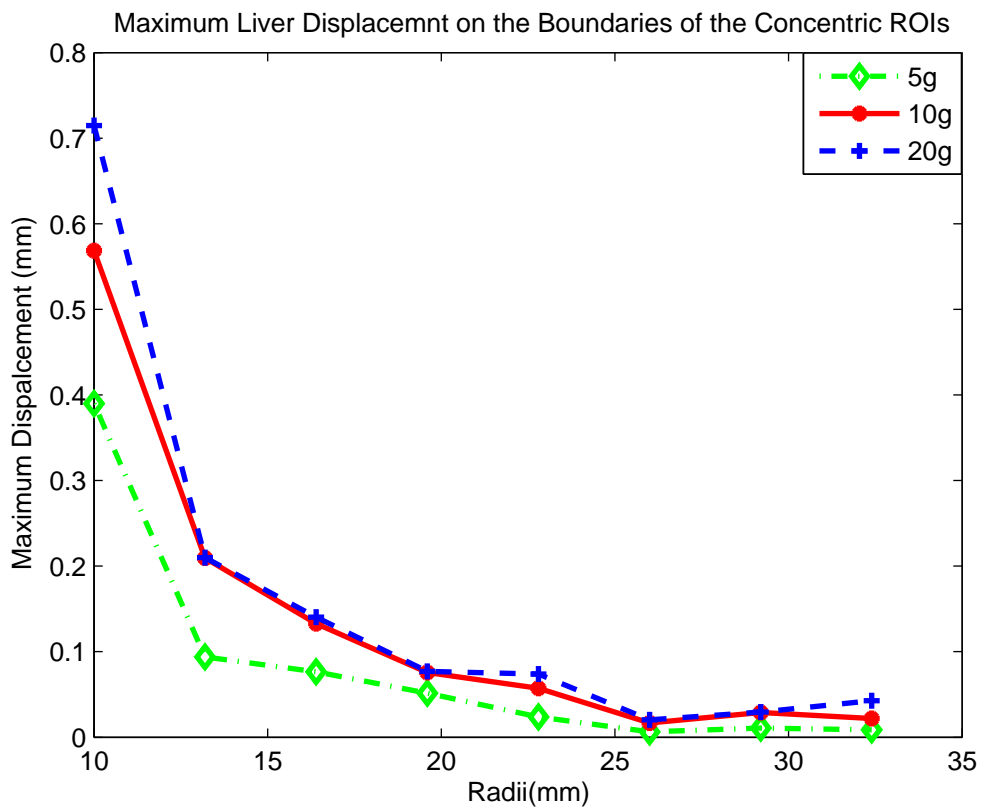
FIGURE 61 – Maximum displacements on the boundaries of concentric regions of interest from separate finite element analysis over these concentric regions, corresponding to Table 6.
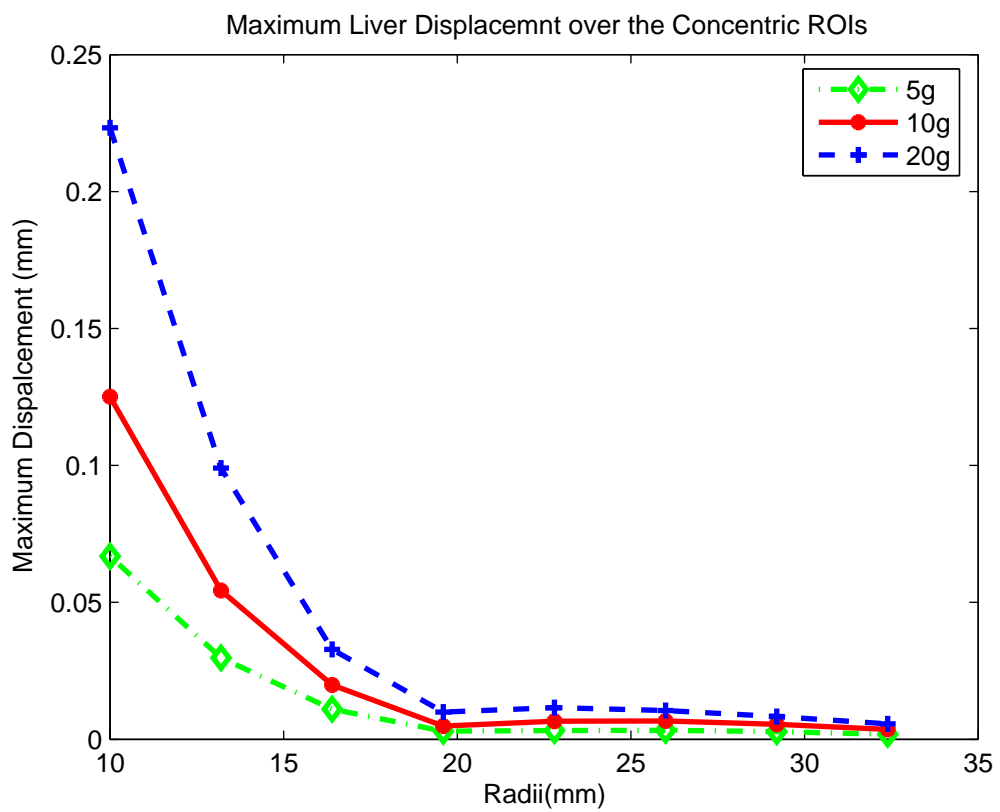
FIGURE 62 – Maximum displacements on the boundaries of concentric regions of interest from finite element analysis over the whole liver domain, corresponding to Table 7.
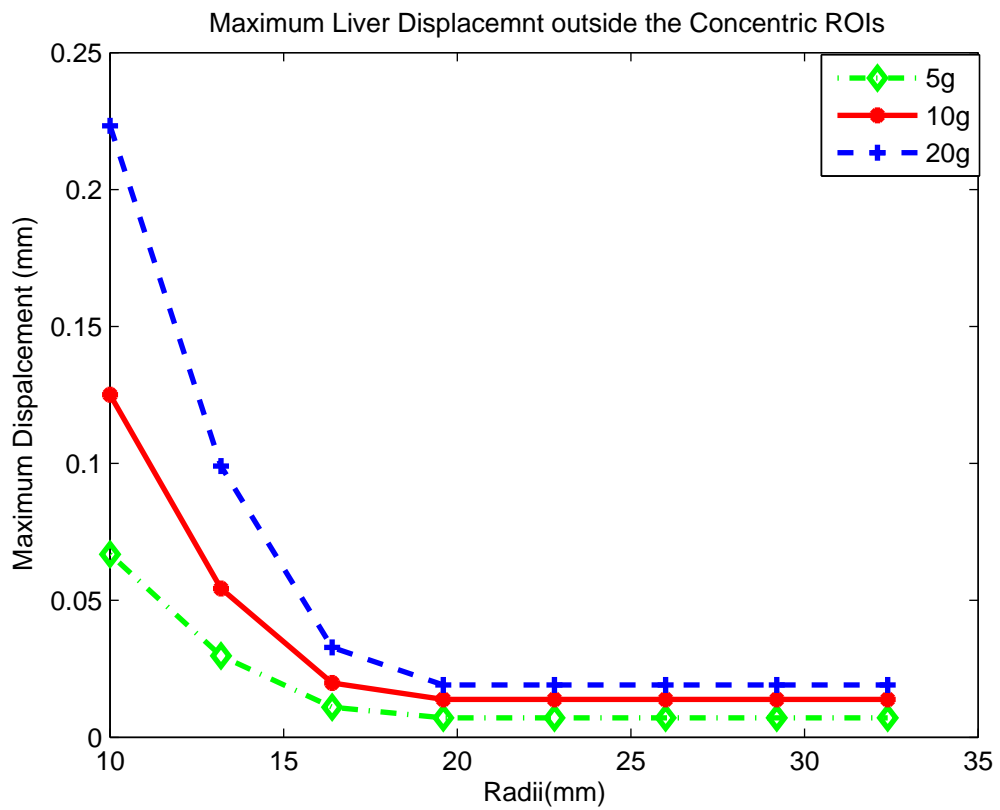
FIGURE 63 – Maximum displacements outside the concentric regions of interest from finite element analysis over the whole liver domain, corresponding to Table 8.
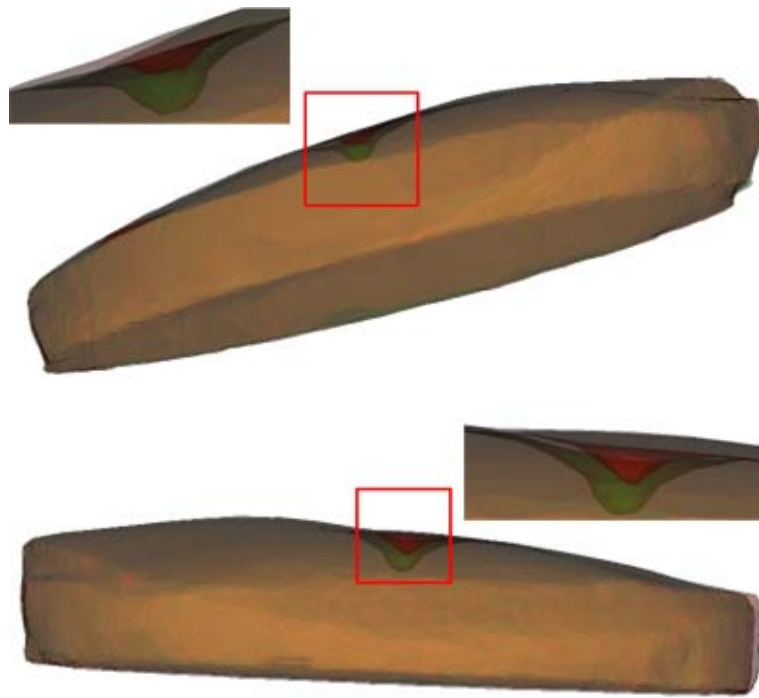
FIGURE 64 – The superimposing of the deformed liver tissue from finite element analysis over the whole domain with those from experiments for the force loads of 10 grams (top) and 20 grams (bottom) respectively.

whole piece of liver, and also the deformed liver tissue from the finite element analysis over the whole liver is superimposed with that from real experiments. Figure 64 shows the superimposing of the deformed liver from simulation and the deformed liver from experiments in the whole liver domain for the force load of 10 and 20 grams. These views are consistent with the results listed in Tables 5, 6, 7, and 8. Figure 64 shows the superimposing of the deformed liver tissue from finite element analysis over the whole domain with those from experiments.

C. SUMMARY

This chapter proposed to investigate region of interest finite element modelling of liver tissue. The results show such modelling may generate different deformations from those using the finite element analysis over the whole liver domain. Although the maximum liver displacement on the boundary of a region centered at the probe tip is quite

small, the finite element model of liver over the region separately may yield different liver tissue deformation than finite element analysis over the whole liver domain. As the region of interest approaches the whole liver domain, the maximum liver displacement from the finite element analysis over the region of interest approaches to the global maximum liver displacement from the finite element analysis over the whole liver domain.

CHAPTER X
CONCLUSIONS AND FUTURE WORKS

This dissertation presents the comprehensive study of tissue deformation under small force loads using high resolution Micro-CT and CBCT imaging technologies. It was first proposed to use these high resolution imaging technologies to study surface and volume changes of the soft tissues.

In Chapter III, high resolution imaging technologies Micro-CT and CBCT were introduced to study soft tissue deformation in stead of using traditional low resolution CT images.

In Chapter IV, the principle of finite element method, and the linear elastic model, and the neo-Hooke's model were described as the basic mechanical models and tool for the modeling of liver tissue responses under the small force loads.

In Chapter V, the procedure for preprocessing of the object was introduced in steps: image acquisition, image segmentation, mesh generation and material parameter measurements for finite element modeling. The process was proposed to acquire the images to study the soft tissue deformation. One automatic variable segmentation method was developed for liver tissue segmentation.

In Chapter VI, the linear elastic model and the neo-Hooke's hyperelastic model were applied to describe the mechanical responses of the liver tissue under small force loads. A validation system was proposed to verify different finite element models for soft tissue deformations. The FE method was used to analyze the lamb liver deformations under certain force loads using the linear elastic model and the neo-Hooke's hyperelastic model. The deformations were measured from the models and compared each other and to the real deformations measured by experiments. It was found that the linear elastic model is more applicable to lamb liver than the neo-Hooke's hyperelastic model for small force loads

($< 40g$) and that the neo-Hooke's model is closer to reality when the force load is larger than $40g$. It was verified that the high resolution imaging technologies can be used to study the surface and volume changes of soft tissues. The comparability of the results presented herein to the *in vivo* tissue, which is valuable for future surgery simulation design, is beyond the scope of this work and will be investigated in future studies.

In Chapter VII, the stereolithograhphical volume file and volume mesh generation are introduced in details for the preprocessing step. The contact of the indentor with the volume mesh surface is explained.

In Chapter VIII, the high resolution Micro-CT and CBCT images were employed to show the liver tissue deformations for different material parameters using the linear elastic model. The optimal material parameters were determined by minimizing the absolute differences between the displacements from real experiment and the displacements from simulation. For the force load of 20 grams, the determined Young's modulus and Poisson's ratio were quite consistent to those in literature and the measurements using the DMA. It was found that for small force loads of 5 and 10 grams, the determined material parameters were not matched well with those from literature and the ones measured using the DMA. For the larger force load of 40 grams, the material parameters determined from simulation deviated from the ones measured using the DMA.

In Chapter IX, it was proposed to investigate region of interest finite element modelling of liver tissue. The results show that such modelling may generate different deformations from those using the finite element analysis over the whole liver domain. The maximum liver displacement on the boundary of a region centered at the probe tip is quite small, the finite element model of liver over the region separately may yield slightly different liver tissue deformation than finite element analysis over the whole liver domain. As the region of interest approaches the whole liver domain, the maximum liver displacement from the finite element analysis over the region of interest approaches to the global maximum liver displacement from the finite element analysis over the whole liver domain. In the process of studying the maximum displacements, one specified region of interest may be found over which finite element analysis can be performed. The results will be slightly

different from the finite analysis over the entire region but such difference may be ignored or allowed in practice. Such a study might provide potential validation of the usage of surgeries using endoscopic instruments.

In future work, it is planned to investigate more complicated biomechanical models using Micro-CT and CBCT, investigate the influence of the region-of-interest based finite element analysis of other tissue deformations compared to the modeling of the entire tissue on soft tissue deformations. Also, it is planned to propose a more complicated finite element model of the deformation of brain tissue which is inhomogeneous with white matter, grey matter, and Cerebral spinal fluid nested together.

REFERENCES

[1] H. Shi, A. Farag, Intensity and region-of-interest-based finite-element modeling of brain deformation, Proceedings of CARS 2004, 373-377, 2004.

[2] M. Beer-Gabel, S. Delmotte, and L. Muntlak, Computer assisted training in endoscopy from a simulator to a learning station, *Endocopy* 24:534-538, 1992.

[3] P. Dubois, P. Mesure, F. Peugnet etc., Training simulator for retinal laser photocoagulation: A new approach for surgeon's apprenticeships, *Proceedings of SPIE Conference on Surgical-Assist Systems*, 54-62.

[4] R. Johnston, S. Bhoyul, L. Way etc., Accessing a virtual reality surgical skills simulator, P*roceedings of Medicine Meets Virtual Reality* 4:608-617, 1996.

[5] G. Higgins, G. Merril, I. Hettinger etc., New simulation technologies for surgical training and certification: Current status and future projections, *Presence* 6 (2):160-172, 1997.

[6] F. Tendick, M. Downes, T. Goktekin etc., A virtual environment testbed for training laparoscopic surgical skills, *Presence* 9(3):236-255, 2001.

[7] N. Ayache and H. Delingette, editors, *International Symposium on Surgery Simulation and Soft Tissue Modeling*, LNCS 2673, Juan-Les-Pins, France, 2003.

[8] S. Cotin and D. Metaxas, editors, International Symposium on Medical Simulation, LNCS 3078, Cambridge, USA, 2004.

[9] J. Morin, G. Dionne, M. Dumont et al., MR guided percutaneous cryosurgery of breast carcinoma: technique and early clinical results, *Proc. Int. Mag. Res. in Med.* 71, 2000.

[10] F.J. Carter, T.G. Frank, P.J. Davies, D. McLean, A. Cuschieri, 2001, Measurements and modeling of the compliance of human and porcine organs, Medical Image Analysis, Vol. 5, 231-236, 2001.

[11] T. Hu, J. Desai, A Biomechanical Model of the Liver for Reality-Based Haptic Feedback, Proc. Medical Image Computing and Computer Assisted Intervention (MICCAI), Montreal, Canada, 75-82, 2003.

[12] Y.C. Fung, Biomechanics: Mechanical Properties of Living Tissues, Springer-Verlag, New York, 1981.

[13] W. Larrabee, A finite element model of skin deformation: Biomechanics of skin and tissue: a review, Laryngoscope, 96:399-405, 1986.

[14] I. Brouwer, J. Ustin, L. Bentley, A. Sherman, N. Dhruv, F. Tendick, Measuring In Vivo Animal Soft Tissue Properties for Haptic Modeling in Surgical Simulation, Proc. Medicine Meets Virtual Reality, 69-74, 2001.

[15] M.P. Ottensmeyer, A.E. Kerdok, R.D. Howe, S.L. Dawson, The Effects of Testing Environment on the Viscoelastic Properties of Soft Tissues, International Symposium on Medical Simulation, 9-18, 2004.

[16] Z. Liu and L. Bilston, On the viscoelastic character of liver tissue: experiments and modeling of the linear behavior, Biorheology, Vol. 37, 191-201, 2000.

[17] K. Miller, and K. Chinzei, Constitutive modeling of brain tissue: experiment and theory, Journal of Biomechanics, Vol. 30, Nos. 11/12, 1115-1121, 1997.

[18] C.C. Ward, Finite element models of the head and their use in brain injury research, Proceedings of the 26th Car Crash Conference, 71-85, 1982.

[19] R. Satava, Medicine 2001 the king is dead - en Interactive Technology and the new paradigm for healthcare. Morgan and Satava (eds). IOS Press, Washington, 334-339, 1995.

[20] P.J. Edwards, D.L.G. Hill, J.A. Little, and D.J. Hawkes, A three component deformation model for image-guided surgery, Medical Image Analysis, 2(4): 355-367, 1998.

[21] N. Hata, A. Nabavi, W.M. Wells III, S.K. Warfield, R. Kikinis, P.M. Black, and F.A. Jolesz, Three-dimensional optical flow method for measurement of volumetric brain deformation from intraoperative MR images, Journal of Computer Assisted Tomography, 24:521-538, 2000.

[22] D.L.G. Hill, C.R. Maurer, R. Maciunas, A.J. Martin, S. Sabanathan, W.A. Hall, D.J. Hawkes, D. Ruckert, C.L. Truwit, Assesment of Intraoperative brain deformation using interventional MR imaging, In Taylor, C. and Colchester, A., editors, MICCAI'99: 910-919, 1999.

[23] R. Bajcsy, and S. Kovacic, Multi-resolution elastic matching, Computer Vision, Graphics, and Image Processing, 46:1-21, 1989.

[24] C. Davatzikos, Spatial transformation and registration of brain images using elastically deformable models, Comp. Vision Image Understanding, 66(2):207-222, 1997.

[25] J. Gee, M. Reivich, R. Bajcsy, Elastically deforming 3D atlas to match anatomical brain images, Journal of Computer Assisted Tomography, 17(2):225-236, 1993.

[26] P. Thompson, and A.W. Toga, A surface-based technique for warping three-dimensional images of the brain, IEEE Trans. Med. Imag., 15(4):402-417, 1996.

[27] P. Shi, G. Robinson, R. Constable, A. Sinusas, J. Duncan, A model-based integrated approach to track myocardial deformation using displacement and velocity constraints, Proceedings of the Fifth International Conference on Computer Vision 1995, 687-692, 1995.

[28] M. Bro-Nielsen, Finite element modeling in surgery simulation, Proceedings of the IEEE, Vol. 86, No. 3, 490-503, 1997.

[29] S. Cotin, H. Delingette, and N. Ayache, Real-time elastic deformations of soft tissues for surgery simulation, IEEE Transaction on Visualization and Computer Graphics, Vol. 5, No. 1, 62-79, 1999.

[30] O. Škrinjar, D. Spencer, J. Duncan, Brian shift modeling for use in neurosurgery, Proceedings of MICCA'98, 641-649, 1998.

[31] O. Škrinjar, C. Studholme, A. Nabavi, J. Duncan, et al., Steps toward a stereo-camera-guided biomechanical model for brain shift compensation, Proceedings of IPMI'2001, 183-189, 2001.

[32] S.K. Warfield, F. Talos, A. Tei, A. Bharatha, A. Nabavi, M. Ferrant, P.M. Black, F.A. Jolesz, R. Kikinis, Real-time registration of volumetric brain MRI by biomechanical simulation of deformation during image guided neurosurgery, Computing and Visual Science, Vol. 5, 3-11, 2002.

[33] M. Miga, K. Paulsen, F. Kennedy et al., Initial in vivo analysis of 3D heterogeneous brain computations for model-updated image guided neurosurgery, Proceedings of MICCA'98, 743-752, 1998.

[34] K. Miller, K. Chinzei, G. Orssengo, P. Bednarz, Mechanical properties of brain tissue invivo: experiment and computer simulation. J. Biomechanics, Vol. 33, 1369-1376, 2000.

[35] I.M. Miga, K.D. Paulsen, P.J. Hoopes, F.E. Kennedy, A. Hartov, and W.R. Roberts, In vivo quantification of a homogeneous brain deformation model for updating preoperative images during surgery, IEEE Transactions on Biomedical Engineering, Vol. 47, No. 2, 266-273, 2000.

[36] T. Hartkens, D.L.G. Hill, A.D. Castellano-Smith, D.J. Hawkes, C.R. Maurer, Jr.A.J. Martin, W.A. Hall, H. Liu, and C.L. Truwit, Measurement and analysis of brain deformation during neurosurgery, IEEE Transactions on Medical Imaging, Vol. 22, No. 1, 82-92, 2003.

[37] H. Delingette, and N. Ayache, Soft tissue modeling for surgery simulation. In N. Ayache, editor, Computational Models for the Human Body, Handbook of Numerical Analysis (Ed: Ph. Ciarlet). Elsevier, 2004.

[38] P.J. Edwards, D.L.G. Hill, J.A. Little, D.J. Hawkes, Deformation for image guided interventions using a three component tissue model, Proceedings of the 15th International Conference, IPMI'97, 218-231, 1997.

[39] M. Ferrant, A. Nabavi, B. Macq, P.M. Black, F.A. Jolesz, R. Kikinis, and S.K. Warfield, Registration of 3D intraoperative MR images of the brain using a finite element biomechanical model, IEEE Transactions on Medical Imaging, Vol. 20, 1384-1397, 2001.

[40] M. Ferrant, A. Nabavi, B. Macq, P.M. Black, F.A. Jolesz, R. Kikinis, and S.K. Warfield, Serial registration of intraoperative MR images of the brain, Medical Image Analysis, Vol. 6, No., 4, 337-359, 2002.

[41] S.K. Warfield, F. Talos, C. Kemper, L. O'Donnell, C.F. Westin, W.M. Wells, P.M. Black, F.A. Jolesz, and R. Kikinis, Capturing brain deformation, Surgery Simulation and Soft Tissue Modeling (Eds: Ayache, N. and Delingette, H.), Lecture Notes in Computer Science 2673, 203-217, 2003.

[42] O. Škrinjar, A. Nabavi, J. Duncan, Model-driven brain shift compensation, Medical Image Analysis, 6(4), 361-373, 2002.

[43] O. Clatz, H. Delingette, E. Bardinet, D. Dormont, and N. Ayache, Patient-specific biomechanical model of the brain: application to Parkinson's disease procedure, Lecture Notes in Computer Science 2673, 321-331, 2003.

[44] K. Miller, Constitutive model of brain tissue suitable for finite element analysis of surgical procedures, Journal of Biomechanics, Vol. 32, 531-537, 1999.

[45] Z. Taylor, K. Miller, Reassessment of brain elasticity for analysis of biomechanisms of hydrocephalus, Journal of Biomechanics, Vol. 37, 1263-1269, 2004.

[46] G. Soza, R. Grosso, C. Nimsky, G. Greiner, P. Hastreiter, Estimating mechanical brain tissue properties with simulation and registration, MICCAI 2004, LNCS 3217, 276-283, 2004.

[47] C.A. Kemper, I.-F. Talos, A. Golby, P.M. Black, R. Kikinis, W.E.L. Grimson, and S.K. Warfield, An anisotropic material model for image guided neurosurgery, MICCAI 2004, LNCS 3217, 267-275, 2004.

[48] A. Hagemann, K. Rohr, H.S. Stiehl, U. Spetzger, and J.M. Gilsbach, Biomechanical modeling of the human head for physically based, nonrigid image registration, IEEE Transactions on Medical Imaging, Vol. 18, No. 10, 875-884, 1999.

[49] A. Hagemann, K. Rohr, H.S. Stiehl, Coupling of fluid and elastic models for biomechanical simulation of brain deformations using FEM, Medical Imaging Analysis, 6, 375-388, 2002.

[50] A.D. Castellano-Smith, T. Hartkens, J. Schnabel, D.R. Hose, H. Liu, W.A. Hall, C.L. Truwit, D.J. Hawkes, and D.L.G. Hawkes, Constructing patient specific models for correcting intraoperative brain deformation, Proceedings of MICCA'2001, 1091-1098, 2001.

[51] K.V. Hansen, M.S. Eskildsen, O.V. Larsen, Region-of-interest based finite element modeling of the brain-an approach to brain surgery simulation, Proceedings of the 14th International Conference on Pattern Recognition, Vol. 1, 292-296, 1998.

[52] Immersion Incorporation website www.immersion.com.

[53] M. Sabry Hassouna and A.A. Farag, 3D Path Planning for Virtual Endoscopy, Proc. of Computer Assisted Radiology and Surgery (CARS), 115-120, 2005.

[54] A.A. Farag, A. El-Baz and G. Gimel'farb, Detection and recognition of lung abnormalities using deformable templates," Proc. of ICPR International Conference on Pattern Recognition, ICPR-2004, 738-741, 2004.

[55] H. Hassan, A. El-Baz, A. G. Farman, and M. Miller, A complete 3D Model of The Human Jaw, Proc. of Computer Assisted Radiology and Surgery (CARS), 1244-1249, 2005.

[56] A.A. Farag, H. Hassan, R. Falk, and S.G. Hushek, 3D Volume Segmentation of MRA Data Sets Using Level Sets, Academic Journal of Radiology, 419-435, 2004.

[57] A.A. Farag, A. El-Baz, G.L. Gimel'farb, Precise segmentation of multimodal images, IEEE Transactions on Image Processing, Vol. 15, no. 4, 952-968, 2006.

[58] A. El-Baz, S.E. Yuksel, H. Shi, A. A. Farag, M.A. El-Ghar, T. Eldiasty, and M. A. Ghoneim, 2D and 3D Shape Based Segmentation Using Deformable Models, Proc. of International Conference on Medical Image Computing and Computer-Assisted Intervention (MICCAI), 821-829, 2005.

[59] S. Osher and J. Sethian, Fronts Propagating with Curvature-Dependent Speed: Algorithms Based on the Hamilton-Jacobi Formulation, Journal of Computational Physics, Vol. 79, 1249, 1988.

[60] M. Kass, A.Witkin, and D. Terzopoulos, Snakes: active contour models, Intl. J. Comp. Vis., Vol. 1, 321331, 1987.

[61] T. McInerney and D. Terzopoulos, Deformable Models in Medical Image Analysis: A Survey, Medical Image Analysis, Vol. 1, No. 2, 91-108, 1996.

[62] L. Evans, Partial Differential Equations, Providence: American Mathematical Society, 1998.

[63] N. Paragios, M. Rousson, and V. Ramesh, Matching Distance Functions: A Shape-to-Area Variational Approach for Global-to-Local Registration, European Conference in Computer Vision, Copenhagen, Denmark, June 2002.

[64] A. Eid and A.A. Farag, A Silhouette-Contour Based 3-D Registration Methodology As a Pre-Evaluation Step Of 3-D Reconstruction Techniques, Proc. of IEEE International Conference on Image Processing (ICIP), 505-508, 2005.

[65] P. Besl and N. Mckay, A Method for Registration of 3-D Shapes, IEEE Tr. on PAMI, Vol. 14, No. 2, 239256, 1992.

[66] A.A. Farag, M.S. Hassouna and A. El-Baz, Real Time Vision-Based Image Guided Neurosurgery, Proc. of Computer Assisted Radiology and Surgery, 467-472.

[67] ABAQUS User's Manuals, ABAQUS Version 6.4, HKS Inc, US, 2003.

[68] D.L. Batiste, A. Kirkley, S. Laverty, L.M. Thain, A.R. Spouge, J.S. Gati, P.J. Foster, D.W. Holdsworth, High-resolution MRI and micro-CT in an ex vivo rabbit anterior cruciate ligament transection model of osteoarthritis, Osteoarthritis Cartilage, Vol. 12, No. 8, 614-626, 2004.

[69] C. Arnheiter, W.C. Scarfe and A.G. Farman, Trends in maxillofacial cone-beam computed tomography usage, Vol. 22, No. 2, 80-85, 2006.

[70] C.H. Kau and S. Richmond, Current Products and Practice: Three-dimensional cone beam computerized tomography in orthodontics, Journal of Orthodontics, Vol. 32, No. 4, 282-293, 2005.

[71] H.S. Tuana and D.W. Hutmacher, Application of micro CT and computation modeling in bone tissue engineering, Computer-Aided Design, Vol. 37, No. 11, 1151-1161, 2005.

[72] R. Baba, K. Ueda and M. Okabe, Using a flat-panel detector in high resolution cone beam CT for dental imaging, Dentomaxillofacial Radiology33, 285-290, 2004.

[73] J.B. Ludlow, L.E. Davies-Ludlow, S.L. Brooks and W.B. Howerton, Dosimetry of 3 CBCT devices for oral and maxillofacial radiology: CB Mercuray, NewTom 3G and i-CAT, Dentomaxillofacial Radiology, 35, 219-226, 2006.

[74] D. Saint-Felix, Y. Trousset, C. Picard, C. Ponchut, R. Romeas and A. Rougee, In vivo evaluation of a new system for 3D computerized angiography, Phys. Med. Biol. 39, 583-595, 1994.

[75] R. Fahrig, A.J. Fox, S. Lownie and D.W. Holdsworth, Use of a C-arm system to generate true three-dimensional computed rotational angiograms: preliminary in vitro and in vivo results, American Journal of Neuroradiology, Vol 18, Issue 8, 1507-1514, 1997.

[76] S. Hirota, N. Nakao, S. Yamamoto, K. Kobayashi, H. Maeda, R. Ishikura, K. Miura, K. Sakamoto, K. Ueda and R. Baba, Cone-Beam CT with Flat-Panel-Detector Digital Angiography System: Early Experience in Abdominal Interventional Procedures, CardioVascular and Interventional Radiology, Vol. 29, No. 6, 1034-1038, 2006.

[77] U. Ken, B. Rika, O. Masakazu, K. Takayuki, N. Norio, H. Shozo, I. Reiichi, Development and Application of Cone Beam CT Technology for Innovation of Diagnostic and Interventional Radiology with 3D Imaging Function, Hitachi Hyoron, Vol. 88, No. 9, 694-697, 2006.

[78] R. Ning, and B. Chen, Cone beam volume CT mammographic imaging: feasibility study, Presented at Proceedings of SPIE - The International Society for Optical Engineering, Vol. 4320, 655-664, 2001.

[79] S. Rudin, A.T. Kuhls, G.K. Yadava, G.C. Josan, Y. Wu, R.N. Chityala, H.S. Rangwala, N.C. Ionita, K.R. Hoffmann, and D.R. Bednarek, New light-amplifier-based detector designs for high spatial resolution and high sensitivity CBCT mammography and fluoroscopy, Proc. SPIE, Vol. 6142, 61421R, 2006.

[80] J.N. Reddy, Energy and Variational Methods in Applied Mechanics, John Willey & Sons, Inc., 1984.

[81] O.C. Zienkiewicz & R.L. Taylor, The Finite Element Method, Vol. 2, Butterworth-Heinemann, 2000.

[82] Y.W. Kwon, H. Bang, The Finite Element Method, CRC Press, Inc., 1996.

[83] S. Owen, A survey of unstructured mesh generation, Technical report, ANSYS Inc., 2000.

[84] M.S. Shephard and M.K. Georges, Three-Dimensional Mesh Generation by Finite Octree Technique, International Journal for Numerical Methods in Engineering, Vol. 32, 709-749, 1991.

[85] R. Lohner, Progress in Grid Generation via the Advancing Front Technique, Engineering with Computers, Vol. 12, 186-210, 1996.

[86] J.M. Sullivan Jr, G. Charron and K.D. Paulsen, A three-dimensional mesh generator for arbitrary multiple material domains, Finite Elements in Analysis and Design, Vol. 25, 219-241, 1997.

[87] H. Hartmann and F. Kruggel, A fast algorithm for generating 3D finite element meshes from magnetic resonance tomograms, Proceedings of IEEE Workshop on Biomedical Image Analysis, 184-192, 1998.

[88] J. Schöberl, NETGEN - An advancing front 2D/3D-mesh generator based on abstract rules, Comput. Visual. Sci, Vol. 1, 41-52, 1997.

[89] H. Shi, R. Fahmi, and A. Farag, Validation Framework of the F.E. Modeling of Liver Tissue, Lecture Notes in Computer Science: Medical Image Computing and Computer-Assisted Intervention - MICCAI 2005, Springer Verlag, New York, Volume 3749, 531-538, 2005.

[90] S.H. Lee, H.C. Kimb, S.M. Hurb and D.Y. Yang, STL file generation from measured point data by segmentation and Delaunay triangulation, Computer-Aided Design, Vol. 34, No. 10, 691-704, 2002.

[91] Y. Ito Y, K. Nakahashi, Surface triangulation for polygonal models based on CAD data, International Journal for Numerical Methods in Fluids Vol. 39, 75-96, 2002.

[92] Stereolithography Interface Specification, 3D Systems, Inc., CA, 1989.

[93] K. Nakahashi, D. Sharov, Direct surface triangulation using the advancing front method, AIAA Paper, 95-1686-CP, 1995.

[94] W. Schroeder, K. Martin, B. Lorensen, The Visualization Toolkit An Object-Oriented Approach To 3D Graphics, Kitware, Inc., 2002.

[95] F. Schubert, Numerical time-domain modeling of linear and nonlinear ultrasonic wave propagation using finite integration techniques theory and applications, Ultrasonics 42, 221-229, 2004.

[96] K. Miller and K. Chinzei, Simple validation of biomechanical models of brain tissue, Journal of Biomechanics 31, 104, 1998.

[97] I. Sakuma, Y. Nishimura, C.K. Chui, E. Kobayashi, H. Inada, X. Chen and T. Hisada, In vitro Measurement of Mechanical Properties of Liver Tissue under Compression and Elongation Using a New Test Piece Holding Method with Surgical Glue, IS4TH, 284-292, 2003.

[98] K. Miller, Method of testing very soft biological tissues in compression, Journal of Biomechanics. 38, 153-158, 2005.

[99] M. Kauer, V. Vuskovic, J. Dual, G. Szekely and M. Bajka, Inverse finite element characterization of soft tissues, Medical Image Analysis 6, 275-287, 2002.

[100] C. Studholme, D.L.G. Hill and D.J. Hawkes, An overlap invariant entropy measure of 3D medical image allignment, Pattern Recognition 32, 71-86, 1999.

[101] C.A. Rawlings, S.V. Lue, C. King, L. Freeman, C. Greenacre, A. Chernosky, F. Mohamed, R. Damion, Serial laparscopic biopsies of liver and spleen in schistosoma-infected baboons, Comparative Medicine, 50, 551–555, 2000

[102] G. Székely, C. Brechbühler, J. Dual, R. Enzler, J. Hug, R. Hutter, N. Ironmonger, M. Kauer, V. Meier, P. Niederer, A. Rhomberg, P. Schmid, G. Schweitzer, M. Thaler, V. Vuskovic, G. Tröster, Virtual reality-based simulation of endoscopic surgery, PRESCIENCE, 9, 310–333, 2000.

[103] M. Bro-Nielsen, S. Cotin, Real-time volumetric deformable models for surgery simulation using finite elements and condensation, Computer Graphics Forum, 15, 57–66, 1996.

[104] S. Cotin, H. Delingette, J.M. Clement, V. Tassetti, J. Marescaux, N. Ayache, Volumetric deformable models for simulation of laparoscopic surgery, Volume 1124, 1996.

[105] C. Forest, H. Delingette, N. Ayache, Removing tetrahedra from manifold tetrahedralisation : application to real-time surgical simulation, Medical Image Analysis, 9, 113–122, 2005.

NOMENCLATURE

The following convention is used throughout the dissertation.

Φ level set function

∂ partial differential

$\| \cdot \|$ Euclidean norm of a vector

δ Delta Dirac function

κ mean curvature

L length

A area

H Haviside function

$2D$ two-dimensional space

$3D$ three-dimensional space

σ stress (the force per unit area)

ϵ strain

E Young's modulus

ν Poisson's ratio

λ Lam material constant

μ shear modulus

μ_0 initial shear modulus

K_0 initial bulk modulus

$\mathbf{f}$ external force

$\mathbf{F}$ the term induced by the external force in equilibrium equation

A_o cross sectional area

Ω a connected open region

$\partial\Omega$	the boundary of a connected open region
$\mathbf{u}$	displacement vector
$\mathbf{U}$	assembled global displacement vector
$\mathbf{p}$	a point in three-dimensional space
Δ	gradient operator
$H_0^1(\Omega)$	Soblev function space
$\int$	integral symbol
$E(u)$	total potential energy
$\mathbf{M}$	material matrix
$\mathbf{B}$	relation operator of strain to displacement
$\mathbf{K}$	global system stiffness matrix
N_i^e	shape function of tetrahedrons
V	volume domain of an object
V^e	volume domain of an element
$\delta E^e(u^e)$	variation of total potential energy of one element
W	energy potential function
C_{10}	one of material parameters in the neo-Hooke's model
D_1	one of material parameters in the neo-Hooke's model
$\bar{I}_1$	first deviatoric strain invariant
$\bar{\lambda}_i$	deviatoric stretch
J^{el}	elastic volume ratio
in	length unit inch
Pa	unit of Young's modulus Pascal

CURRICULUM VITAE

NAME: Hongjian Shi

ADDRESS:

Computer Vision and Imaging Processing
Department of Electrical and Computer Engineering
University of Louisville
Louisville, KY 40292

EDUCATION:
- B.Sc., in Math Education, Henan Normal University, China 1984
- M.Sc., in Mathematics, Peking University, China 1987
- Ph.D. in Mathematics, Simon Fraser University, Canada 1997
- M.Sc. in Electrical and Computer Engineering, The University of British Columbia, Canada

RESEARCH:
- Applied mathematics
- Edge detection and image sampling in image processing
- Video compression and noise reduction
- Finite element analysis
- Medical Imaging
- Medical image processing and segmentation

PUBLICATIONS:

- H. Shi, A. Farag, R. Fahmi, D. Chen, Validation of Finite Element Models of Liver Tissue using Micro-CT, accepted and to appeare in IEEE Transactions on Biomedical Engineering, May 2007.

- A. Farag, H. Shi, R. Fahmi, and M. J. Voor, Basic Experiments on Finite Element Analysis of Soft Tissues, Chapter 12, Biomechanics Applied to Computer Assisted Surgery, by editor: Yohan Payan, Research Signpost Publications, 193-208, 2005.

- H. Shi, R. Fahmi, and A. Farag, Validation Framework of the F.E. Modeling of Liver Tissue, Lecture Notes in Computer Science: Medical Image Computing and Computer-Assisted Intervention - MICCAI 2005, Springer Verlag, New York, Volume 3749, 531-538, 2005.

- A. El-Baz, S.E. Yuksel, H. Shi, A. Farag, M.A. El-Ghar, T. Eldiasty, and M. A. Ghoneim, 2D and 3D Shape Based Segmentation Using Deformable Models, Lecture Notes in Computer Science: Medical Image Computing and Computer-Assisted

Intervention - MICCAI 2005, Springer Verlag, New York, Volume 3750, 821-829, 2005.

- H. Shi and A. Farag, Validating linear elastic and linear viscoelastic models of lamb liver tissue using cone-beam CT, International Congress Series: Proceedings of Computer Assisted Radiology and Surgery (CARS), Volume 1281, 473-478, 2005.

- H. Shi and R. Fahmi, Energy Minimization within the F.E. Framework to Predict Liver Tissue Deformation, GVIP 05 Conference, 19-21 December 2005, CICC, Cairo, Egypt.

- H. Shi and A. Farag, Intensity and Region-of-Interest Based Finite Element Modeling of Brain Deformation, International Congress Series: Proceedings of Computer Assisted Radiology and Surgery (CARS), Volume 1268, 373-377, 2004.